Nanostructured Photocatalytic Systems to Enable Portable Kidney Dialysis and Precision Synthesis

Hao Tang

A dissertation

submitted in partial fulfillment of the

requirements for the degree of

Doctor of Philosophy

University of Washington

2023

Reading Committee:

Bruce J. Hinds, Chair

Guozhong Cao

Vincent C. Holmberg

Program Authorized to Offer Degree:

Molecular Engineering & Sciences

University of Washington

Abstract

Nanostructured Photocatalytic Systems to Enable Portable Kidney Dialysis and Precision Synthesis

Hao Tang

Chair of the Supervisory Committee:
Bruce J. Hinds
Department of Materials Science & Engineering

Two distinct types of photocatalytic material systems have been studied for wearable dialysis devices and precise pharmaceutical synthesis: TiO_2 nanowire anodes and gold nanoporous membranes. The study on TiO_2 involves the development of a novel urea photodecomposition system (POUR) that efficiently and selectively converts urea into N_2 and CO_2, enabling spent dialysate regeneration for portable kidney dialysis. The long-term stability and regeneration treatments of TiO_2 photocatalyst has been investigated. The oxidative environment generated localized around the TiO_2 surface is considered as an efficient way to remove the Ti-C and maintain the photocatalytic performance of TiO_2. External voltage applied to the TiO_2 single crystal nanowires dramatically enhances the collection of photogenerated electrons to the cathode and pushing holes to reaction surface thereby minimizing the recombination process and

significantly increasing the photocurrent (~14x) and the urea photodecomposition rate. Further mechanistic investigations revealed the requirement of chloride (Cl^-) for the complete oxidation of urea to physiologically safe N_2 and CO_2. Quenching studies proved a mechanism based on TiO_2 surface bound radical intermediates (Ti-Cl·). High photocurrent to reaction efficiency for this 6 e^-/h^+ process and selectivity of urea suggests urea nitrogens are bound to TiO_2 surface (Ti-N bonds) during the complete oxidation process. On the other hand, gold nanoparticles in a plasmonic flow reactor demonstrated an over 200% quantum efficiency for peroxide activation, offering controlled single oxidation reactions for pharmaceutical synthesis. The reactor design, optimized pore diameter, and LED illumination wavelength were crucial factors influencing peroxide activation efficiency. Overall, these findings shed light on the potential applications of TiO_2 and gold nanoparticles in advanced photocatalytic systems for the wearable dialysis device and precise pharmaceutical synthesis.

TABLE OF CONTENTS

LIST OF FIGURES

LIST OF TABLES

ACKNOWLEDGEMENTS

As I am completing this remarkable journey in my life, I would love to first thank my principal investigator, Prof. Bruce Hinds, for his support and mentorship these years. His commitment to my academic growth has been nothing short of inspiring, and I have learned a lot about how to be a good and successful scientist from him. I am also honored to have Buddy Ratner, Guozhong Cao and Vincent Holmberg to be as my committee, with their continuous help, kindly support and visionary insights on my academic study during the PhD journey.

Meanwhile, I want to thank all my colleagues at Hinds' lab for help discussions and collaborations. I do have a great time work with all you guys.

I want to give a special thanks to my undergraduate advisor, Dr. Qin. Without her support and encouragement, I would not have continued to pursuit for a PhD degree at UW.

At last, I would love to thank all my family and friends for their kindly support, boundless patience, and unflagging encouragement; also MoMo, my little cat, for his lovely companionship in my last two PhD years.

Chapter 1. INTRODUCTION

1.1 KIDNEY DIALYSIS AND PORTABLE DIALYSIS DEVICE

Chronic kidney disease (CKD) affects millions of people worldwide, necessitating effective treatment options to manage its debilitating effects. Among the treatment modalities, kidney dialysis plays a critical role in removing waste products and excess fluids from the bloodstream for patients with end-stage renal disease (ESRD). Traditional hemodialysis imposes substantial burdens on patients in terms of time commitment and lifestyle limitations. The requirement for multiple visits to a dialysis center each week, coupled with lengthy treatment sessions, significantly impedes patients' ability to engage in regular activities, work, and travel. Furthermore, this conventional hemodialysis approach entails the rapid removal of waste products, excess fluids, and electrolytes from the bloodstream within a relatively short duration during the treatment session, leading to considerable metabolite fluctuations. The strict adherence to fluid intake restrictions and dietary constraints, particularly regarding potassium, phosphorus, and sodium intake, further exacerbates the challenges faced by patients, impacting their dietary satisfaction and meal enjoyment. In response to these limitations, the pursuit of portable dialysis devices has garnered substantial attention, striving to enable continuous and improved dialysis therapy that can be administered conveniently in the home or on the go.

Portable dialysis devices offer numerous advantages, allowing patients to live a more flexible and convenient life. However, one of the challenges in designing such devices lies in the regeneration of dialysate within the device itself. Traditional dialysis methods rely on large volumes of high-quality dialysate (~120L per session), a specialized solution used to facilitate the exchange of waste products and excess fluids across the hemolysis membrane. This reliance on external dialysate supply hinders the portability and practicality of traditional dialysis treatments. To overcome these challenges, researchers have explored alternative approaches for dialysate regeneration within portable dialysis devices. Among these approaches are the use of absorbents and enzymes to remove urea and other non-uremic toxins from the spent dialysate. Absorbents, such as activated carbon or ion-exchange resins, can bind most uremic toxins, however, have very low (~mg/g) binding capacity for urea. Similarly, enzymes, such as urease, can be employed to accelerate the hydrolysis of urea into ammonia and carbon dioxide, facilitating its removal. Notable here is that ammonia from the decomposition of urea via enzymes is to the patients at ~100μM concentration levels. Thus, the systems require successive ion exchange steps to remove ammonium (Fig 1.1a) adding significant cost and hazards associated with cracks in adsorbent beds.

While absorbents and enzymes have shown some promises for using in portable dialysis devices to regenerate the spent dialysate, the integration of novel nanotechnologies like TiO_2 photocatalysis to decompose urea and non-uremic toxins holds a greater potential. TiO_2, a widely studied and cost-effective photocatalyst, exhibits remarkable photocatalytic activity and selectivity, making it an attractive option for various applications, including degradation of organic pollutants, energy conversion/storage, and here for spent dialysate regeneration. By leveraging TiO_2 photocatalysis, it becomes possible to decompose urea in the spent dialysate efficiently and selectively, enabling the possibility for a portable kidney dialysis device. Figure 1.1 below illustrates the structure of portable dialysis cartridges via three different methods for urea removal/degradation; Figure 1.2 shows the two-stage dialyzer for efficient removal of water and urea with the designed TiO_2 photocatalysis oxidation system.

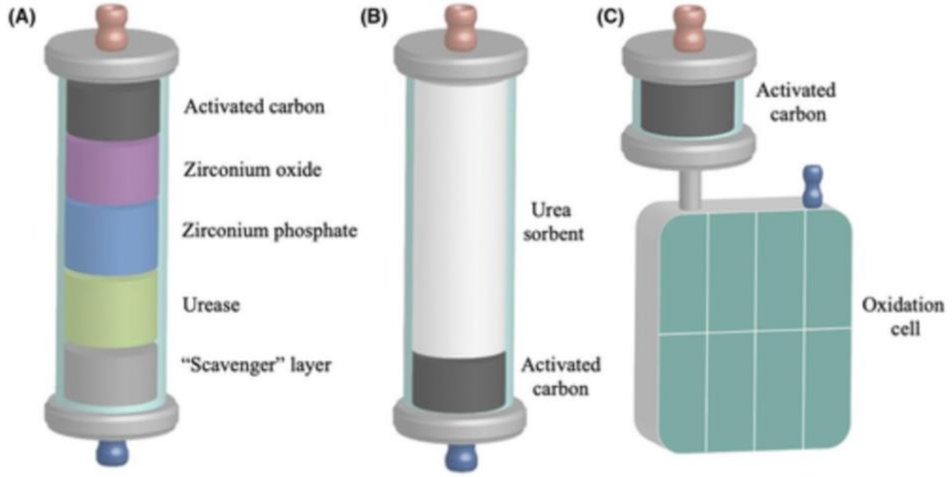

Figure 1.1. Structure of urea removal/degradation cartridge based on (A) urease cartridge; (B) sorbent and (C) photo-oxidation; reproduced with permission from ref [1]. Copyright 2022, Wiley.

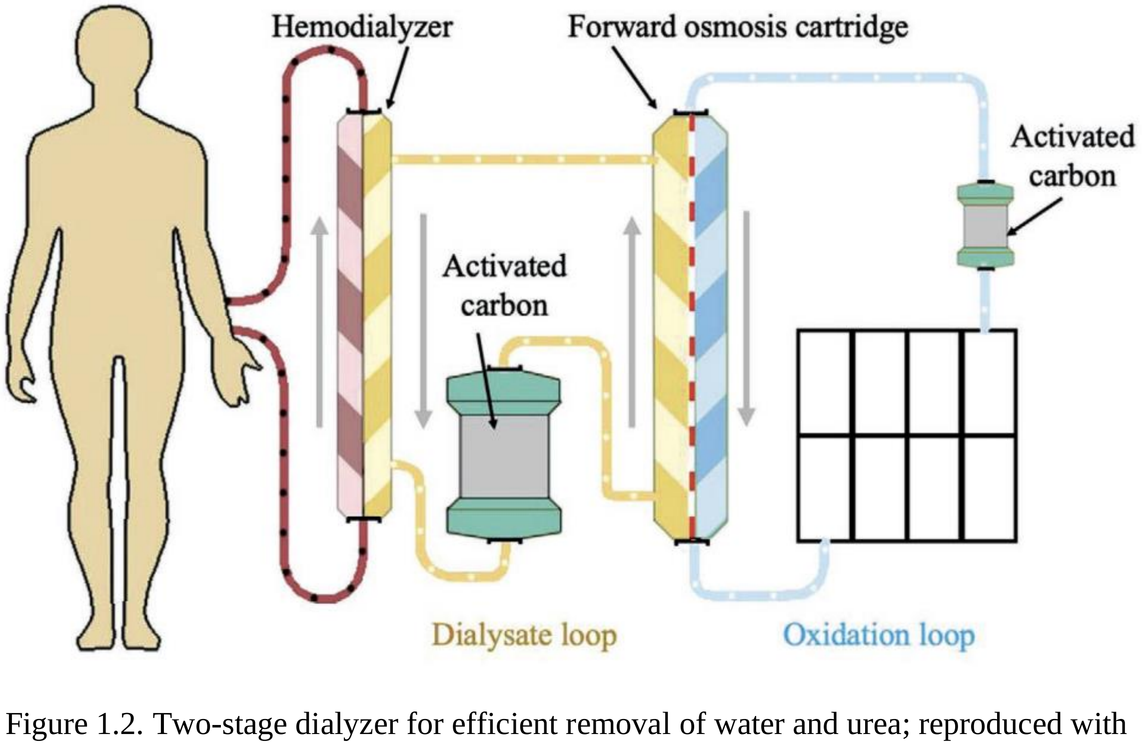

Figure 1.2. Two-stage dialyzer for efficient removal of water and urea; reproduced with permission from ref [1]. Copyright 2022, Wiley.

The utilization of TiO_2 photocatalysis in portable kidney dialysis devices offers several advantages. First, it eliminates the need for external dialysate supply, making the device more self-contained and compact. This portability enhances patients' mobility and allows them to perform dialysis therapy wherever and whenever needed. Second, TiO_2 photocatalysis can selectively decompose urea into N_2 and CO_2, ensuring its effective removal from the spent dialysate and reducing the risk of uremic toxin buildup. This selectivity enhances the overall efficiency of dialysis treatments, improving patient outcomes and quality of life. Figure 1.3 shows the device configuration of photodecomposition of the urea reactor (POUR) panel and the proposed urea photo-oxidation reaction at the surface of electrodes in the POUR panel for the wearable dialysis device.

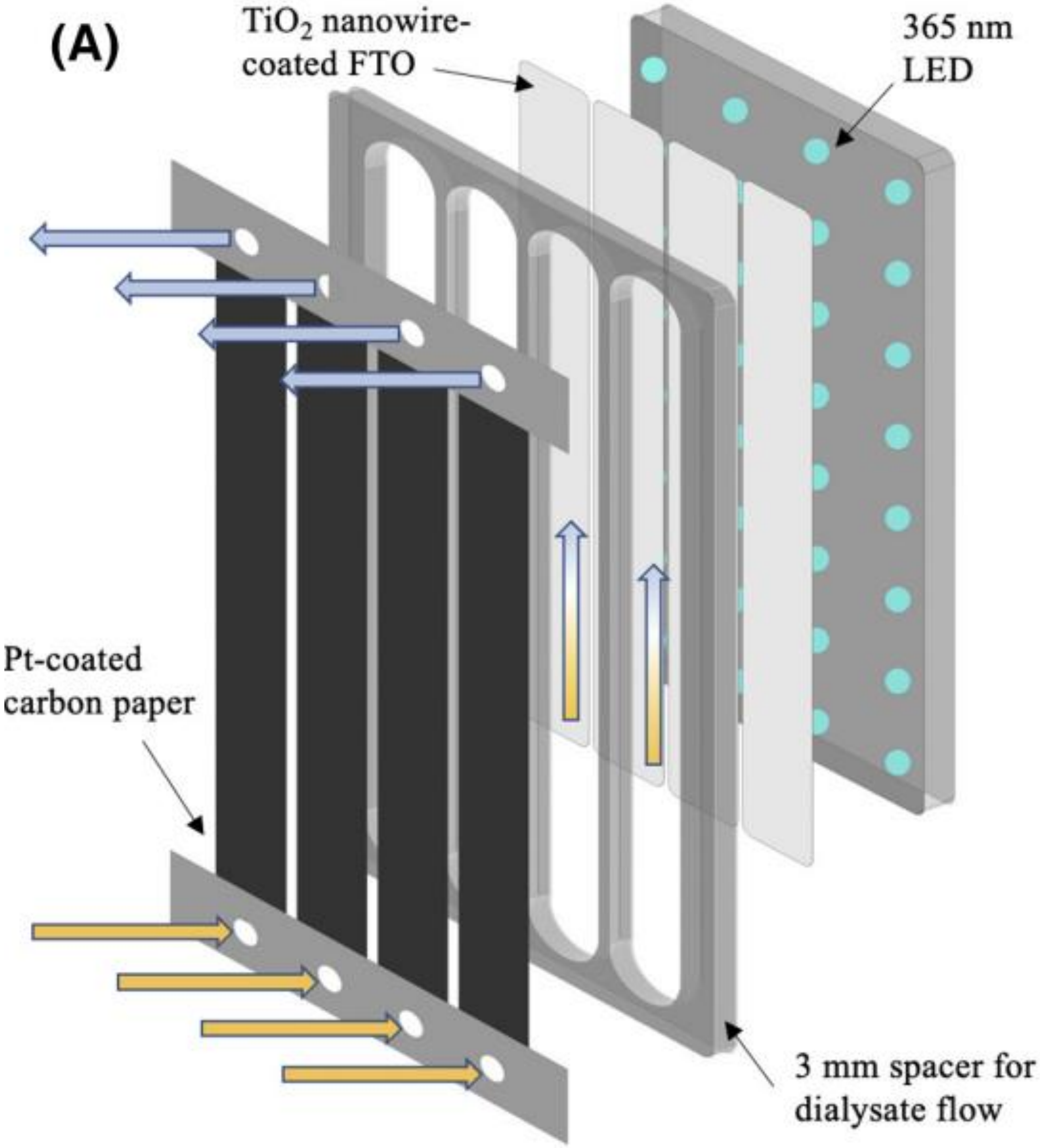

Anode: (TiO_2/FTO): $CO(NH_2)_2 + H_2O + 6e^- + 6h^+ \rightarrow CO_2 + N_2 + 6H^+ + 6e^-_{circuit}$

Cathode: (Pt/Carbonpaper): $\frac{3}{2}O_2 + 3H_2O + 6e^-_{circuit} \rightarrow 6OH^-$

Overall: $CO(NH_2)_2 + \frac{3}{2}O_2 \rightarrow CO_2 + N_2 + 2H_2O$

Figure 1.3. The device configuration of photodecomposition of urea reactor (POUR) panel and the reactions at the surface of both electrodes in POUR; reproduced with permission from ref [1]. Copyright 2022, Wiley.

However, while TiO_2 photocatalysis shows promise for urea decomposition in portable dialysis devices, there is still a need to deepen our understanding of the underlying mechanism. Gaining a comprehensive understanding of the TiO_2 photocatalytic reaction pathway and the role of specific intermediates, such as Cl^-, within the urea photodecomposition process, is crucial. By investigating the intricate details of the TiO_2 photocatalytic mechanism, we can optimize the performance and efficiency of urea decomposition and enhance the overall performance of portable dialysis devices. In addition to understanding the photocatalytic mechanism, it is essential to address the stability concerns associated with TiO_2 performance in urea photodecomposition. The long-term stability and durability of TiO_2 as a photo-active-catalyst can influence its practical application in portable dialysis devices. Factors such as surface poisoning, photo-corrosion, catalyst deactivation, and fouling can impact the efficiency and reliability of TiO_2 photocatalysis over extended periods. Therefore, comprehensive studies on the stability and performance degradation of TiO_2 photocatalysts are necessary to ensure the sustained and optimal performance of TiO_2 for urea decomposition in portable dialysis devices.

To achieve a deeper understanding of the TiO_2 mechanism for urea photodecomposition and address stability concerns, a multidisciplinary approach combining experimental and theoretical investigations is needed. Experimental studies can provide valuable insights into the reaction kinetics, surface chemistry, and interaction between TiO_2, urea and intermediates. Complementary theoretical modeling and computational simulations, such density function theory (DFT), can further elucidate the reaction mechanism at the molecular level, aiding in the design and optimization of TiO_2 photocatalysts for improved stability and performance. By undertaking a comprehensive study of the TiO_2 photocatalytic system, including both the mechanistic aspects and stability considerations, we can pave the way for the development of advanced and reliable portable dialysis devices. These devices would offer efficient and stable urea decomposition, ensuring the effective removal of urea from the spent dialysate and facilitating its regeneration for continuous use. Ultimately, the in-depth understanding of the TiO_2 mechanism and stability properties will contribute to the advancement of portable dialysis technology, bringing us closer to the realization of flexible and convenient renal disease therapy for millions of patients.

Looking towards the future, the development and widespread adoption of portable dialysis devices with integrated dialysate regeneration via TiO_2 photocatalysis hold tremendous promise. These devices have the potential to transform the field of dialysis, empowering patients to lead more flexible and better lives. The ability to perform dialysis therapy at home or while traveling could significantly reduce the burden on patients, improve their overall well-being, and enhance their engagement in daily activities.

In conclusion, the development of portable dialysis devices with integrated dialysate regeneration represents a significant advancement in the field of kidney dialysis. In contrast to early methodologies involving absorbents and enzymes, the incorporation of TiO_2 photocatalysis proves a novel, more efficient and safer approach for urea removal. By harnessing the power of TiO_2 photocatalysis, portable dialysis devices can provide patients with greater mobility, convenience, and improved overall quality of life. Continued research and innovation in this area will undoubtedly shape the future of dialysis treatment and contribute to the well-being of patients with ESRD.

1.2 TiO_2 PHOTOCATALYSIS AND UREA PHOTODECOMPOSITION

TiO_2 photocatalysis has emerged as a powerful and versatile technique for a wide range of applications, driven by its ability to harness solar energy and induce photooxidation reactions under milder conditions with great efficiency and selectivity. Understanding the mechanism of TiO_2 photocatalytic reactions is essential for optimizing its performance, stability and expanding its potential applications. In this section, we will go through some general aspects of TiO_2 photocatalysis, including its discovery as a photocatalyst, applications in different fields, and proposed mechanism for urea photo-oxidation.

The discovery of TiO_2's photocatalytic properties can be traced back to the pioneering work of Fujishima and Honda in 1972 [2]. They observed that TiO_2 electrodes, when illuminated, could split water into hydrogen and oxygen gases. This seminal finding demonstrated the potential of TiO_2 as a photocatalyst, initiating a new era in the field of solar-driven chemical reactions. Since then, extensive research has been conducted to elucidate the underlying mechanisms and exploit the capabilities of TiO_2 photocatalysis.

TiO_2 photocatalysis has found numerous applications across various fields. One prominent application is in environmental remediation, where TiO_2 is employed for the degradation of organic pollutants, such as dyes, pesticides, and pharmaceuticals, present in wastewater and contaminated soil. [3-16] The photocatalytic activity of TiO_2 enables the mineralization of these pollutants into harmless byproducts, offering an environmentally friendly approach to water and soil purification. Beyond environmental remediation, TiO_2 photocatalysis has also proven useful in energy conversion and storage. [9, 12-14, 17-29] It has been extensively studied for solar cell applications as well as the photocatalytic generation of hydrogen from water, providing a sustainable and renewable source of fuel. TiO_2-based photocatalysts have also been explored for the conversion of carbon dioxide (CO_2) into value-added chemicals and fuels [28, 30-34], contributing to efforts in mitigating climate change and achieving a carbon-neutral economy. Additionally, TiO_2 photocatalysis has applications in self-cleaning surfaces [7, 14, 35-37], antibacterial coatings [14, 16, 38-42], and air purification systems [8, 14, 15, 29, 42], among others. The unique properties of TiO_2, such as its high reactivity, stability, and abundance, make it an attractive material for various technological advancements.

When considering the oxidation of urea, we can draw insights from the mechanism of ammonia (NH_3) decomposition on TiO_2 [3, 15, 43-49]. NH_3 possesses a similar $-NH_2$ group with a nitrogen atom bearing a lone pair of electrons, analogous to the structure of urea. Therefore, it is reasonable to speculate that the mechanism of urea photodecomposition on TiO_2 shares similarities with the decomposition of NH_3 on TiO_2. Figure 1.4 illustrated one proposed fundamental reaction mechanisms and pathways involved in the photodecomposition of NH_3 at TiO_2 surface from gaseous and aqueous media. [48]

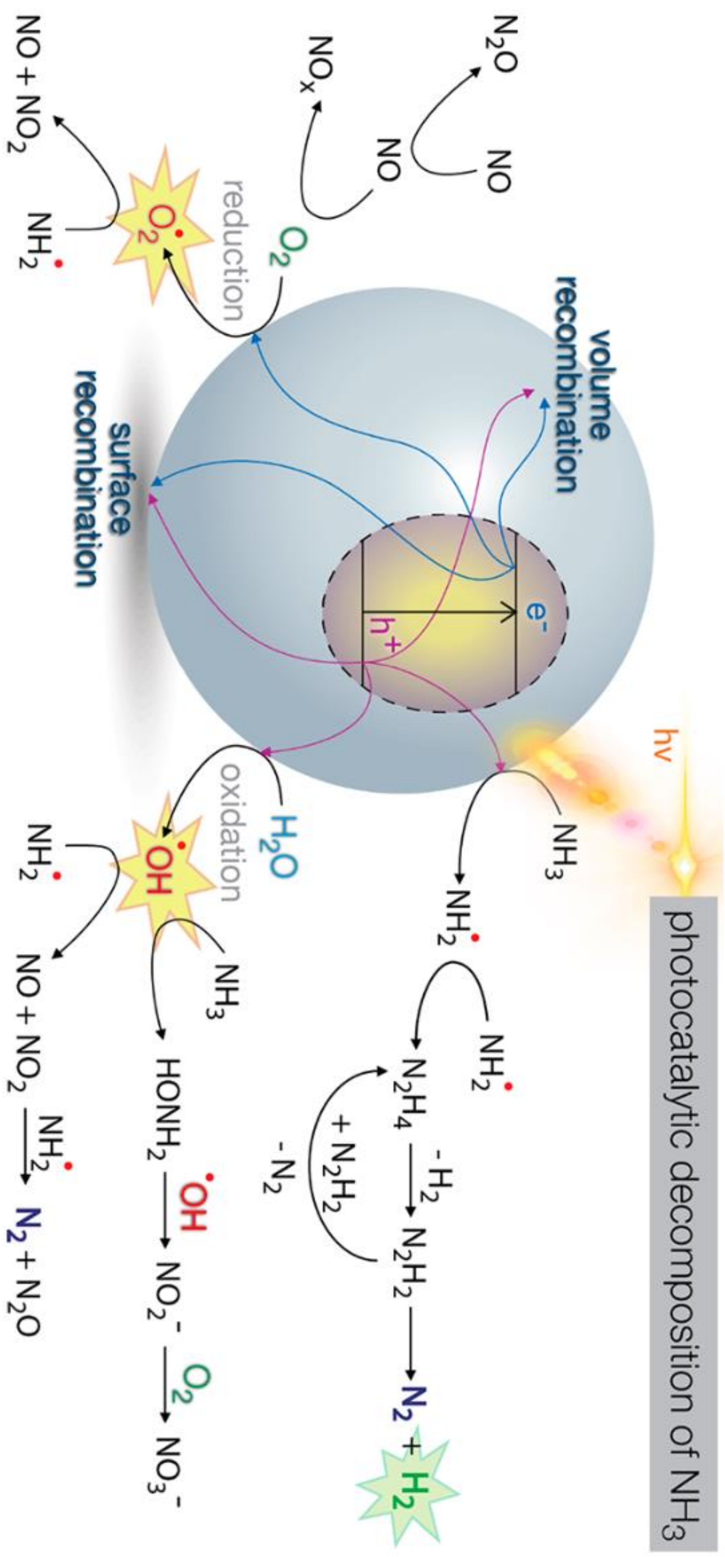

Figure 1.4. Proposed mechanism for NH_3 photodecomposition reaction at TiO_2 surface; reproduced with permission from ref [48]. Copyright 2020, American Chemical Society.

With additional platinum loaded on TiO_2 surface, another group also proposed the reaction mechanism of NH_3 photodecomposition in aqueous/dry condition [49], shown in Figure 1.5.

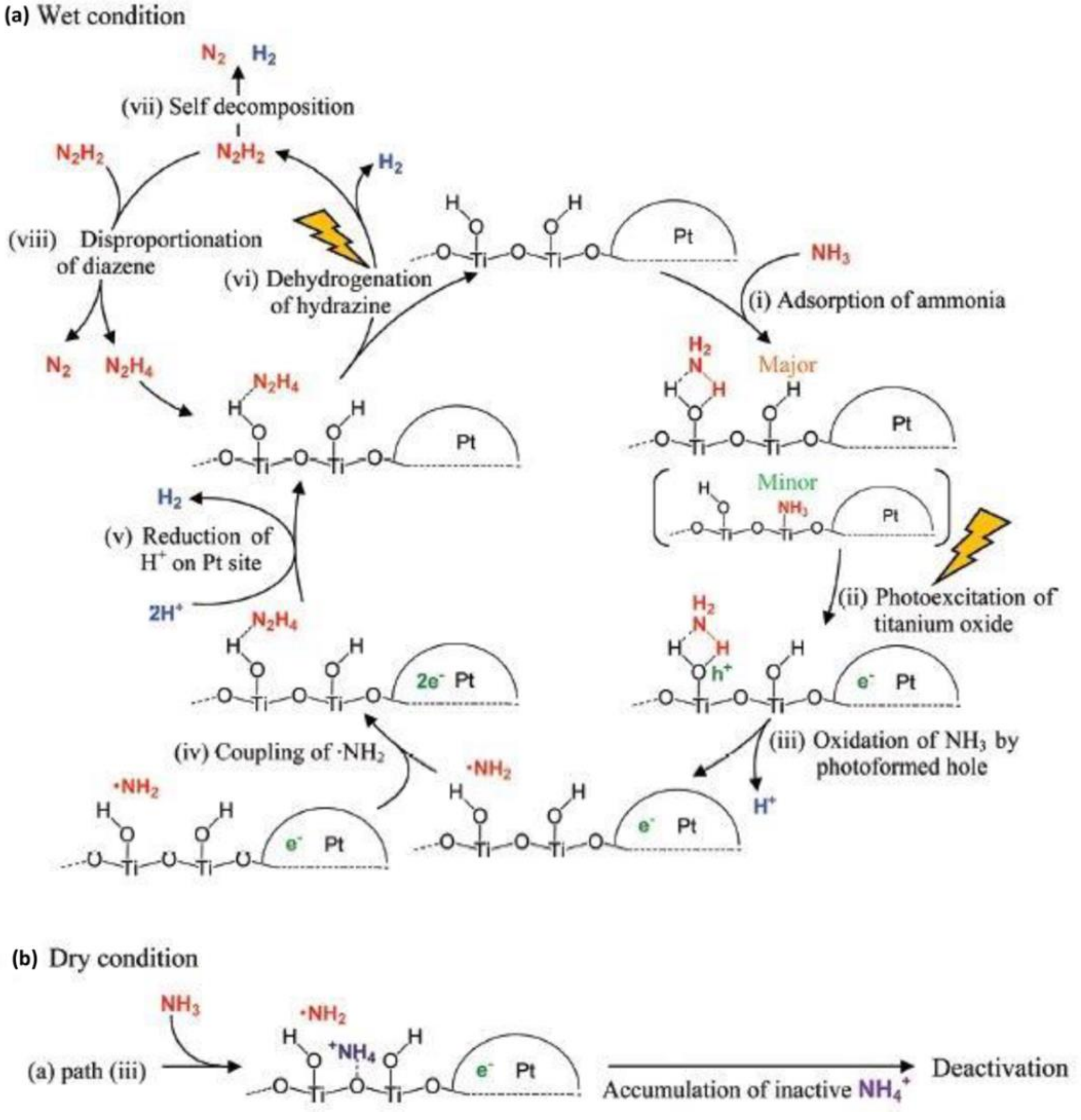

Figure 1.5. Proposed dominant reaction pathway for the photocatalytic decomposition of NH_3 (in the gas phase) on platinum-loaded TiO_2 in the presence of (a) water and (b) in the absence of water; reproduced with permission from ref [49]. Copyright 2012, American Chemical Society.

Figure 1.6 shows the most interesting reaction pathways for NH_3 photodecomposition at TiO_2 surface, which was proposed by a Japanese group in 2017. [45] As can be seen in Figure 1.6, there are three prominent reaction pathways for photodecomposition of NH_3 molecules into H_2 and N_2 gases, which can be considered as a very similar case for urea photodecomposition into N_2 and CO_2 gases, especially for the early NH_3 adsorption stage in all three pathways that two neighboring NH_3 molecules adsorbed closely at TiO_2 surface in order to form N-N or N=N bonding latterly and generate N_2 gas as the final product.

In route 1, two hydrogen atoms are extracted from the adsorbed NH_3 molecules, resulting in the formation of NH· species. The net activation energy required for the NH_3 splitting process through route 1 was estimated to be 236 kcal mol^{-1}. [45] In route 2, after one hydrogen atom was cleaved from NH_3, the two neighboring NH_2· radicals combine to form N_2H_4 species, which further decompose to produce hydrogen. The net activation energy for this NH_3 splitting process via route 2 was estimated to be 74.4 kcal mol^{-1}. [45] Alternatively, a variation of route 2, known as route 2', occurs when the NH_2· radicals react with another NH_3 molecules instead of combining with the neighboring NH_2· radical. The estimated net activation energy for NH_3 splitting through route 2' was 65.8 kcal mol^{-1}. [45] From the activation energies perspective, it is clear that route 1 requires three times more energy than route 2 and 2', indicating that the NH_3 splitting process is less likely to proceed through route 1. Additionally, the difference in activation energies between routes 2 and 2' is minimal. Therefore, from a thermodynamic perspective, it is more favorable for the NH_3-splitting pathway to predominantly adopt routes 2 and 2' to produce hydrogen and nitrogen, illustrated in Figure 1.6 below.

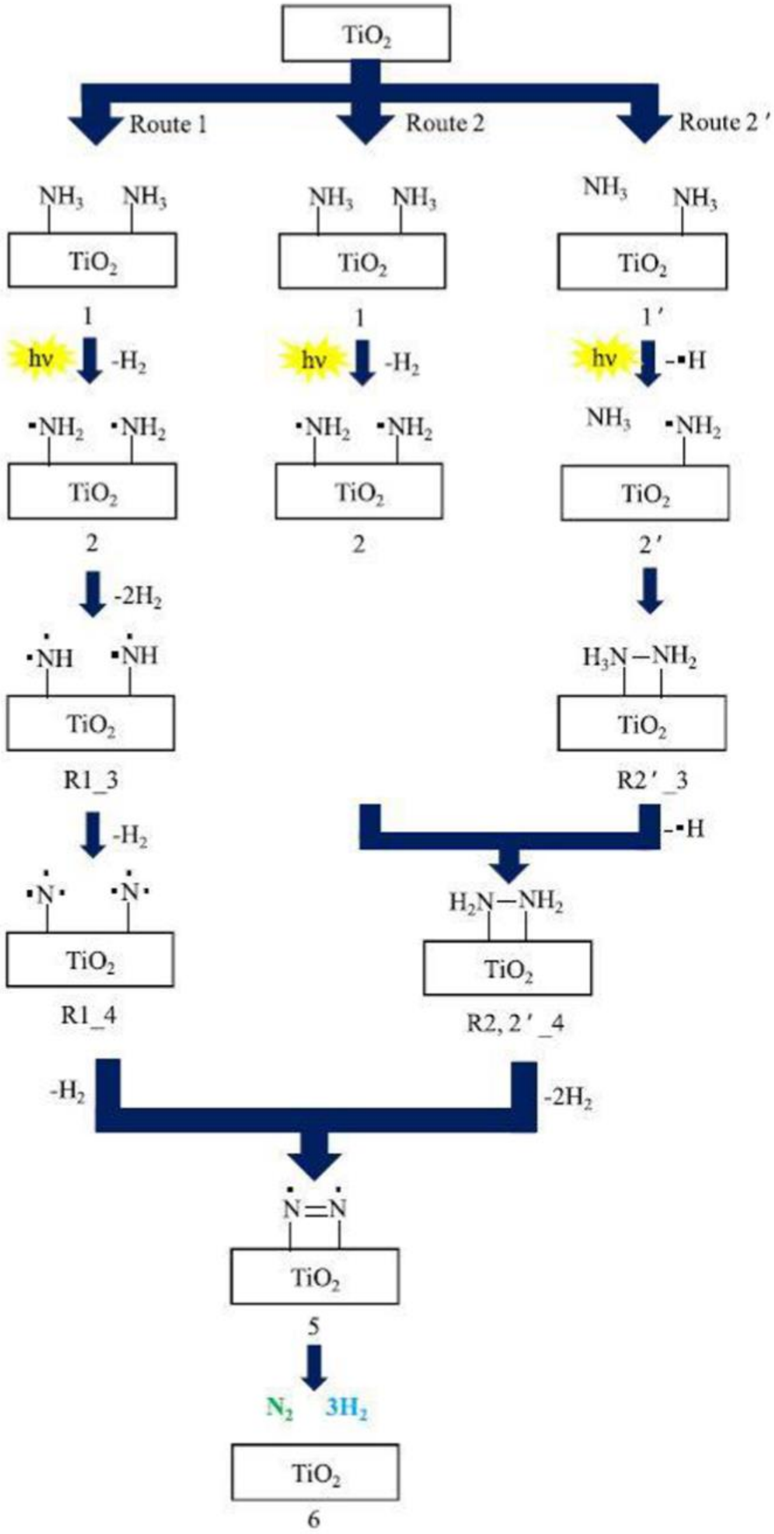

Figure 1.6. Suggested reaction mechanism for NH_3 decomposition to N_2 and H_2 over the TiO_2 photocatalyst; reproduced with permission from ref [45]. Copyright 2017, Elsevier.

Other than investigating the NH_3 photodecomposition mechanism on TiO_2, we also did literature study about the NH_3 photodecomposition mechanism with another photocatalyst, tungsten trioxide (WO_3). [10, 50] NH_3 decomposition on WO_3 involves the reaction of NH_3 with reactive intermediate (Cl·) which originated from Cl^- in solution by reacting with the photoexcited h^+ at WO_3 surface, shown in Figure 1.7. The proposed reactions for the generation of reactive intermediate (Cl·) and the photodecomposition of NH_3 are listed in Figure 1.8.

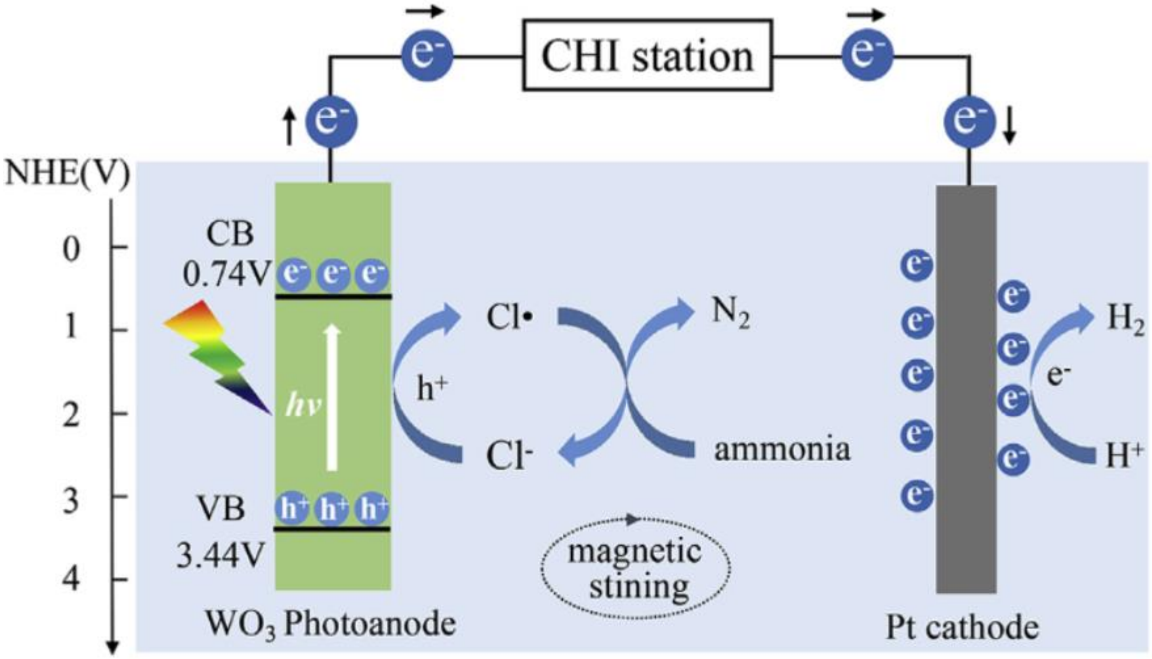

Figure 1.7. The proposed working mechanism of ammonia degradation by the PEC-chloride system; reproduced with permission from ref [50]. Copyright 2017, Elsevier.

$$WO_3 + h\nu \rightarrow h^+ + e^-$$

$$H_2O + h^+ \rightarrow HO\bullet + H^+$$

$$Cl^- + h^+ \rightarrow Cl\bullet$$

$$2Cl^- - 2e^- \rightarrow Cl_2$$

$$Cl_2 + H_2O \rightarrow HClO + HCl$$

$$NH_4^+ + Cl\bullet \rightarrow NH_2\bullet + Cl^- + 2H^+$$

$$NH_2\bullet + HO\text{-}Cl \rightarrow NH_2Cl + HO\bullet$$

$$NH_2Cl + Cl\bullet \rightarrow \bullet NHCl + Cl^- + H^+$$

$$\bullet NHCl + HO\text{-}Cl \rightarrow NHCl_2 + HO\bullet$$

$$NHCl_2 + H_2O \rightarrow NOH + 2H^+ + 2Cl^-$$

$$NHCl_2 + NOH \rightarrow N_2 + HClO + H^+ + Cl^-$$

Figure 1.8. The proposed photocatalytic reactions and pathway for the ammonia nitrogen removal by the PEC-chloride system; reproduced with permission from ref [50]. Copyright 2017, Elsevier.

In this proposed pathway, Cl· is an important reactive intermediate that engages in the NH_3 photodecomposition reaction and is necessary for an efficient ammonia nitrogen degradation in the designed PEC-chloride system. By adding two distinct types of scavengers to quench Cl· or the HO· radicals, this research group proved that the Cl· is the main radical species in the PEC-chlorine process for ammonia nitrogen degradation, and Cl· can selectively oxidize ammonia nitrogen to N_2 and NO_3^-, shown in Figure 1.9.

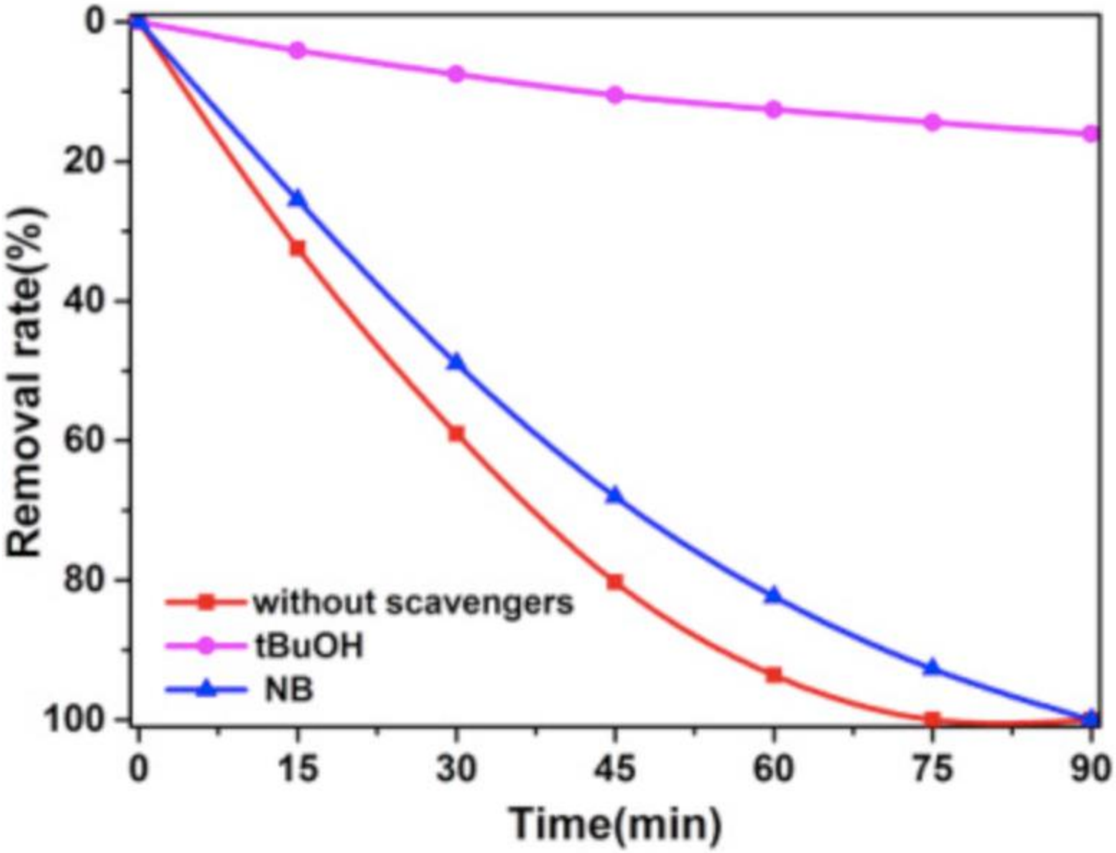

Figure 1.9. Ammonia nitrogen degradation efficiency by PEC-chloride process with different scavengers added; reproduced with permission from ref [50]. Copyright 2017, Elsevier.

By analogizing this mechanism to NH_3 decomposition on WO_3, we can speculate a possible pathway for urea photodecomposition at TiO_2 surface, when we are having 0.15M NaCl in the 10mM urea solution (standard experimental condition for photo-oxidation of urea in our designed wearable dialysis device, POUR). However, it is important to note that urea possesses a more complex molecular structure than NH_3, so potentially it might have additional reaction pathways and intermediates. Further systematic studies are thus needed to investigate the specific mechanisms and to optimize the efficiency of urea photodecomposition on the TiO_2 photocatalysts in order to improve the overall performance of the wearable dialysis device, POUR.

In summary, TiO_2 photocatalysis has emerged as a powerful tool for harnessing solar energy and inducing photooxidation reactions. With applications ranging from environmental remediation to energy conversion, TiO_2 photocatalysis offers a sustainable approach to address pressing global challenges. By drawing insights from the NH_3 decomposition mechanism on TiO_2 /WO_3 and considering the structural similarities between NH_3 and urea, we can speculate on the mechanism of urea photodecomposition on TiO_2. Exploring and understanding the urea photo-oxidation mechanisms experimentally and computationally will pave the way for the development of efficient and selective processes for urea oxidation in our wearable kidney dialysis applications [51, 52].

1.3 GOLD SURFACE PLASMONIC PHOTOCATALYTIC MEMBRANE

Gold nanoparticles have emerged as promising photocatalysts, harnessing the unique catalytic properties of gold in combination with its plasmonic photo-activity. The discovery of gold nanoparticles' plasmonic potential transformed the perception of gold from being primarily inert and stable to exhibiting intriguing photocatalytic properties. This breakthrough can be attributed to the development of synthetic strategies enabling precise control over the size, shape, and surface properties of gold nanoparticles [53-62], shown in Figure 1.10. One of the key phenomena underlying gold plasmonic photocatalysis is the localized surface plasmon resonance (LSPR). As illustrated in Figure 1.11, LSPR refers to the collective oscillation of conduction electrons within a nanoparticle upon interaction with light [60].

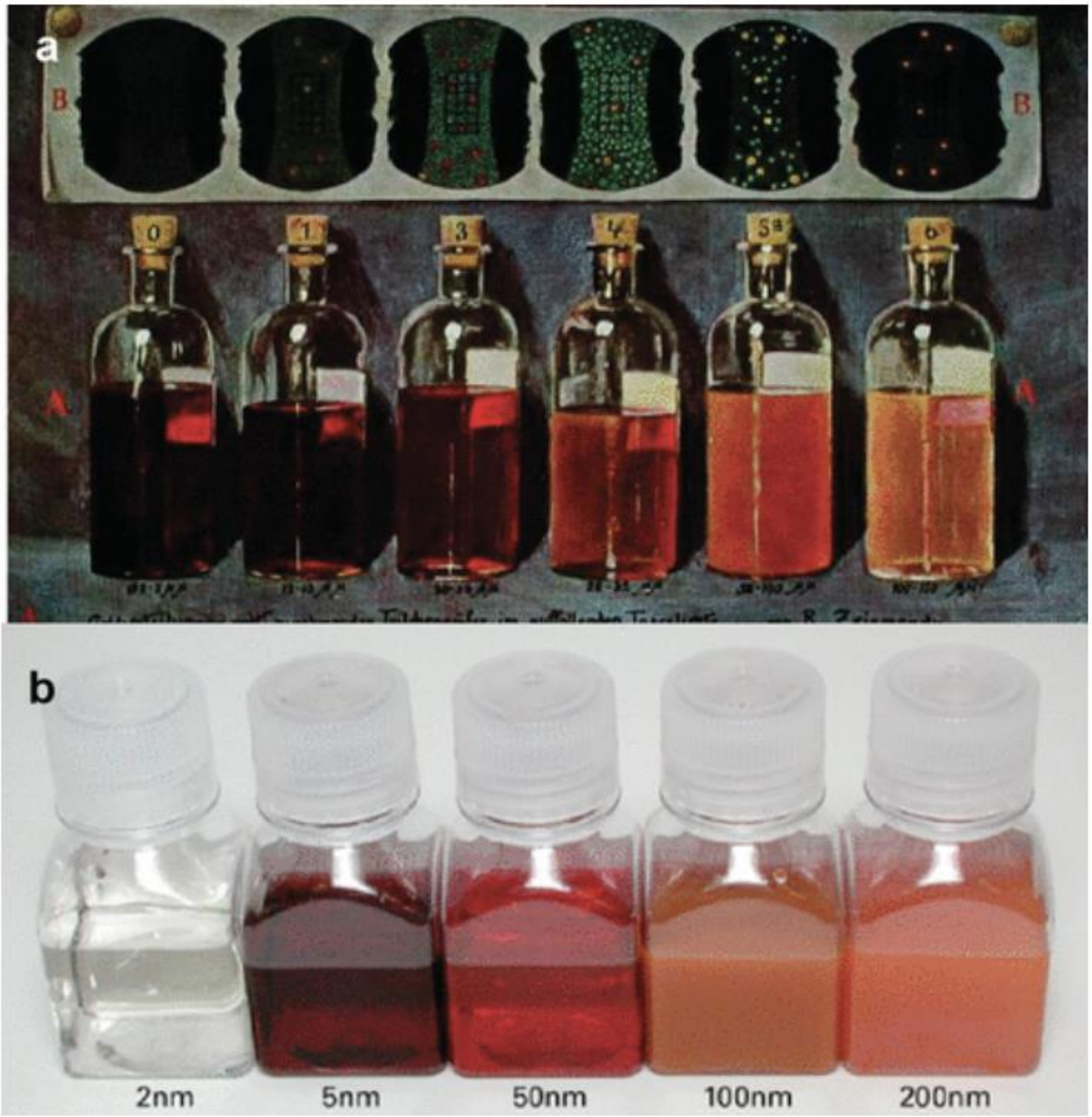

Figure 1.10. Size dependence of gold colloid optical properties. (a) 1909 illustration of dark field scattering of gold colloids of various sizes; (b) Modern photograph of similar colloid solutions (Ted Pella Co.); reproduced with permission from ref [60]. Copyright 2011, American Chemical Society.

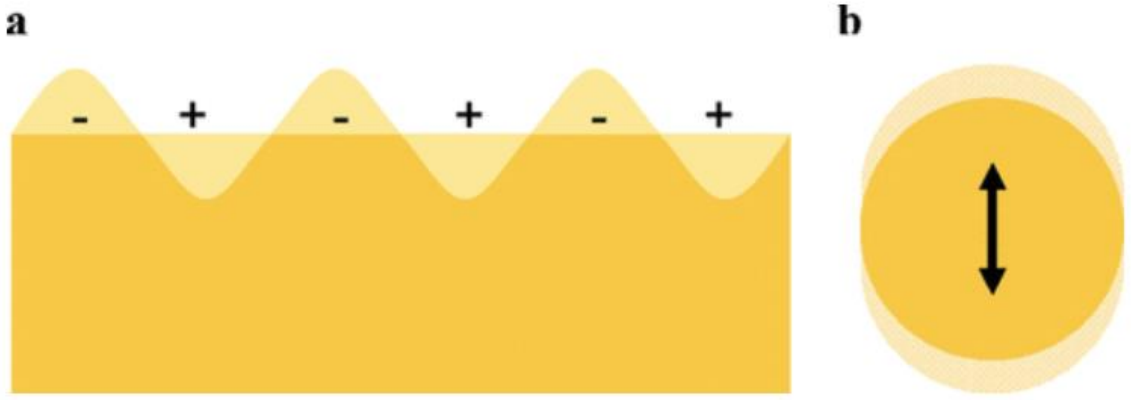

Figure 1.11. Illustrations of (a) surface plasmons and (b) a localized surface plasmon; reproduced with permission from ref [60]. Copyright 2011, American Chemical Society.

Gold nanoparticles exhibit LSPR when their dimensions match the incident light wavelength, leading to the generation of intense and tunable electromagnetic fields near the nanoparticle surface. These enhanced electromagnetic fields play a crucial role in driving chemical reactions by promoting energy transfer and facilitating charge separation. [63-70] These unique properties conferred by LSPR make gold plasmonic photocatalysts highly desirable for numerous applications. In environmental remediation, they have been employed for the degradation of organic pollutants, including dyes and phenolic compounds. The strong plasmonic fields generated by gold nanoparticles enhance light absorption, enabling efficient photooxidation reactions and the degradation of organic contaminants. [71-75] Gold plasmonic photocatalysts also hold enormous potential in energy conversion and storage. They have been extensively studied for the photocatalytic generation of hydrogen from water, leveraging the plasmon-induced enhancement of light absorption and charge separation. Gold-based photocatalysts address the need for sustainable and renewable energy sources by converting solar energy into chemical fuels with a much broader range of light absorption. [67, 69, 76-78] Moreover, gold plasmonic photocatalysis exhibits promise in chemical synthesis and catalysis. The localized electromagnetic fields generated by gold nanoparticles promote specific chemical reactions, such as selective oxidation and reduction processes, in a more precise pathway. [74, 79-81] This unique property has been harnessed for the synthesis of various value-added chemicals, including fine chemicals, pharmaceutical intermediates, and high-value products. Figure 1.12 shows an example of utilizing the LSPR of gold nanoparticles to achieve chemical synthesis under a mild and controllable approach.

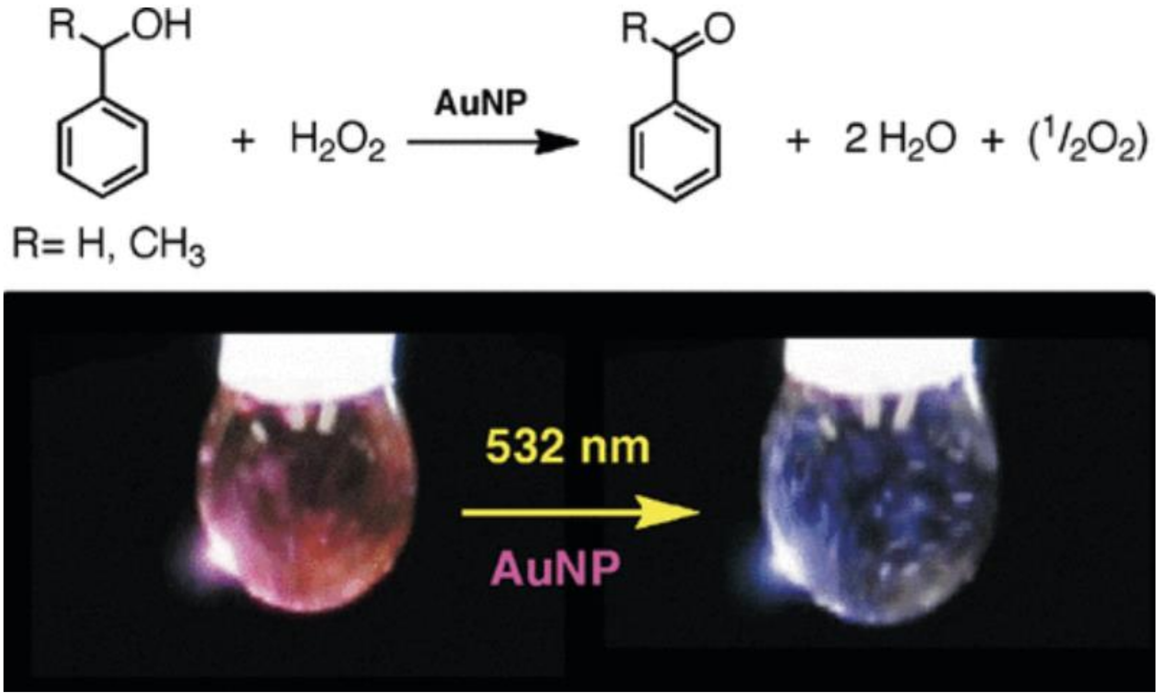

Figure 1.12. Overall reaction pathway for AuNP plasmon-dedicated oxidation of benzylic alcohols in the presence of H_2O_2 and the color of the laser drop sample before and after a single pulse of 532 nm laser excitation; reproduced with permission from ref [79]. Copyright 2011, American Chemical Society.

Looking towards the future, gold plasmonic photocatalysis offers exciting prospects for further advancement. The development of novel nanostructures, such as core-shell configurations and hybrid materials, can enhance photocatalytic performance and broaden the range of light absorption harvested from solar energy. The integration of gold plasmonic photocatalysts with other functional materials, such as membranes or conductive metal oxides, holds the potential for improved plasmonic photocatalytic performance and more applications in different fields.

In conclusion, gold plasmonic photocatalysis represents a rapidly evolving field at the intersection of plasmonics and catalysis. The discovery of gold nanoparticles as efficient photocatalysts and the understanding of LSPR have paved the way for their utilization in various applications, including environmental remediation, energy conversion, and chemical synthesis. Ongoing research and innovation in gold plasmonic photocatalysis hold tremendous potential for addressing critical societal and economic challenges and driving sustainable technological advancements in the future.

1.4 REFERENCE

[1] Shao, G.; Himmelfarb, J.; Hinds, B. J. Strategies for optimizing urea removal to enable portable kidney dialysis: A reappraisal. Artificial Organs 2022, 46 (6), 997-1011.

[2] Fujishima, A.; Honda, K. Electrochemical photolysis of water at a semiconductor electrode. nature 1972, 238 (5358), 37-38.

[3] Wang, H.; Zhang, X.; Su, Y.; Yu, H.; Chen, S.; Quan, X.; Yang, F. Photoelectrocatalytic oxidation of aqueous ammonia using TiO2 nanotube arrays. Applied Surface Science 2014, 311, 851-857.

[4] Kalantari, K.; Kalbasi, M.; Sohrabi, M.; Royaee, S. J. Synthesis and characterization of N-doped TiO2 nanoparticles and their application in photocatalytic oxidation of dibenzothiophene under visible light. Ceramics International 2016, 42 (13), 14834-14842.

[5] Lee, S.-Y.; Park, S.-J. TiO2 photocatalyst for water treatment applications. Journal of industrial and engineering chemistry 2013, 19 (6), 1761-1769.

[6] Al-Mamun, M.; Kader, S.; Islam, M.; Khan, M. Photocatalytic activity improvement and application of UV-TiO2 photocatalysis in textile wastewater treatment: A review. Journal of Environmental Chemical Engineering 2019, 7 (5), 103248.

[7] Nakata, K.; Fujishima, A. TiO2 photocatalysis: Design and applications. Journal of photochemistry and photobiology C: Photochemistry Reviews 2012, 13 (3), 169-189.

[8] Paz, Y. Application of TiO2 photocatalysis for air treatment: Patents' overview. Applied Catalysis B: Environmental 2010, 99 (3-4), 448-460.

[9] Fan, Y.; Hu, G.; Yu, S.; Mai, L.; Xu, L. Recent advances in TiO2 nanoarrays/graphene for water treatment and energy conversion/storage. Sci China Mater 2019, 62 (3), 325-340.

[10] Fernandes, E.; Gomes, J.; Martins, R. C. Semiconductors Application Forms and Doping Benefits to Wastewater Treatment: A Comparison of TiO2, WO3, and g-C3N4. Catalysts 2022, 12 (10), 1218.

[11] Han, F.; Kambala, V. S. R.; Srinivasan, M.; Rajarathnam, D.; Naidu, R. Tailored titanium dioxide photocatalysts for the degradation of organic dyes in wastewater treatment: a review. Applied Catalysis A: General 2009, 359 (1-2), 25-40.

[12] Ong, W. J.; Tan, L. L.; Chai, S. P.; Yong, S. T.; Mohamed, A. R. Facet-dependent photocatalytic properties of TiO2-based composites for energy conversion and environmental remediation. ChemSusChem 2014, 7 (3), 690-719.

[13] Henderson, M. A. A surface science perspective on TiO2 photocatalysis. Surface Science Reports 2011, 66 (6-7), 185-297.

[14] Fujishima, A.; Zhang, X.; Tryk, D. A. TiO2 photocatalysis and related surface phenomena. Surface science reports 2008, 63 (12), 515-582.

[15] Ochiai, T.; Fujishima, A. Photoelectrochemical properties of TiO2 photocatalyst and its applications for environmental purification. Journal of Photochemistry and photobiology C: Photochemistry reviews 2012, 13 (4), 247-262.

[16] Richards, T.; Harrhy, J. H.; Lewis, R. J.; Howe, A. G.; Suldecki, G. M.; Folli, A.; Morgan, D. J.; Davies, T. E.; Loveridge, E. J.; Crole, D. A. A residue-free approach to water disinfection using catalytic in situ generation of reactive oxygen species. Nature Catalysis 2021, 4 (7), 575-585.

[17] Wang, Z.-S.; Kawauchi, H.; Kashima, T.; Arakawa, H. Significant influence of TiO2 photoelectrode morphology on the energy conversion efficiency of N719 dye-sensitized solar cell. Coordination chemistry reviews 2004, 248 (13-14), 1381-1389.

[18] Huang, F.; Hou, J.; Wang, H.; Tang, H.; Liu, Z.; Zhang, L.; Zhang, Q.; Peng, S.; Liu, J.; Cao, G. Impacts of surface or interface chemistry of ZnSe passivation layer on the performance of CdS/CdSe quantum dot sensitized solar cells. Nano Energy 2017, 32, 433-440.

[19] Kumar, A.; Choudhary, P.; Kumar, A.; Camargo, P. H.; Krishnan, V. Recent advances in plasmonic photocatalysis based on TiO2 and noble metal nanoparticles for energy conversion, environmental remediation, and organic synthesis. Small 2022, 18 (1), 2101638.

[20] Frank, A. J.; Kopidakis, N.; Van De Lagemaat, J. Electrons in nanostructured TiO2 solar cells: transport, recombination and photovoltaic properties. Coordination Chemistry Reviews 2004, 248 (13-14), 1165-1179.

[21] Roy, P.; Kim, D.; Lee, K.; Spiecker, E.; Schmuki, P. TiO2 nanotubes and their application in dye-sensitized solar cells. Nanoscale 2010, 2 (1), 45-59.

[22] Mora-Seró, I.; Giménez, S.; Fabregat-Santiago, F.; Gómez, R.; Shen, Q.; Toyoda, T.; Bisquert, J. Recombination in quantum dot sensitized solar cells. Accounts of chemical research 2009, 42 (11), 1848-1857.

[23] Mor, G. K.; Varghese, O. K.; Paulose, M.; Shankar, K.; Grimes, C. A. A review on highly ordered, vertically oriented TiO2 nanotube arrays: Fabrication, material properties, and solar energy applications. Solar Energy Materials and Solar Cells 2006, 90 (14), 2011-2075.

[24] Ni, M.; Leung, M. K.; Leung, D. Y.; Sumathy, K. A review and recent developments in photocatalytic water-splitting using TiO2 for hydrogen production. Renewable and Sustainable Energy Reviews 2007, 11 (3), 401-425.

[25] Ge, M.; Li, Q.; Cao, C.; Huang, J.; Li, S.; Zhang, S.; Chen, Z.; Zhang, K.; Al-Deyab, S. S.; Lai, Y. One-dimensional TiO2 nanotube photocatalysts for solar water splitting. Advanced science 2017, 4 (1), 1600152.

[26] Abed, J.; Rajput, N. S.; Moutaouakil, A. E.; Jouiad, M. Recent advances in the design of plasmonic Au/TiO2 nanostructures for enhanced photocatalytic water splitting. Nanomaterials 2020, 10 (11), 2260.

[27] Zhou, D.; Chen, Z.; Gao, T.; Niu, F.; Qin, L.; Huang, Y. Hydrogen Generation from Water Splitting on TiO2 Nanotube-Array-Based Photocatalysts. Energy Technology 2015, 3 (9), 888-895.

[28] Sakar, M.; Mithun Prakash, R.; Do, T.-O. Insights into the TiO2-based photocatalytic systems and their mechanisms. Catalysts 2019, 9 (8), 680.

[29] Nakata, K.; Ochiai, T.; Murakami, T.; Fujishima, A. Photoenergy conversion with TiO2 photocatalysis: New materials and recent applications. Electrochimica Acta 2012, 84, 103-111.

[30] Habisreutinger, S. N.; Schmidt-Mende, L.; Stolarczyk, J. K. Photocatalytic reduction of CO2 on TiO2 and other semiconductors. Angewandte Chemie International Edition 2013, 52 (29), 7372-7408.

[31] Low, J.; Cheng, B.; Yu, J. Surface modification and enhanced photocatalytic CO2 reduction performance of TiO2: a review. Applied Surface Science 2017, 392, 658-686.

[32] Ola, O.; Maroto-Valer, M. M. Review of material design and reactor engineering on TiO2 photocatalysis for CO2 reduction. Journal of Photochemistry and Photobiology C: Photochemistry Reviews 2015, 24, 16-42.

[33] Kočí, K.; Matějů, K.; Obalová, L.; Krejčíková, S.; Lacný, Z.; Plachá, D.; Čapek, L.; Hospodková, A.; Šolcová, O. Effect of silver doping on the TiO2 for photocatalytic reduction of CO2. Applied Catalysis B: Environmental 2010, 96 (3-4), 239-244.

[34] Al Jitan, S.; Palmisano, G.; Garlisi, C. Synthesis and surface modification of TiO2-based photocatalysts for the conversion of CO2. Catalysts 2020, 10 (2), 227.

[35] Banerjee, S.; Dionysiou, D. D.; Pillai, S. C. Self-cleaning applications of TiO2 by photo-induced hydrophilicity and photocatalysis. Applied Catalysis B: Environmental 2015, 176, 396-428.

[36] Zhao, X.; Zhao, Q.; Yu, J.; Liu, B. Development of multifunctional photoactive self-cleaning glasses. Journal of Non-Crystalline Solids 2008, 354 (12-13), 1424-1430.

[37] Nishimoto, S.; Bhushan, B. Bioinspired self-cleaning surfaces with superhydrophobicity, superoleophobicity, and superhydrophilicity. Rsc Advances 2013, 3 (3), 671-690.

[38] Prakash, J.; Sun, S.; Swart, H. C.; Gupta, R. K. Noble metals-TiO2 nanocomposites: from fundamental mechanisms to photocatalysis, surface enhanced Raman scattering and antibacterial applications. Applied Materials Today 2018, 11, 82-135.

[39] Kunrath, M. F.; Leal, B. F.; Hubler, R.; de Oliveira, S. D.; Teixeira, E. R. Antibacterial potential associated with drug-delivery built TiO2 nanotubes in biomedical implants. AMB Express 2019, 9 (1), 1-13.

[40] Yadav, H. M.; Kim, J.-S.; Pawar, S. H. Developments in photocatalytic antibacterial activity of nano TiO 2: A review. Korean Journal of Chemical Engineering 2016, 33, 1989-1998.

[41] Visai, L.; De Nardo, L.; Punta, C.; Melone, L.; Cigada, A.; Imbriani, M.; Arciola, C. R. Titanium oxide antibacterial surfaces in biomedical devices. The International journal of artificial organs 2011, 34 (9), 929-946.

[42] Su, E.; Justin, D.; Pratt, C.; Sarin, V.; Nguyen, V.; Oh, S.; Jin, S. Effects of titanium nanotubes on the osseointegration, cell differentiation, mineralisation and antibacterial properties of orthopaedic implant surfaces. The bone & joint journal 2018, 100 (1_Supple_A), 9-16.

[43] Yasuda, M.; Matsumoto, T.; Yamashita, T. Sacrificial hydrogen production over TiO2-based photocatalysts: Polyols, carboxylic acids, and saccharides. Renewable and Sustainable Energy Reviews 2018, 81, 1627-1635.

[44] Nemoto, J.; Gokan, N.; Ueno, H.; Kaneko, M. Photodecomposition of ammonia to dinitrogen and dihydrogen on platinized TiO2 nanoparticules in an aqueous solution. Journal of Photochemistry and Photobiology A: Chemistry 2007, 185 (2-3), 295-300.

[45] Utsunomiya, A.; Okemoto, A.; Nishino, Y.; Kitagawa, K.; Kobayashi, H.; Taniya, K.; Ichihashi, Y.; Nishiyama, S. Mechanistic study of reaction mechanism on ammonia photodecomposition over Ni/TiO2 photocatalysts. Applied Catalysis B: Environmental 2017, 206, 378-383.

[46] Kebede, M. A.; Varner, M. E.; Scharko, N. K.; Gerber, R. B.; Raff, J. D. Photooxidation of Ammonia on TiO2 as a Source of NO and NO2 under Atmospheric Conditions. Journal of the American Chemical Society 2013, 135 (23), 8606-8615.

[47] Morranega, H.; Herrmann, J.; Pichat, P. NH3 oxidation over UV-irradiated TiO2 at room temperature. The Journal of Physical Chemistry 1979, 83, 2251-2255.

[48] Vikrant, K.; Kim, K.-H.; Dong, F.; Giannakoudakis, D. A. Photocatalytic platforms for removal of ammonia from gaseous and aqueous matrixes: status and challenges. ACS Catalysis 2020, 10 (15), 8683-8716.

[49] Yuzawa, H.; Mori, T.; Itoh, H.; Yoshida, H. Reaction mechanism of ammonia decomposition to nitrogen and hydrogen over metal loaded titanium oxide photocatalyst. The Journal of Physical Chemistry C 2012, 116 (6), 4126-4136.

[50] Ji, Y.; Bai, J.; Li, J.; Luo, T.; Qiao, L.; Zeng, Q.; Zhou, B. Highly selective transformation of ammonia nitrogen to N2 based on a novel solar-driven photoelectrocatalytic-chlorine radical reactions system. Water research 2017, 125, 512-519.

[51] Shao, G.; Tang, H.; Ren, S.; Creason, S. A.; Faisal, S.; Galperin, A.; Aliseda, A.; Gao, D.; Ratner, B.; Hinds, B. J. Dialysate regeneration via urea photodecomposition with TiO2 nanowires at therapeutic rates. Artificial Organs 2023.

[52] Shao, G.; Tang, H.; Ren, S.; Creason, S. A.; Gao, D.; Ratner, B. D.; Hinds, B. J. Dialysate Regeneration with Urea Selective Membrane Coupled to Photoelectrochemical Oxidation System. Advanced Materials Interfaces 2022, 9 (13), 2102308.

[53] Amendola, V.; Pilot, R.; Frasconi, M.; Maragò, O. M.; Iatì, M. A. Surface plasmon resonance in gold nanoparticles: a review. Journal of Physics: Condensed Matter 2017, 29 (20), 203002.

[54] Ghosh, S. K.; Pal, T. Interparticle coupling effect on the surface plasmon resonance of gold nanoparticles: from theory to applications. Chemical reviews 2007, 107 (11), 4797-4862.

[55] Eustis, S.; El-Sayed, M. A. Why gold nanoparticles are more precious than pretty gold: noble metal surface plasmon resonance and its enhancement of the radiative and nonradiative properties of nanocrystals of different shapes. Chemical society reviews 2006, 35 (3), 209-217.

[56] Qian, H.; Zhu, Y.; Jin, R. Atomically precise gold nanocrystal molecules with surface plasmon resonance. Proceedings of the National Academy of Sciences 2012, 109 (3), 696-700.

[57] Shi, W.; Sahoo, Y.; Swihart, M. T.; Prasad, P. Gold nanoshells on polystyrene cores for control of surface plasmon resonance. Langmuir 2005, 21 (4), 1610-1617.

[58] Iida, K.; Noda, M.; Ishimura, K.; Nobusada, K. First-principles computational visualization of localized surface plasmon resonance in gold nanoclusters. The Journal of Physical Chemistry A 2014, 118 (47), 11317-11322.

[59] Nishijima, Y.; Rosa, L.; Juodkazis, S. Surface plasmon resonances in periodic and random patterns of gold nano-disks for broadband light harvesting. Optics express 2012, 20 (10), 11466-11477.

[60] Mayer, K. M.; Hafner, J. H. Localized surface plasmon resonance sensors. Chemical reviews 2011, 111 (6), 3828-3857.

[61] Willets, K. A.; Van Duyne, R. P. Localized surface plasmon resonance spectroscopy and sensing. Annu. Rev. Phys. Chem. 2007, 58, 267-297.

[62] Tian, Z. Q.; Ren, B.; Wu, D. Y. Surface-enhanced Raman scattering: From noble to transition metals and from rough surfaces to ordered nanostructures. Journal of Physical Chemistry B 2002, 106 (37), 9463-9483. DOI: 10.1021/jp0257449.

[63] Zhou, L.; Swearer, D. F.; Zhang, C.; Robatjazi, H.; Zhao, H.; Henderson, L.; Dong, L.; Christopher, P.; Carter, E. A.; Nordlander, P.; et al. Quantifying hot carrier and thermal contributions in plasmonic photocatalysis. Science 2018, 362 (6410), 69-+. DOI: 10.1126/science.aat6967.

[64] Liu, J. G.; Zhang, H.; Link, S.; Nordlander, P. Relaxation of Plasmon-Induced Hot Carriers. Acs Photonics 2018, 5 (7), 2584-2595. DOI: 10.1021/acsphotonics.7b00881.

[65] Zheng, B. Y.; Zhao, H.; Manjavacas, A.; McClain, M.; Nordlander, P.; Halas, N. J. Distinguishing between plasmon-induced and photoexcited carriers in a device geometry. Nature Communications 2015, 6. DOI: 10.1038/ncomms8797.

[66] Linic, S.; Aslam, U.; Boerigter, C.; Morabito, M. Photochemical transformations on plasmonic metal nanoparticles. Nature Materials 2015, 14 (6), 567-576. DOI: 10.1038/nmat4281.

[67] Linic, S.; Christopher, P.; Ingram, D. B. Plasmonic-metal nanostructures for efficient conversion of solar to chemical energy. Nature Materials 2011, 10 (12), 911-921. DOI: 10.1038/nmat3151.

[68] Mubeen, S.; Lee, J.; Singh, N.; Kraemer, S.; Stucky, G. D.; Moskovits, M. An autonomous photosynthetic device in which all charge carriers derive from surface plasmons. Nature Nanotechnology 2013, 8 (4), 247-251. DOI: 10.1038/nnano.2013.18.

[69] Aslam, U.; Rao, V. G.; Chavez, S.; Linic, S. Catalytic conversion of solar to chemical energy on plasmonic metal nanostructures. Nature Catalysis 2018, 1 (9), 656-665. DOI: 10.1038/s41929-018-0138-x.

[70] Zhan, C.; Chen, X.-J.; Yi, J.; Li, J.-F.; Wu, D.-Y.; Tian, Z.-Q. From plasmon-enhanced molecular spectroscopy to plasmon-mediated chemical reactions. Nature Reviews Chemistry 2018, 2 (9), 216-230. DOI: 10.1038/s41570-018-0031-9.

[71] Swearer, D. F.; Robatjazi, H.; Martirez, J. M. P.; Zhang, M.; Zhou, L.; Carter, E. A.; Nordlander, P.; Halas, N. J. Plasmonic Photocatalysis of Nitrous Oxide into N-2 and O-2 Using Aluminum-Iridium Antenna-Reactor Nanoparticles. Acs Nano 2019, 13 (7), 8076-8086. DOI: 10.1021/acsnano.9b02924.

[72] Ballarin, B.; Barreca, D.; Boanini, E.; Cassani, M. C.; Dambruoso, P.; Massi, A.; Mignani, A.; Nanni, D.; Parise, C.; Zaghi, A. Supported Gold Nanoparticles for Alcohols Oxidation in Continuous Flow Heterogeneous Systems. Acs Sustainable Chemistry & Engineering 2017, 5 (6), 4746-4756. DOI: 10.1021/acssuschemeng.7b00133.

[73] Christopher, P.; Xin, H.; Marimuthu, A.; Linic, S. Singular characteristics and unique chemical bond activation mechanisms of photocatalytic reactions on plasmonic nanostructures. Nature Materials 2012, 11 (12), 1044-1050. DOI: 10.1038/nmat3454.

[74] Seemala, B.; Therrien, A. J.; Lou, M. H.; Li, K.; Finzel, J. P.; Qi, J.; Nordlander, P.; Christopher, P. Plasmon-Mediated Catalytic O-2 Dissociation on Ag Nanostructures: Hot Electrons or Near Fields? Acs Energy Letters 2019, 4 (8), 1803-1809, Article. DOI: 10.1021/acsenergylett.9b00990.

[75] Sun, Y.; Xia, Y. Increased sensitivity of surface plasmon resonance of gold nanoshells compared to that of gold solid colloids in response to environmental changes. Analytical chemistry 2002, 74 (20), 5297-5305.

[76] Mukherjee, S.; Libisch, F.; Large, N.; Neumann, O.; Brown, L. V.; Cheng, J.; Lassiter, J. B.; Carter, E. A.; Nordlander, P.; Halas, N. J. Hot Electrons Do the Impossible: Plasmon-Induced Dissociation of H-2 on Au. Nano Letters 2013, 13 (1), 240-247. DOI: 10.1021/nl303940z.

[77] Robatjazi, H.; Zhao, H.; Swearer, D. F.; Hogan, N. J.; Zhou, L.; Alabastri, A.; McClain, M. J.; Nordlander, P.; Halas, N. J. Plasmon-induced selective carbon dioxide conversion on earth-abundant aluminum-cuprous oxide antenna-reactor nanoparticles. Nature Communications 2017, 8. DOI: 10.1038/s41467-017-00055-z.

[78] Choi, C. H.; Chung, K.; Nguyen, T.-T. H.; Kim, D. H. Plasmon-Mediated Electrocatalysis for Sustainable Energy: From Electrochemical Conversion of Different Feedstocks to Fuel Cell Reactions. Acs Energy Letters 2018, 3 (6), 1415-1433. DOI: 10.1021/acsenergylett.8b00461.

[79] Hallett-Tapley, G. L.; Silvero, M. J.; Gonzalez-Bejar, M.; Grenier, M.; Netto-Ferreira, J. C.; Scaiano, J. C. Plasmon-Mediated Catalytic Oxidation of sec-Phenethyl and Benzyl Alcohols. Journal of Physical Chemistry C 2011, 115 (21), 10784-10790. DOI: 10.1021/jp202769a.

[80] Huang, Q.; Hu, S.; Zhuang, J.; Wang, X. MoO3–x-based hybrids with tunable localized surface plasmon resonances: chemical oxidation driving transformation from ultrathin nanosheets to nanotubes. Chemistry–A European Journal 2012, 18 (48), 15283-15287.

[81] Huang, Y. F.; Zhang, M.; Zhao, L. B.; Feng, J. M.; Wu, D. Y.; Ren, B.; Tian, Z. Q. Activation of oxygen on gold and silver nanoparticles assisted by surface plasmon resonances. Angewandte Chemie 2014, 126 (9), 2385-2389.

Chapter 2. REGENERATION OF TiO_2 PHOTOCATALYTIC ACTIVITY FOR UREA OXIDATION TO ENABLE CONTINUOUS PORTABLE KIDNEY DIALYSIS

Adapted from Hao Tang, Guozheng Shao, and Bruce J. Hinds. "Regeneration of TiO_2 Photocatalytic Activity for Urea Oxidation to Enable Continuous Portable Kidney Dialysis." Manuscript ready for submission.

2.1 BACKGROUND

There are over 500,000 prevalent cases of end-stage renal disease (ESRD) in the United States using hemodialysis (HD) with a per person per year spending of \$10,000-90,000. Despite an over \$50 billion spending in the United States alone, the 5-year survival rate is only 35% largely due to non-physiological conditions of the treatment and infections [1][2]. For a conventional HD treatment, it is intermittent, with 3 to 4 hours treatment, three times a week. Treatment approaches are similar to those of the 1970's and require over 120kg of dialysate to be produced and disposed of. This precludes use as a portable and continuous HD treatment option that would improve quality of life and reduce clinic related treatment costs. This concept of regenerating the spent dialysate was first suggested by A. Johnson in 1966[3], and the regenerative dialysis (REDY) enzyme/sorbent system was one of the first generation of wearable dialysis devices dialysate regeneration and recirculation [3-5]. However, REDY based machines were only on the market for about ten years from 1984 to 1994[4], due to enzyme stability and high cost of dual ion exchange sorbents for the produced ammonia. Photocatalytic urea decomposition can be another effective way to remove urea from the dialysate and thus regenerate the spent dialysate in a wearable dialysis device system.[6] TiO_2-mediated photooxidation has been used for environmental remediation of organics, even when those toxic materials are at low concentrations. [7-14] For high concentration agricultural applications, a urea removal system of UV irradiation onto colloidal TiO_2 in an electrochemical cell was able to decompose urea into physiologically safe O_2 and N_2. However, the current density performance was two orders of magnitude less than needed for application in dialysate regeneration [15]. Recent work (Figure 2.1) had developed an efficient photooxidation of urea reactor (POUR) based on hydrothermally grown TiO_2 nanowires on conductive FTO (Fluorine-doped Tin Oxide) glass, UV LEDs, and catalytic gas diffusion barriers (Pt-coated carbonpaper). Photodecomposition rates were sufficient to remove daily production of urea at 15 g/day with practical device size and power requirements. [16,17] The primary method to improve performance was to use highly conductive single crystal TiO_2 nanowires to separate electron-hole pairs with 0.5V applied bias [16,18] as well as a facile supply of O_2 at the air permeable cathode. Though promising, the urea photodecomposition performance of the POUR panel decreased by over 50% with repetitive 24hr runs. Reported here is the observation of Ti-C bond formation associated with performance decay. Through oxidation cycles, this could be removed and regenerate TiO_2 photocatalytic activity over 52 hours at target therapeutic urea removal rates of 0.34mg/hr cm^2.

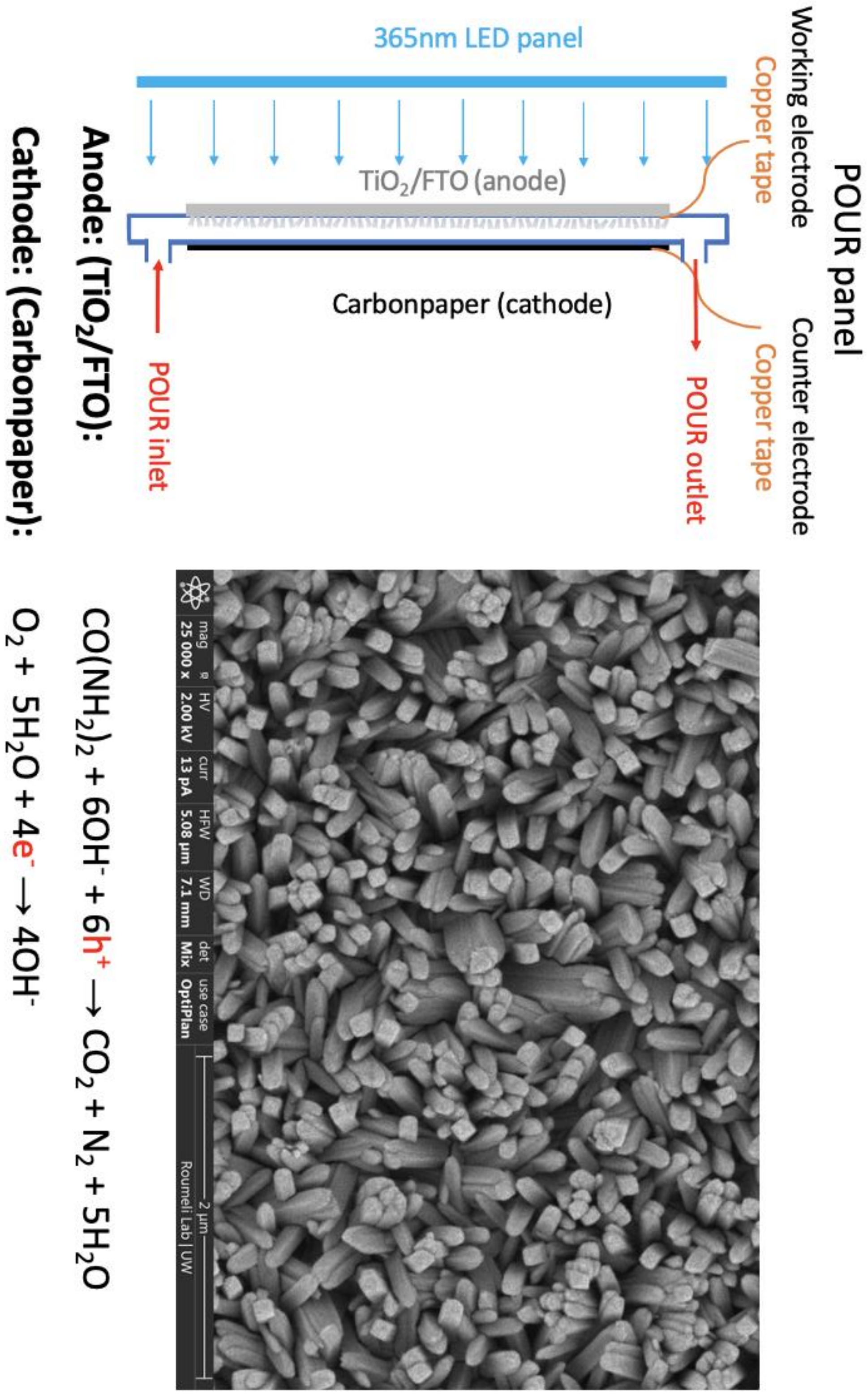

Figure 2.1. The schematic of assembled POUR panel for urea photodecomposition and SEM image of TiO_2 nanowires hydrothermally grown on the conductive FTO glass.

2.2 EXPERIMENTAL METHODS

2.2.1 *Materials*

Fluorine-doped tin oxide (FTO) on glass microscope slides (2.5cm x 7.6cm) were purchased from MTI Corp. (TEC 7). The carbonpaper, with 4 mg/cm^2 amount of Pt-coated, was from FuelCellStore.com. Titanium (IV) isoproproxide (TTIP), 37% concentrated hydrochloric acid (HCl) and isopropanol (IPA) were from Sigma-Aldrich. Invitrogen urea nitrogen (BUN) colorimetric detection kit was purchased from ThermoFisher Scientific.

2.2.2 *TiO_2 Nanowire Synthesis*

6 M HCl solution was prepared by mixing 250mL 37% HCL with 250mL deionized water. 12mL of TTIP was added followed by 30min stirring. FTO glasses were cleaned by acetone and IPA with 5min sonication, respectively. After the cleaning process, the FTO glasses were air dried by compressed air. A microwave hydrothermal synthesis system (MARS^{TM} 6, Parallel & Scale-Up Microwave Synthesizer) bought from CEM Corporation was used for the TiO_2/FTO glass synthesis. Two FTO slides were placed in each vessel, with FTO growth surfaces facing away from each other and 60mL of TTIP-HCl solution added. The ramping time from room temperature (20℃) to 150 ℃ is 20 minutes, and the temperature was kept at 150 ℃ for 50 minutes. The TiO_2/FTO glass subtracts were then annealed in air at 550 ℃ for 3hr.

2.2.3 *POUR Panel Assembly and POUR Test*

POUR Panel Assembly. The frame of the POUR panel is Poly(methyl methacrylate), cut by laser cutter to hold a single annealed TiO_2/FTO glass substrate. This acts as the photoanode and was assembled into the POUR panel according to the schematic shown in Figure 2.1 (Left). Gas permeable carbonpaper, loaded with 4mg/cm^2 Pt black, was used as the counter cathode on the back side of the POUR panel. Copper tape was used to make electric connections on electrodes, and by applying additional silver paste (purchased from TedPella) the electric conductivity was improved. The panel was sealed by the ultra-clear medical-grade epoxy purchased from Ellsworth Adhesives, followed by an overnight epoxy curing process at room temperature. UV LED strips with 365 nm peak wavelength (realUV™ LED Strip Lights) were cut and connected to make an LED panel array with 25 mW/cm^2 power intensity.

POUR test. The setup for the POUR test with the solution circulation loop is shown in Figure 2.2, with the automatic Arduino sample collection and purging system. 200mL of 10mM urea with 0.15M NaCl solution was prepared and circulated in the POUR loop with a flow rate of 1.8 ml/min. Equivalent amount of urea (15g/day) is gradually infused via syringe pump into the urea solution beaker to mimic the amount of urea generated in the human body every day. A constant 0.5V operation voltage was applied by the Metrohm Autolab PGSTAT204 potentiostat. TiO_2 is the working electrode, and the carbon paper/Pt is the combined counter and reference electrode. The photocurrent vs time curve was recorded during the POUR experiment at a 5s time interval. The sampling and air purge process is automatically controlled by the Arduino system with the 3-way valves: A-sampling, B-inlet diversion loop, C-air purge outlet, D-air purge inlet. 1mL sample solution was collected every 4hr from the circulation loop and was frozen under -4℃ for further analysis. Purging treatment during the POUR experiment was controlled by the Arduino system with desired length of purging period and frequency. High positive bias pulse treatment was conducted by programming the NOVA software, which connected the potentiostat. For the single pass POUR experiment, there was no solution circulation, and the sample solutions were collected directly from the outlet of the POUR panel, followed by -4℃ freezing.

2.2.4 *Characterizations*

Urea Concentration Determination. Urea nitrogen (BUN) colorimetric detection kit (Invitrogen) was used to determine the urea concentration of the sample solutions collected from the POUR experiment. Standard solutions and assays were prepared according to the standard operation procedure (SOP) using the provided 96-well plate. The plate was then read at 450 nm by SpectraMax i3x from Molecular Devices with absorption mode. The standard curve was generated by curve-fitting software with a four-parameter algorithm.

Scanning Electron Microscope. The scanning electron microscopy (SEM) images of the TiO_2/FTO glasses were taken using the FEI XL830 dual beam FIB/SEM at 2 kV.

X-ray photoelectron spectroscopy. XPS spectra of TiO_2 samples were taken on a Surface Science Instruments S-Probe spectrometer. This instrument has a monochromatized Al x-ray source and a low energy electron flood gun for charge neutralization. X-ray spot size for these acquisitions was 800 x 800 μm. Pass energy for survey spectra (composition) was 150 eV. The pass energy for high-resolution spectra was 50 eV. For the high-resolution C ls spectra all binding energies were referenced to the C ls C-C bonds at 285.0 eV. A detail scan was run for N 1s to improve quantification. Quantification of survey spectra was done using the Service Physics Hawk Analysis 7 program (Service Physics, Bend OR). The peak fitting of high-resolution spectra was done in CasaXPS. For peak fitting, a Shirley background was used.

Total Free Chlorine Species Concentration Determination. DPD Free Chlorine Reagent Powder Pillows purchased from HACH were used to determine the total free chlorine concentration in the sample solutions collected from the single pass POUR experiment, according to the SOP provided. Standard solution was provided by HACH, and a serial dilution of the standard solution was made in the lab to get the calibration curve for the concentration measurement. The measurement range for total free chlorine species in the solution ranges from 0.1 to 8.0 mg/L.

Ammonia (NH_3) and Ammonium (NH_4^+) Concentration Determination. The High-Performance Ammonia Ion Selective Electrode purchased from Thermo Scientific was used to measure the total amount of gas-phase NH_3 and dissolved NH_4^+ concentration in sample solutions collected from the single pass POUR experiment, according to the SOP provided. Six standard NH_4Cl solutions were prepared by a serial dilution (ranging from 0.1M to 1μM) of the 0.1M NH_4Cl standard from Thermo Scientific. 0.2mL of pH-adjusting ionic strength adjuster (ISA) solution was added into 10mL standard/sample solutions before each measurement. The measurement range for the total amount of gas-phase NH_3 and dissolved NH_4^+ concentration in the solution ranges from 10^{-3} to 10^3 mg/L. The amount of NH_3 and NH_4^+ in the fresh-prepared 10mM urea 0.15M NaCl solution was also measured, as background reference.

Cyclic Voltammetry Analysis. Cyclic Voltammetry (CV) scans were measured by the Metrohm Autolab PGSTAT204 in potentiostat mode, ranging from -1.0V to 1.9V, with scanning rate of 50mV/s. Ag/AgCl was used as the reference electrode.

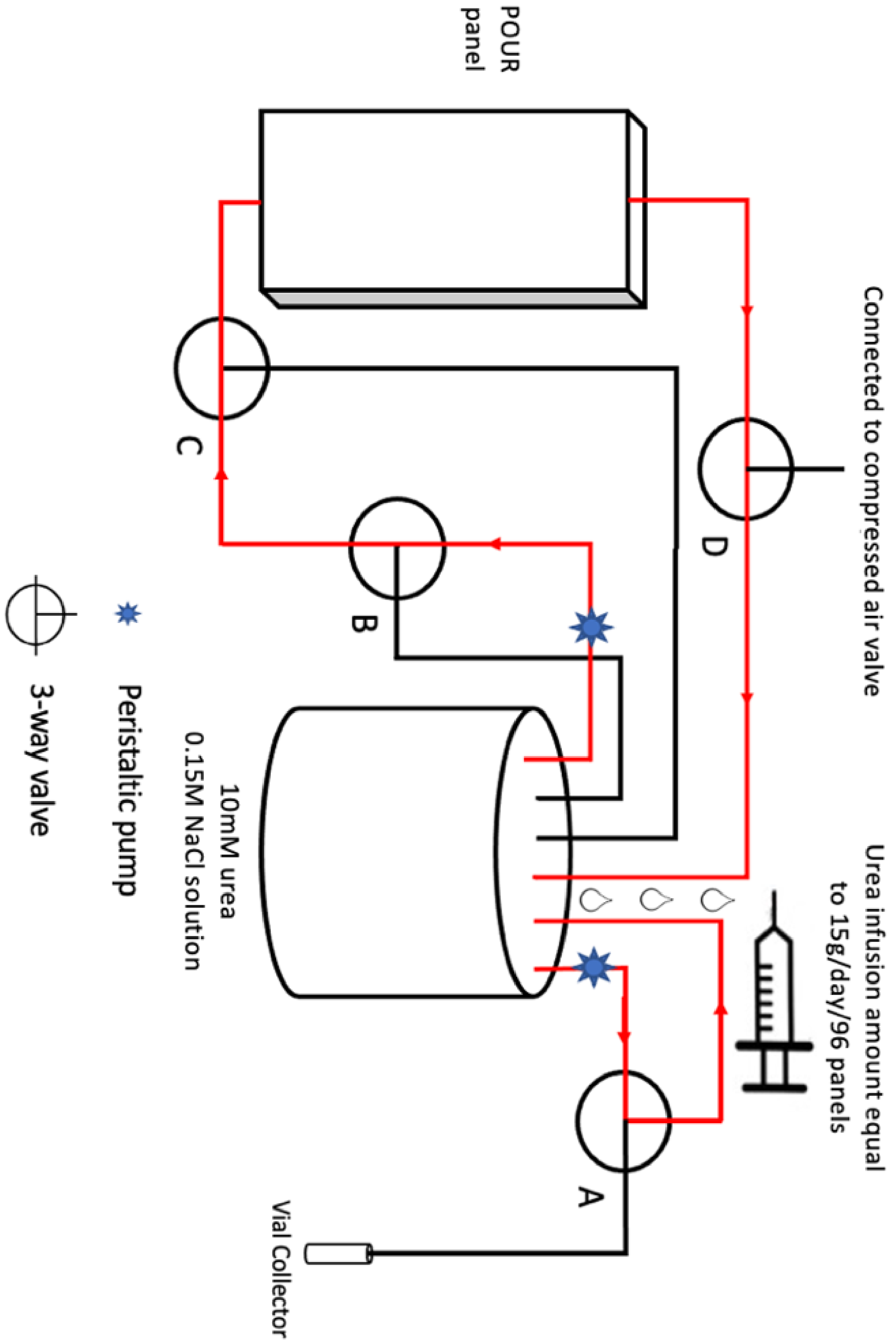

Figure 2.2. Schematic diagram of the setup for POUR experiment with automatic Arduino sample collection and purging system.

An equivalent amount of urea (15g/day) is gradually infused into the urea solution beaker to mimic the amount of urea generated in the human body every day. The sampling and air purge process is automatically controlled by the Arduino system and 3-way valves A-sampling, B- inlet diversion loop, C-air purge outlet, D-air purge inlet. The red loop indicates the solution flow during the normal POUR operation. Sample collection: switch valve A; Purging treatment: switch valve B, C and D.

2.3 RESULTS AND DISCUSSION

Figure 2.1 shows the schematic of the assembled POUR panel for urea photodecomposition and the SEM image of the photocatalytic TiO_2 nanowires, hydrothermally grown on the FTO substrate. According to the SEM image of the TiO_2 nanowires, the diameter is around 100nm, and the size of the nanowires is uniform throughout the entire substrate. The photocatalytic reactions on anode and cathode are listed in Figure 2.1. On the photoanode side (TiO_2/FTO), photo-excited h^+ reacts with urea in the solution, and the e^- would be driven to the cathode side under external applied voltage, avoiding charge recombination loss [5,15]. On the cathode, e^- reacts with H_2O and O_2, which is freely diffused through the gas permeable carbonpaper. For full scale demonstration eight ~10cm x 23cm panels were used and is a practical limit to what can fit in a portable backpack. This area ($1800cm^2$) and 15g/day urea decomposition rate give a target performance of 0.33mg/hr cm^2 for test size device. Higher performance would allow smaller devices.

For an as-prepared POUR panel, the urea photodecomposition rate during 4-24hr is about 0.28 mg/hr cm^2, but after more than 20 runs, it drops to a significantly lower level around 0.12 mg/hr cm^2, shown in Figure 2.3 a) and b). By replacing the used carbonpaper with a new one, we did not observe the restoration of the urea photodecomposition performance, suggesting that the performance-limited component in the POUR panel is the TiO_2. We also observed that between POUR experiments, the panel is exposed to air purging for at least 24hr, and a high urea photodecomposition rate was measured during the first 4hr of operation. We thus hypothesized the periodic air purging would continuously restore TiO_2 during the POUR panel operation. Figure 2.3 c) and d) show periodic air purging as the regeneration treatment method to meet the 0.33 mg/hr cm^2 urea removal target (red dashed line). The black dash line indicates the average urea removal rate of this POUR panel during the 4-24hr as a steady state value for comparison. During the first 4hr, the urea photodecomposition rate is faster but not in steady state.

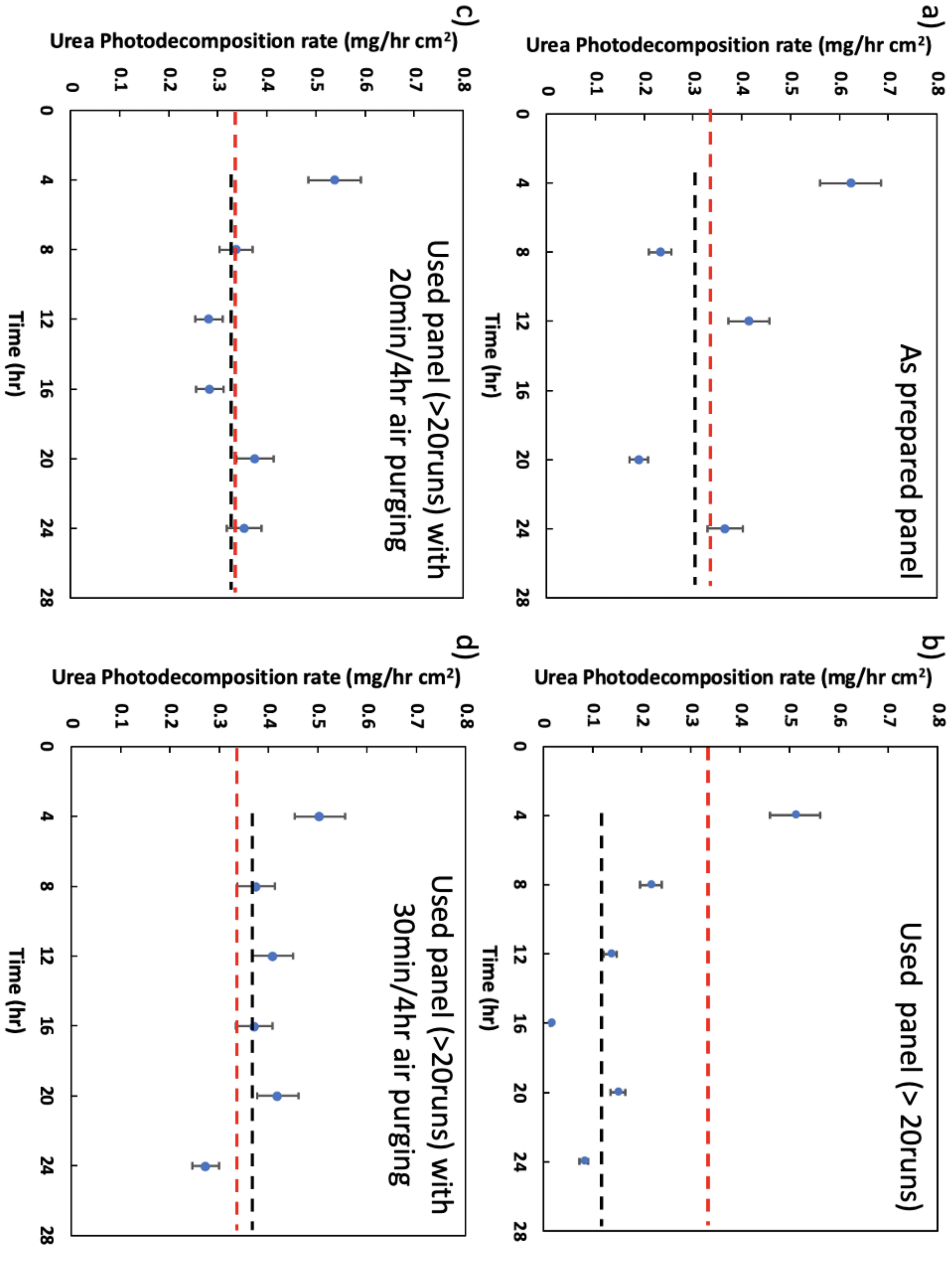

Figure 2.3. A comparison of the urea photodecomposition rate between a) the as-prepared POUR panel and b) the same POUR panel after more than 20 runs (24hr each); with c) 20min/4hr and d) 30min/4hr air purging as the regeneration treatment during the POUR experiments.

The red dashed line indicates the targeted 0.33 mg/hr cm^2 urea removal rate, corresponding to normal human body daily urea production rate (15g/day) and 1800cm^2 device; and the black dash line indicates the average urea removal rate of the POUR panels during the 4-24hr under different experimental conditions.

With 20min air purge per 4hr run time, the urea photodecomposition rate during 4-24hr is measured to be 0.33 mg/hr cm^2; with 30min/4hr treatment, the urea decomposition rate during 4-24hr is 0.37 mg/hr cm^2 for the same POUR panel. For this used POUR panel with period air purging during its operation, the urea photodecomposition rate between 4-24hr is even higher (17%-33%) than its as-prepared condition (0.28mg/hr cm^2). Meanwhile, this periodic air purging treatment suggests that oxidation may be the main mechanism of the TiO_2 regeneration process.

Table 2.1 also illustrated the urea photodecomposition rate during 4-24hr for the same 1x1 POUR panel with different purging treatment time periods and purging species. A longer air purging time improves TiO_2 regeneration but would reduce percent duty cycle time for operation. Overnight air purging gives highest TiO_2's urea photodecomposition rate within the first 4hr but is not maintained after that period. Pure O_2 shows a higher regeneration compared to air (20% O_2) at the same cycle time, suggesting that O_2 is the active species during the regeneration process. Oxidation by H_2O_2 also showed regeneration of TiO_2 performance but over time would oxidize the carbon paper, reducing overall performance.

Table 2.1. The urea photodecomposition rate during 4-24hr for the same POUR panel with different gas purging treatments.

The normal purging treatment used air (20% O_2) as purging species. With *marked, pure O_2 was used.

Purging time (min/4hr)	0	5	10	10*	20	20*	30
Urea photo-decomposition rate (4-24hr) (mg/hr cm^2)	0.12	0.20	0.17	0.30	0.33	0.35	0.37

Since oxidation is qualitatively seen to restore TiO_2 performance, X-ray photoelectron spectroscopy (XPS) analysis was performed to find any surface reduction products on the TiO_2, and the surface chemistry of TiO_2 was also characterized by XPS, shown in Table 2.2. No Ti-C bonding was found on fresh as-synthesized TiO_2 surface but appeared on the TiO_2 sample after 24hr test (without any treatment). This indicates that carbon compounds formed on the TiO_2 surface, poisoning photo-electrocatalytic sites. After air purging overnight, Ti-C bonding disappeared, which agrees with the observation that overnight air purging can significantly restore the TiO_2's urea photodecomposition rate during the first 4hr of the 24hr test. Ti-C is a relatively strong covalent bond at 423 kJ/mol would thus has a kinetic barrier to forming the more stable Ti-O bond of 666 kJ/mole [19].

Table 2.2. The XPS results for TiO_2 surface analysis before and after 24hr POUR experiment without regeneration treatments and with overnight air treatment.

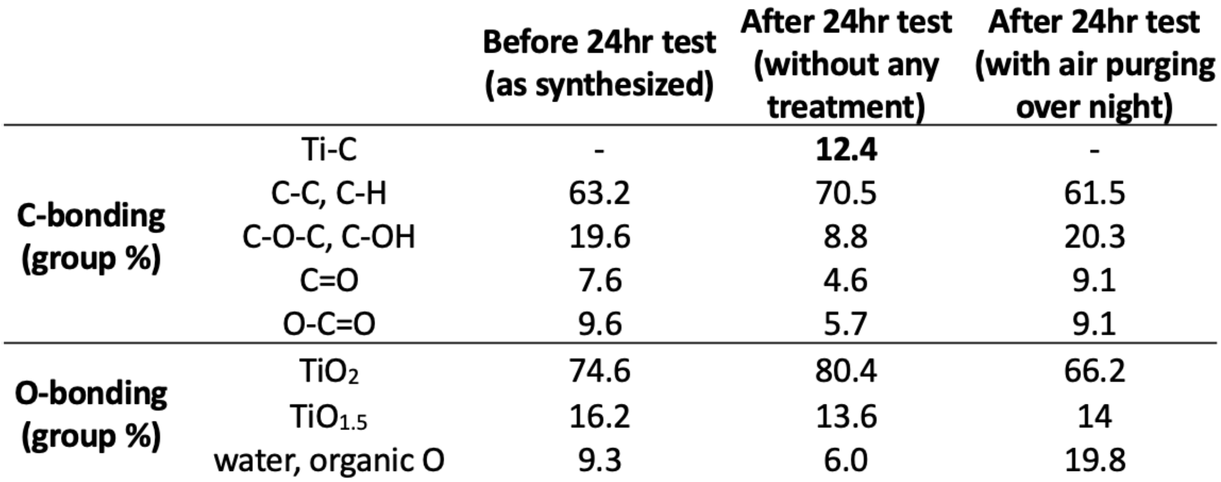

		Before 24hr test (as synthesized)	**After 24hr test (without any treatment)**	**After 24hr test (with air purging over night)**
C-bonding (group %)	Ti-C	-	**12.4**	-
	C-C, C-H	63.2	70.5	61.5
	C-O-C, C-OH	19.6	8.8	20.3
	C=O	7.6	4.6	9.1
	O-C=O	9.6	5.7	9.1
O-bonding (group %)	TiO_2	74.6	80.4	66.2
	$TiO_{1.5}$	16.2	13.6	14
	water, organic O	9.3	6.0	19.8

Since the performance impaired POUR panel has a significant amount of Ti-C bonding on TiO_2 surface, it is expected to be oxidized by species, such as O_2 and H_2O_2, or a high positive bias near the splitting of water (ranging from 1.0 to 1.5V). Voltages higher than 1.5V have excessive water splitting and non-selectively oxidize Cl^- to oxochloro species. Figure 2.4 and Table 2.3 illustrate the urea photodecomposition rate of this used POUR panel with different applied bias pulse treatments. The shorter time is that of the high voltage pulse while the longer time is for the operational voltage at 0.5V. Both 1.35 and 1.5V are considered as optimal voltages for the applied bias pulse treatment for the TiO_2 regeneration. Comparing between the 5min/hr and 5s/min 1.5V applied bias pulse treatments, both offer similar performance at the same 92% duty cycle. The shorter pulses offer an advantage of a more uniform output stream to the dialyzer.

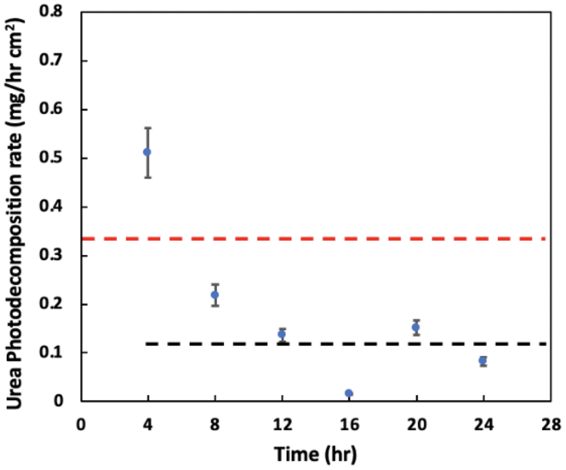

Without treatment (>20runs)

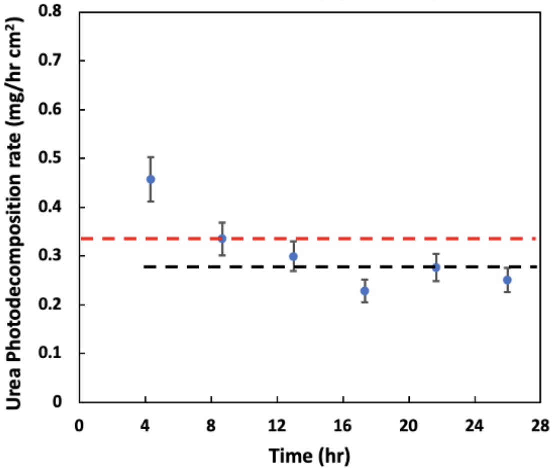

5min/hr 1.0V applied pulse

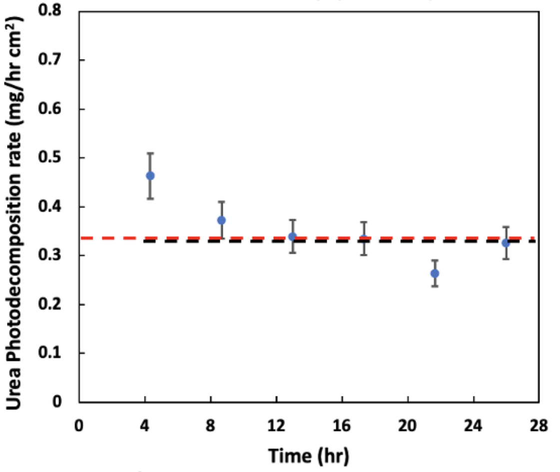

5min/hr 1.5V applied pulse

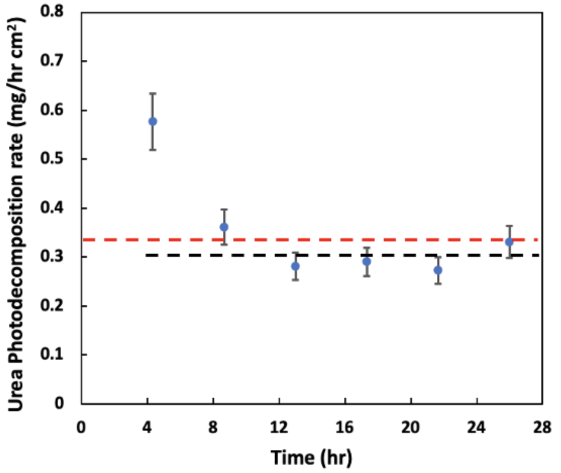

5min/hr 1.2V applied pulse

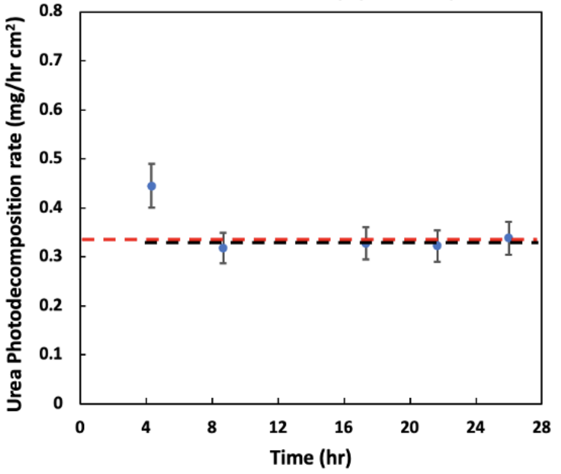

5min/hr 1.35V applied pulse

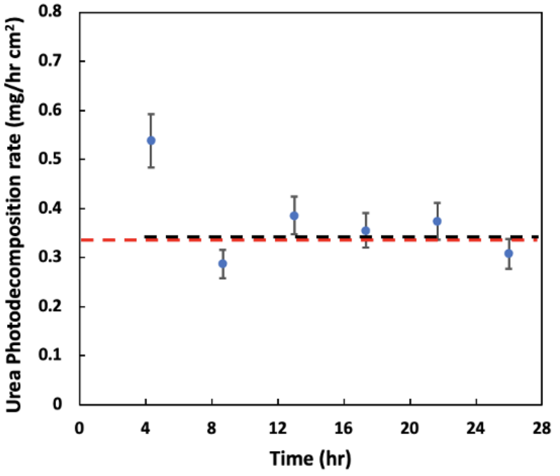

5s/min 1.5V applied pulse

Figure 2.4. Effect of different applied bias pulse treatments on the TiO_2 regeneration process in 24hr POUR experiments.

Shorter time is the duration of indicated voltage pulse while operation bias was 0.5V for the longer time.

Table 2.3. Effect of different applied bias pulse treatments on the TiO_2 regeneration process in 24hr POUR experiment.

A constant 0.5V voltage was applied during the 24hr POUR operation. The frequency of the voltage pulse treatment is 5min/hr. With *marked, the frequency of voltage pulse is 5s/min.

Voltage Pulse (V)	**-**	**1.0**	**1.2**	**1.35**	**1.5**	**1.5***
Urea photo-decomposition rate (4-24hr) (mg/hr cm^2)	0.12	0.28	0.31	0.33	0.33	0.34

To study the effect of this applied bias pulse treatment in a long-term experiment, an as-prepared POUR panel was operated for 52 hours with 5min/hr 1.5V applied bias pulse treatment, shown in Figure 2.5. We still observed a high urea photodecomposition rate within the first 4hr, and then the urea photodecomposition rate keeps stable at around 0.34mg/hr cm^2 for the rest of the 48hr, suggesting that the applied bias pulse is a promising strategy to help maintain the urea photodecomposition performance on TiO_2.

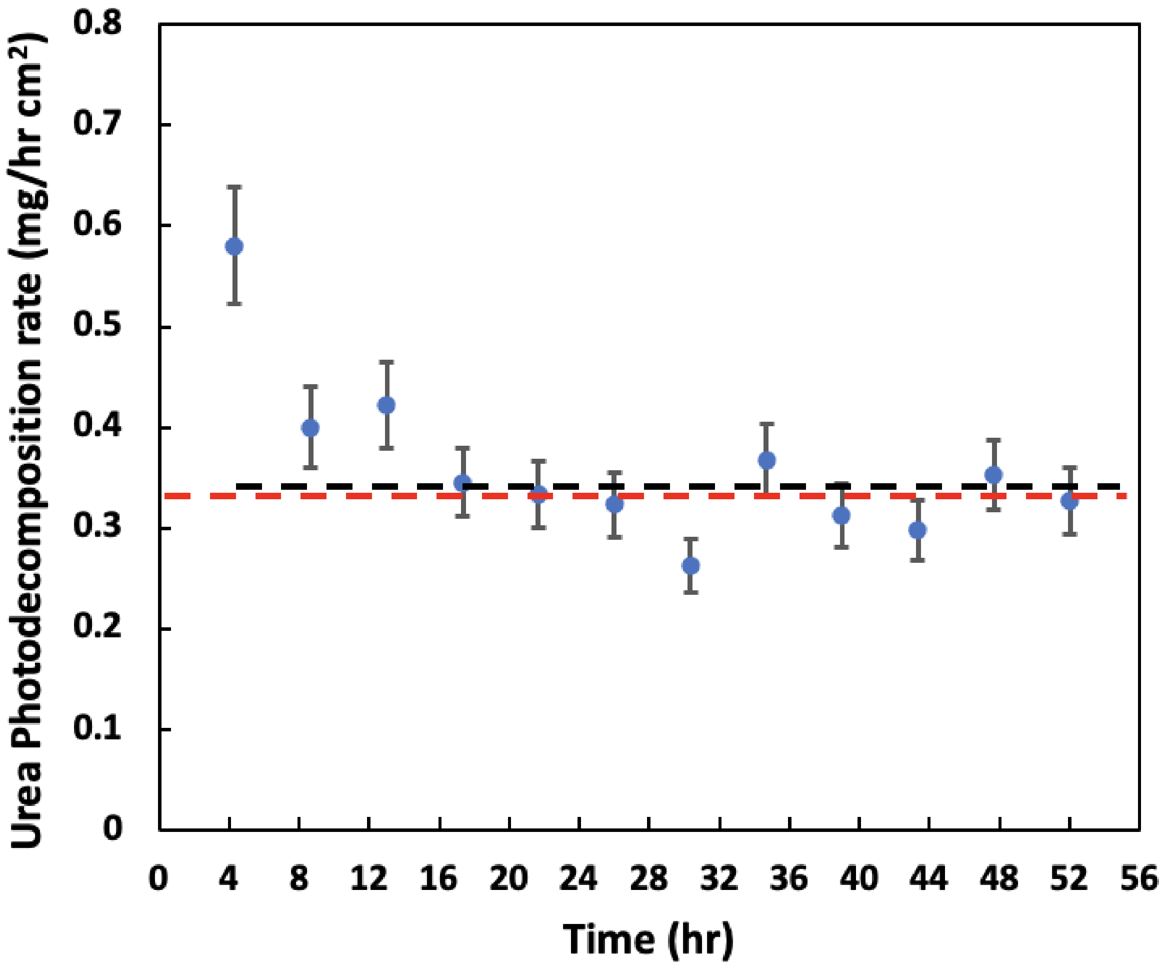

Figure 2.5. Urea photodecomposition rate for a 52hr POUR experiment on an as-prepared POUR panel with a constant 0.5V operation voltage and a 5min/hr 1.5V applied bias pulse treatment.

A major concern on employing the high voltage applied bias pulse as TiO_2 regeneration is to have side reactions with Cl^- to form Cl_2 and related oxochlorines or the incomplete urea oxidation forming ammonia. The TiO_2 urea photooxidation system is remarkably selective (90%) to urea (at ~10mM) compared to the dialysate (150mM NaCl solution). It would be expected that applying bias would reduce the TiO_2 selectivity of photooxidizing urea, but the opposite is seen in Figure 2.6, where with 1.5V voltage pulse treated, TiO_2 produces less chlorine species and ammonia. We measured the free chlorine and ammonium concentration from the outlet of the POUR panel during 24hr experiments in a single pass (non-recirculating mode). The formation rate of free chlorine and ammonia, as listed in Table 2.4, 5min/hr 1.5V applied bias pulse treatment gave the lowest free chlorine species and ammonia formation rates, compared to no treatment and air purge treatment. Interestingly, the free chlorine and ammonia formation rates with no treatment and with 30min/4hr air purging treatment are very similar. For running POUR experiment at constant 1.5V, we do see a significant amount of ammonia formation (~6x) and about 2x the chlorine formation and this agrees with less urea selectivity and incomplete urea oxidation under strong applied bias. However, the absolute amounts of ammonia formed are about 85 times less than urea being photodecomposed (6.65 μg/hr cm^2 ammonia formed vs. 0.56 mg/hr cm^2 urea decomposed) or 24 times less at a molar level. The chlorine levels are 1000x less. Thus, the urea selectivity remains extremely high even at elevated bias on the TiO_2 surface.

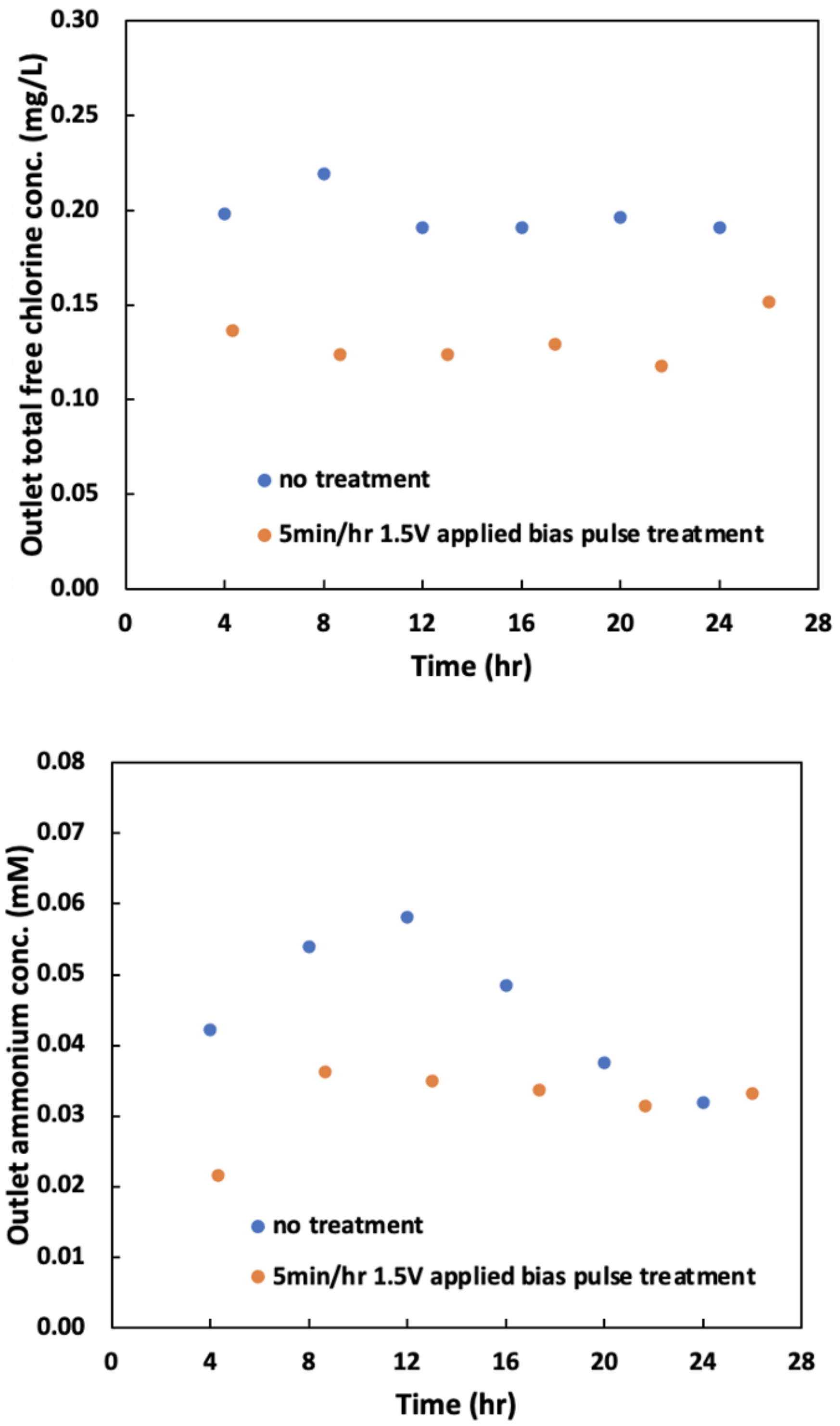

Figure 2.6. The measured a) free chlorine and b) ammonia concentration from the outlet of POUR panel during 24hr experiment with no treatment; 5min/hr 1.5V applied bias pulse treatment.

Table 2.4. The experimentally measured photocurrent, urea photodecomposition rate, free chlorine species and ammonia formation rates from the same POUR panel under different operation conditions, with single-pass setup in 24hr experiments.

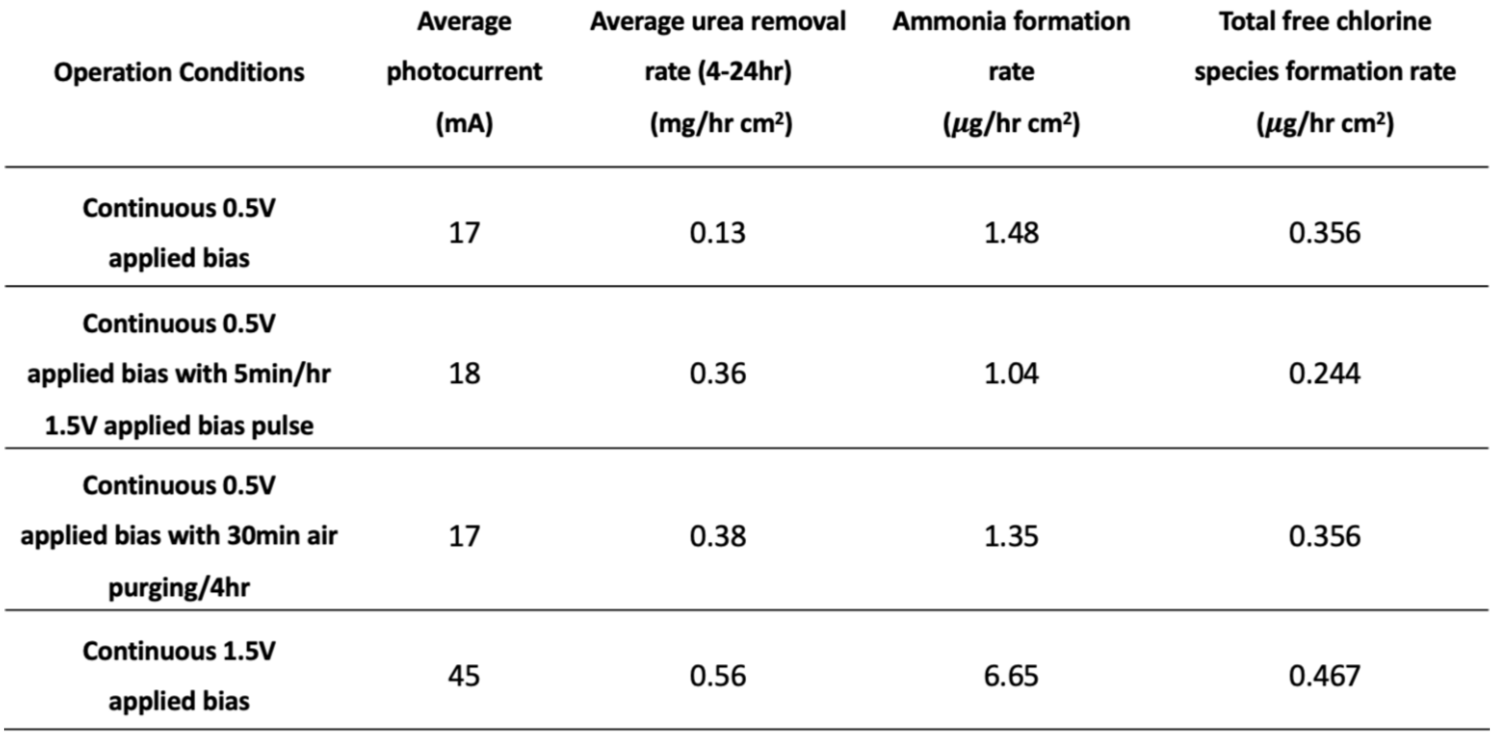

Operation Conditions	Average photocurrent (mA)	Average urea removal rate (4-24hr) (mg/hr cm^2)	Ammonia formation rate (μg/hr cm^2)	Total free chlorine species formation rate (μg/hr cm^2)
Continuous 0.5V applied bias	17	0.13	1.48	0.356
Continuous 0.5V applied bias with 5min/hr 1.5V applied bias pulse	18	0.36	1.04	0.244
Continuous 0.5V applied bias with 30min air purging/4hr	17	0.38	1.35	0.356
Continuous 1.5V applied bias	45	0.56	6.65	0.467

Notably, the photocurrent is tripled when we tripled the continuous operation voltage from 0.5V to 1.5V, suggesting the importance of separating the photon excited electrons/holes to the FTO electrode and TiO_2, respectively. However, even though we observed a tripled the photocurrent by increasing the applied bias from 0.5V to 1.5V, the urea photodecomposition rate is not tripled. Only ~50% of the photocurrent goes to urea oxidation reaction when we applied a constant 1.5V applied while with the constant applied bias of 0.5V, the selectivity of photocurrent toward urea photodecomposition is ~80% [5]. However, we did not see a significantly increased amount of chlorine species formed in the outlet from the POUR panel, hence chloride oxidation is not the main byproduct during the constant 1.5V high voltage operation.

Mechanistically, it is insightful to look at the cyclic voltammetry (CV) measured under dark condition and under UV light (normal POUR panel operation condition) to compare TiO_2 behavior as an electrochemical electrode versus a photocatalytic electrode. As shown in Figure 2.7 a), under UV light the photocurrent measured is about two orders of magnitude higher than that under ambient light, showing that the photon excited electron/hole pairs are the dominant species in the TiO_2 photocatalytic reactions. Thus, the galvanic decomposition of urea by applied bias is negligible. Higher bias separates electron-hole pairs, preventing recombination and substantially increasing photocurrent. The measured photocurrent in the CVs in Figure 2.7 a) is in agreement with the photocurrent measured in the 24hr experiment with constant 0.5V and 1.5V, as listed in Table 2.4. However, when further increase the applied voltage beyond 1.9V, the photocurrent reaches a plateau indicating that all available electron/hole pairs have been separated with minimal recombination loss. Figure 2.7 b) shows the differences between dark C-V scans for the POUR panel without and with 10mM urea in the 0.15M NaCl solution. The water splitting peak starts to form when the applied voltage is above 1.5V. When the urea is present in the solution, the height of water splitting peak is lower by 73%, suggesting that the urea has affinity to the TiO_2 surface suppressing the water splitting reaction.

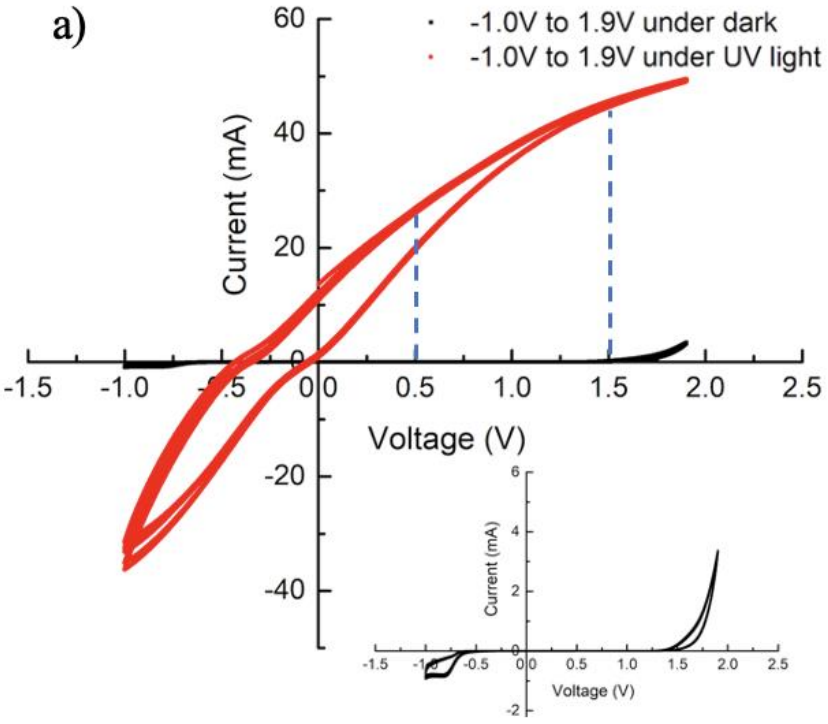

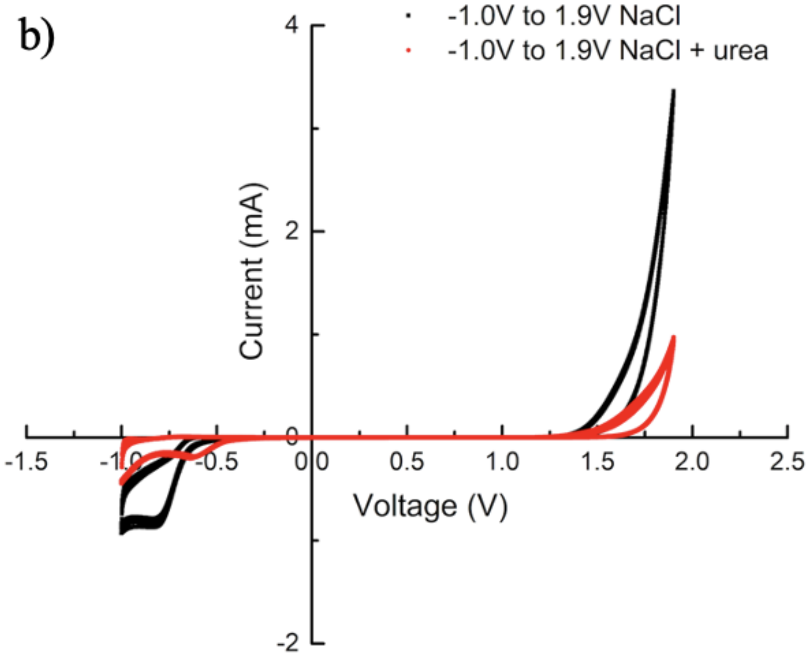

Figure 2.7. The C-V scans of the POUR panel with a) 0.15M NaCl + 10mM urea solution under dark condition vs. under UV light irradiation; b) 0.15M NaCl solution and 0.15M NaCl + 10mM urea solution under dark condition.

Blue dash lines are the photocurrents when the applied voltages are 0.5V and 1.5V. The inset figure is the zoomed-in CV curve measured under dark condition. The electrode area is 16.8 cm^2.

2.4 CONCLUSION

TiO_2 based selective photo-oxidation of urea is a promising route to regenerate kidney HD dialysate to enable portable and continuous treatments. However, a 50% reduction in performance after 12 hours of use posed a serious challenge due to Ti-C bond formation as seen by XPS. This carbon bond could be oxidized to Ti-O via air exposure, chemical oxidation and by a high applied bias in aqueous solution, with the latter being easily implemented in practice. The voltage pulses did not produce a significant increase in ammonia nor free chlorine species. Higher applied biases dramatically increased photocurrent by separating e^-/h^+ pairs to cathode circuit and anode surface. With an optimized high voltage bias pulse (5min/hr at 1.5V) as the TiO_2 regeneration treatment, the equivalent urea removal rate of the POUR panel could achieve the 15g/day target for a wearable dialysis device in a 52hr test. This regeneration approach will be critical to enable a photocatalytic route to dialysate regeneration and its incorporation into portable continuously operating devices.

2.5 REFERENCE

[1] United States Renal Data System (USRDS). 2019 Annual Data Report; USRDS: Minneapolis, MN, USA, 2019.

[2] Himmelfarb, Jonathan, and Buddy Ratner. "Wearable artificial kidney: problems, progress and prospects." Nature Reviews Nephrology 16.10 (2020): 558-559

[3] Roberts, M. "The regenerative dialysis (REDY) sorbent system." Nephrology 4.4 (1998): 275-278.

[4] Agar, John Wm. "Understanding sorbent dialysis systems." Nephrology 15.4 (2010): 406-411.

[5] Raja, Rasib M., Mark S. Kramer, and Jerry L. Rosenbaum. "Recirculation peritoneal dialysis with sorbent Redy cartridge." Nephron 16.2 (1976): 134-142.

[6] Urbańczyk, Ewelina, Maciej Sowa, and Wojciech Simka. "Urea removal from aqueous solutions—a review." Journal of Applied Electrochemistry 46.10 (2016): 1011-1029.

[7] Fujishima, Akira, and Kenichi Honda. "Electrochemical photolysis of water at a semiconductor electrode." nature 238.5358 (1972): 37-38.

[8] Thompson, Tracy L., and John T. Yates. "TiO_2-based photocatalysis: surface defects, oxygen and charge transfer." Topics in Catalysis 35.3 (2005): 197-210.

[9] Lee, Seul-Yi, and Soo-Jin Park. "TiO_2 photocatalyst for water treatment applications." Journal of Industrial and Engineering Chemistry 19.6 (2013): 1761-1769.

[10] Fujishima, Akira, Xintong Zhang, and Donald A. Tryk. "TiO_2 photocatalysis and related surface phenomena." Surface science reports 63.12 (2008): 515-582.

[11] Fujishima, Akira, Tata N. Rao, and Donald A. Tryk. "Titanium dioxide photocatalysis." Journal of photochemistry and photobiology C: Photochemistry reviews 1.1 (2000): 1-21.

[12] Konstantinou, Ioannis K., and Triantafyllos A. Albanis. "TiO_2-assisted photocatalytic degradation of azo dyes in aqueous solution: kinetic and mechanistic investigations: a review." Applied Catalysis B: Environmental 49.1 (2004): 1-14.

[13] Schneider, Jenny, et al. "Understanding TiO_2 photocatalysis: mechanisms and materials." Chemical reviews 114.19 (2014): 9919-9986.

[14] Ku, Young, Yu-Chun Lee, and Wen-Yu Wang. "Photocatalytic decomposition of 2-chlorophenol in aqueous solution by UV/TiO_2 process with applied external bias voltage." Journal of hazardous materials 138.2 (2006): 350-356.

[15] Kaneko, Masao, et al. "Biophotochemical cell (BPCC) to photodecompose biomass and bio-related compounds by UV irradiation with simultaneous electrical power generation." Journal of Photochemistry and Photobiology A: Chemistry 205.2-3 (2009): 168-172.

[16] Shao, Guozheng, Yushi Zang, and Bruce J. Hinds. "TiO2 nanowires-based system for urea photodecomposition and dialysate regeneration." ACS Applied Nano Materials 2.10 (2019): 6116-6123.

[17] Shao, Guozheng, et al. "Dialysate Regeneration with Urea Selective Membrane Coupled to Photoelectrochemical Oxidation System." Advanced Materials Interfaces 9.13 (2022): 2102308.

[18] Ray, Nathan J., and Eduard G. Karpov. "A Voltage Bias Effect on Catalytic Activity of Electrically Continuous Pt/TiO2 Nanocomposites." Advanced Materials Interfaces 5.13 (2018): 1800089

[19] Luo, Yu-Ran. Comprehensive handbook of chemical bond energies. CRC press, 2007.

Chapter 3. INVESTIGATION OF THE PHOTODECOMPOSITION PATHWAY FOR UREA INTO N_2 AT TIO_2 SURFACE FOR PORTABLE KIDNEY DIALYSIS

Adapted from Hao Tang, Mingyuan Zhang, Guozheng Shao, and Bruce J. Hinds. "Investigation of the Photodecomposition Pathway for Urea into N_2 at TiO_2 surface in Portable Kidney Dialysis." Manuscript in preparation.

3.1 BACKGROUND

In the field of healthcare, wearable dialysis devices have gained significant attention as a promising way to enhance the quality of life for patients suffering from end-stage renal diseases (ESRD). These devices aim to provide continuous and personalized dialysis treatment, reducing the need for large-scale dialysis centers and offering greater mobility to the patients. Current dialysis treatments use about 120 liters of dialysate, precluding the ability to make portable systems unless small volumes of dialysate can be cleaned and regenerated. A major challenge in wearable dialysis systems is the effective removal of urea (a major waste product from protein metabolism) and many other non-uremic toxins to regenerate cleaned dialysate. Different types of approaches have been studied to regenerate the spent dialysate, including enzyme/sorbent system[1-3], electrochemical[4-6] and photochemical decomposition methods. The enzyme/sorbent system produces toxic ammonia that must be ion exchanged in sorbent while electrochemical systems produce nitrates and other oxidative species. Titanium dioxide (TiO_2), a widely studied photocatalyst, has exhibited exceptional photocatalytic activity due to its unique properties and low cost. In recent years, researchers have explored various applications of TiO_2 in environmental remediation, energy production, and healthcare.[7-12] TiO_2 photochemistry had been employed to decompose urea into safe N_2 and CO_2 gas for agricultural waste water treatment but energy efficiency and size were several orders of magnitude away from application in dialysate regeneration. From our earlier studies, we have already proven the concept of utilizing TiO_2 as a photocatalyst to photodecompose urea from spent dialysate in a wearable dialysis device, with a high quantum efficiency (QE) up to 30% and an excellent selectivity (up to 76% of the photocurrent) toward urea photodecomposition.[13-15] Large gains in performance were made by using 1) TiO_2 nanowires with direct connection to FTO collector to separate electron (e^-) hole (h^+) pairs 2) the air permeable Pt/carbonpaper cathode and 3) the use of energy efficient UV-LEDs. The main products formed from urea photo-oxidation reaction in our designed TiO_2 flow reactor system are N_2 and CO_2, as shown below.[14, 15]

Anode: (TiO_2/FTO): $CO(NH_2)_2 + H_2O + 6e^- + 6h^+ \rightarrow CO_2 + N_2 + 6H^+ + 6e^-_{circuit}$

Cathode: (Pt/Carbonpaper): $\frac{3}{2}O_2 + 3H_2O + 6e^-_{circuit} \rightarrow 6OH^-$

Overall: $CO(NH_2)_2 + \frac{3}{2}O_2 \rightarrow CO_2 + N_2 + 2H_2O$

However, through electrochemical decomposition by Pt[4, 5, 16] or boron-doped diamond (BDD)[4, 6] electrodes, urea can be decomposed into toxic compounds such as NH_3/NH_4^+ or NO_3^-, shown below.

NH_3/NH_4^+ as product: $CO(NH_2)_2 + H_2O \rightarrow CO_2 + 3NH_3$

NO_3^- as product: $CO(NH_2)_2 + 4O_2 \rightarrow CO_2 + 2NO_3^- + 2H^+ + H_2O$

Herein, we aim to further investigate the photocatalytic reaction mechanism at the TiO_2 surface and to understand the factors that influence the efficiency and selectivity of the urea photodecomposition reaction into physiologically safe N_2 and CO_2. The investigations on flow-rate and urea-concentration dependencies demonstrate that the urea photo-oxidation reaction is not mass transport limited but surface reaction limited, emphasizing the importance of the TiO_2 surface reaction for the performance optimization. Through experimental studies, we have discovered the key intermediates in the urea photocatalytic reaction, chlorine ions (Cl^-) reacting with holes (h^+) to form Cl-TiO_2 surface bound species that can form chlorine radicals (Cl·) to react with urea and have safe N_2 and CO_2 byproducts.[17, 18] The use of other anions, SO_4^{2-} and HCO_3^-, gave nitrate byproduct or quenched the urea reaction. To gain deeper insights into the photocatalytic reaction mechanism at TiO_2 surface, we adopt a comprehensive approach that combines experimental study with theoretical DFT modeling[19-21], and this synergistic approach allows us to systematically figure out the interactions between TiO_2 surface, urea molecules and the Cl^-/Cl· intermediates, elucidating the mechanistic pathways involved in the urea photodecomposition reaction at the TiO_2 surface.

3.2 EXPERIMENTAL METHODS

3.2.1 *Materials*

Fluorine-doped tin oxide (FTO) on glass microscope slides (2.5cm x 7.6cm) were purchased from MTI Corp. (TEC 7). The carbonpaper as a counter-electrode, with 4 mg/cm2 amount of Pt-loaded, was purchased from Fuel Cell Store (www.fuelcellstore.com). Titanium (IV) isoproproxide (TTIP), 37% concentrated hydrochloric acid (HCl), ammonium chloride (NH4Cl, ≥99.5%), tert-butanol (anhydrous, ≥99.5%) and nitrobenzene (≥99%) were purchased from Sigma-Aldrich. Invitrogen urea nitrogen (BUN) colorimetric detection kit and the allyl alcohol (≥98%) were purchased from ThermoFisher Scientific.

3.2.2 *Synthesis of TiO_2 Nanowire on FTO Glasses*

The TiO_2 coated FTO glasses were prepared with optimized procedure from our early study. First, a 6 M HCl solution was prepared by mixing 250mL 37% HCl with 250mL deionized water, then 12mL of TTIP was added followed by 30min continuous stirring. Bare FTO glasses were cleaned by acetone and IPA with 5min sonication, respectively. After the cleaning process, FTO glasses were air dried with compressed air. A microwave hydrothermal synthesis system (MARSTM 6, Parallel & Scale-Up Microwave Synthesizer) bought from CEM Corporation was used for the TiO_2/FTO glass synthesis. Two FTO slides were placed in each vessel, with FTO growth surfaces facing away from each other and 60mL of TTIP-HCl solution added. The ramping time from room temperature (20℃) to 130 ℃ is 20 minutes, and the temperature was kept at 130 ℃ for 40 minutes. The TiO_2/FTO glass subtracts were then annealed in air at 550 ℃ for 3 hours.

3.2.3 *Photo-Oxidation of Urea Reactor (POUR) Panel Assembly and Performance Test*

Photo-Oxidation of Urea Reactor (POUR) Assembly

The frame of the POUR panel is Poly(methyl methacrylate) purchased from McMaster-Carr, cut by laser cutter to hold a single annealed TiO_2/FTO glass substrate. The TiO_2/FTO glass acts as photoanode, and the gas permeable carbonpaper, loaded with 4mg/cm^2 Pt black was used as the counter electrode at the back side of the POUR panel. Copper tapes were used to make electric connections on both electrodes, and additional silver paste (purchased from TedPella) was applied to improve the electric conductivity between electrodes and the copper tapes. Finally, the panel was sealed by the ultra-clear medical-grade epoxy (purchased from Ellsworth Adhesives), followed by an overnight epoxy curing process at room temperature. The dimension of the flow channel in POUR panel is about 0.25cm x 2.1cm x 7.1cm. UV LED strips with 365 nm peak wavelength (from realUV™ LED Strip Lights) were cut and connected to make an LED panel array as UV light irradiation source.

POUR Performance Test

For a standard closed-loop circulation experiment, 200mL of 10mM urea with 0.15M NaCl solution was prepared and circulated in the POUR loop with a flow rate of 0.6 ml/min with the peristaltic pump. 0.15625g/day urea (equivalent amount of 15g/day for 96 single panels) was gradually infused via syringe pump into the urea solution beaker to mimic the amount of urea generated in the human body every day. For the standard single-pass experiment, 10mM urea with 0.15M

NaCl solution was continuously pumped into the POUR loop with a flow rate of 0.6 mL/min by a peristaltic pump, with no urea infusion process. The closed-loop circulation experiment was designed to study the long-term performance of the POUR, while the single-pass experiment was dedicated for investigating how experimental conditions affect the urea photodecomposition performance. TiO_2 is the working electrode, and the carbon paper/Pt is the combined counter and reference electrode. For both these two experiments, a constant 0.5V operation voltage with 5s/min 1.5V voltage pulse was applied by the Metrohm Autolab PGSTAT204 potentiostat. The photocurrent vs time curve was recorded during the POUR experiment at a 5s time interval. For the standard closed-loop circulation experiment, 1mL sample solution was collected every 4hr from the circulation loop and was frozen under -4 ℃ for further analysis; for the standard single-pass experiment, after the POUR run for 4 hours to reach the steady state, solution samples could be directly collected at the outlet of the POUR panel at any desired time point for the analysis. For investigation on the flow-rate dependency on urea photodecomposition rate, 10mM urea with 0.15M NaCl solution was fed under different flow rates in the single-pass setup, with other experimental parameters to be the same as the standard. To investigate the urea-concentration dependency on the urea photodecomposition rate, single-pass experiments were conducted, and the flow rate was changed accordingly to the urea concentration in feeding solution (for example, 0.6mL/min flow rate for 10mM urea solution in standard condition; 0.3mL/min flow rate for 20mM urea solution; 1.2mL/min flow rate for 5mM urea solution). By substituting urea with NH_4Cl, 20mM NH_4Cl with 0.15M NaCl solution was prepared as a feeding solution with the other experimental parameters kept as the same as the standard. In radical scavenger quenching experiments, 10mM urea with 0.15M NaCl solution with different types (tert-butanol, allyl alcohol and nitrobenzene) and different amounts (2.15-215mM) of quenching agents were prepared respectively, and the experiments were conducted under the standard single-pass conditions.

3.2.4 *Characterizations*

Urea Concentration Determination

Urea nitrogen (BUN) colorimetric detection kit (Invitrogen) was used to determine the urea concentration of the sample solutions collected from the POUR experiments. Standard solutions and assays were prepared according to the standard operation procedure (SOP) using the provided 96-well plate. The plate was then read at 450 nm by SpectraMax i3x from Molecular Devices with absorption mode. The standard curve was generated by curve-fitting software with a four-parameter algorithm.

Ammonia (NH_3) and Ammonium (NH_4^+) Concentration Determination

The High-Performance Ammonia Ion Selective Electrode purchased from Thermo Scientific was used to measure the total amount of gas-phase NH_3 and dissolved NH_4^+ concentration in sample solutions collected in the NH_4Cl substitution experiments, according to the SOP provided. Six standard NH_4Cl solutions were prepared by a serial dilution (ranging from 0.1M to 1μM) using the

0.1M NH_4Cl standard from Thermo Scientific. 0.2mL of pH-adjusting ionic strength adjuster (ISA) solution was added into 10mL standard/sample solutions before each measurement. The measurement range for the total amount of gas-phase NH_3 and dissolved NH_4^+ concentration in the solution ranges from 10^{-3} to 10^3 mg/L.

Cyclic Voltammetry (CV) and Electrochemical Impedance Spectroscopy (EIS) Analysis

CV scans under different light intensities were measured for the POUR panel by the Metrohm Autolab PGSTAT204 in potentiostat mode, ranging from 0V to 1.9V, with a scanning rate of 0.3V/s. Light intensity was changed by adding microscope glass substrates or FTO glasses in front of the POUR panel to absorb the UV light. No reference electrode was applied during the CV scans. EIS was conducted for the POUR panel under dark and under normal UV light irradiation using the FRA/impedance feature from Metrohm Autolab PGSTAT204 to study the electronic and ionic processes within the POUR at different applied voltages under either dark or UV light irradiation.

X-ray Photoelectron Spectroscope (XPS)

XPS spectra and surface chemistry analysis of TiO_2 samples were characterized by the Surface Science Instruments S-Probe spectrometer. X-ray spot size for the acquisitions was 800 x 800 μm. Pass energy for survey spectra (composition) was 150 eV. The pass energy for high-resolution spectra was 50 eV. Quantification of survey spectra was done using the Service Physics Hawk Analysis

7 program (Service Physics, Bend OR). Peak fitting of high-resolution spectra was done using CasaXPS. For peak fitting, a Shirley background was used.

3.3 RESULTS AND DISCUSSION

3.3.1 *Photocatalytic decomposition rate of urea and photo-electrochemical study of the TiO_2 system.*

To systematic study on the mechanism of urea photodecomposition reaction on TiO_2 surface, we first studied if the system was mass-transport limited by the flow-rate and urea-concentration effect on urea photocatalytic decomposition rate. Figure 3.1 shows the urea decomposition rate measured under different flow rates, with 10mM urea 0.15M NaCl as the feeding solution. For channel dimensions of ~0.3cm x2.5cm x7.5cm, with standard 0.63mL/min flow rate, the residence time of the solution within the POUR panel in the photodecomposition process is ~9min and output concentration is ~6.5mM. When the flow rate is between 0.24mL/min and 0.89 mL/min, the urea photodecomposition rate is nearly constant, though the output concentration goes from 3.0mM to 8.4mM, indicating that the urea photodecomposition reaction is not mass transport limited but surface reaction limited. However, when the flow rate is at 0.14mL/min, the measured outlet urea concentration is lower than 1mM, which explains the decrease of urea decomposition rate at the low-flow-rate condition and a mass transport limit. A higher flow rate can avoid the depletion of urea in the stream and thus reduce side reactions. Since the POUR panel is designed to regenerate spent dialysate in a wearable dialysis device, the optimized flow rate has been chosen to be 0.6mL/min in order to obtain enough concentration gradient at the hemodialysis part in the dialysis device.

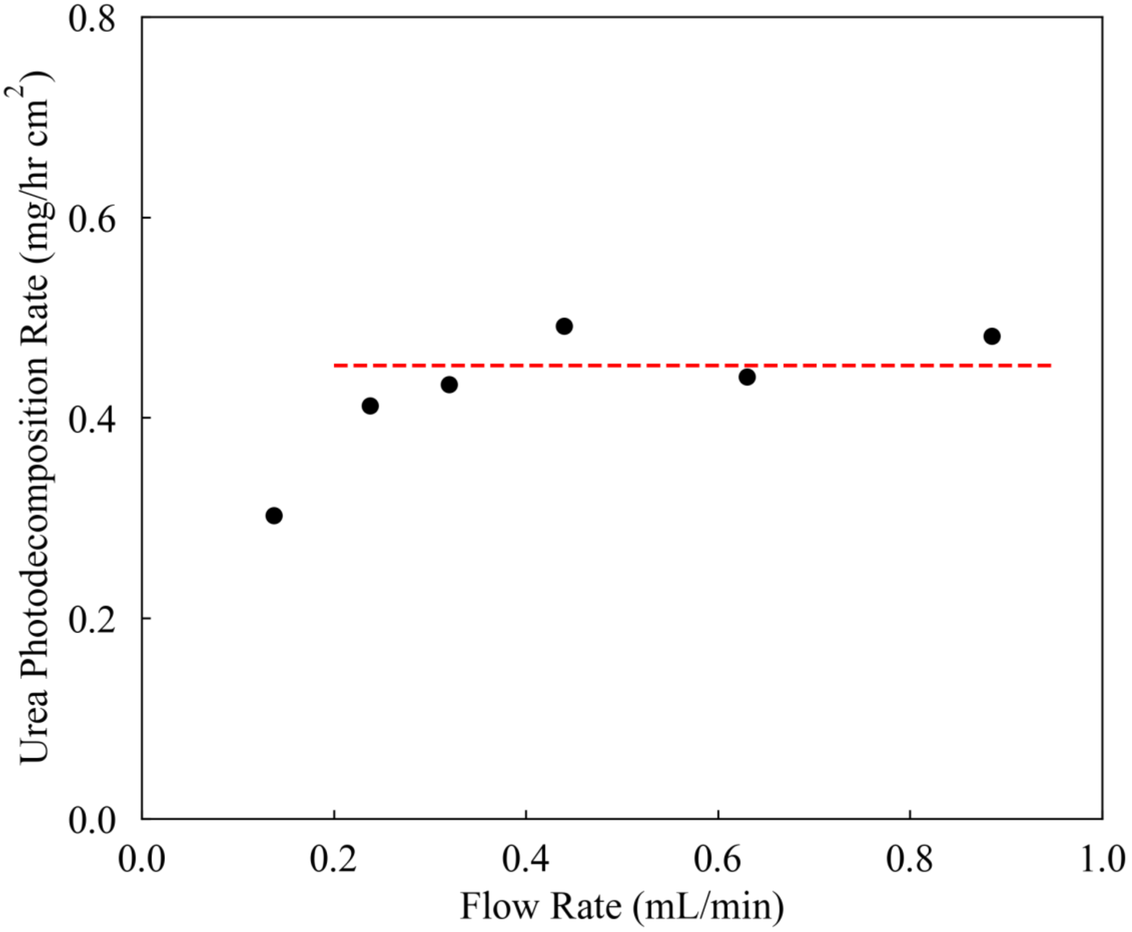

Figure 3.1. Urea photodecomposition rate measured under different flow rates, with 10mM urea in the feeding solution. The POUR operation voltage is 0.5V and the UV light intensity is 48.0mW/cm^2.

To investigate the urea concentration dependency, solutions with different urea concentrations were fed into the POUR panel. For 10mM urea solution, 0.6mL/min flow rate is chosen to obtain ~45% concentration drop at the outlet, thus for a 5mM urea solution the flow rate would be changed to 1.2mL/min and for a 20mM urea solution the flow rate should be changed to 0.3mL/min in order to obtain a similar concentration drop at the outlet of the POUR for a more accurate urea concentration measurement with the urea detection kit. As the urea photodecomposition rate at the TiO_2 surface in POUR panel is not dependent on the flow rate, it validates the observation from Figure 3.2 that the urea photodecomposition rate is not affected by the urea concentration (>2mM), which further suggests that the reaction is not mass transport limited as well as not concentration dependent shown in the reaction rate law (rate = $k[A]^n$). The average measured urea photodecomposition rate from Figure 3.2 is around 0.546mg hr^{-1} cm^{-2}, when urea concentration is ranging from 2mM to 100mM.

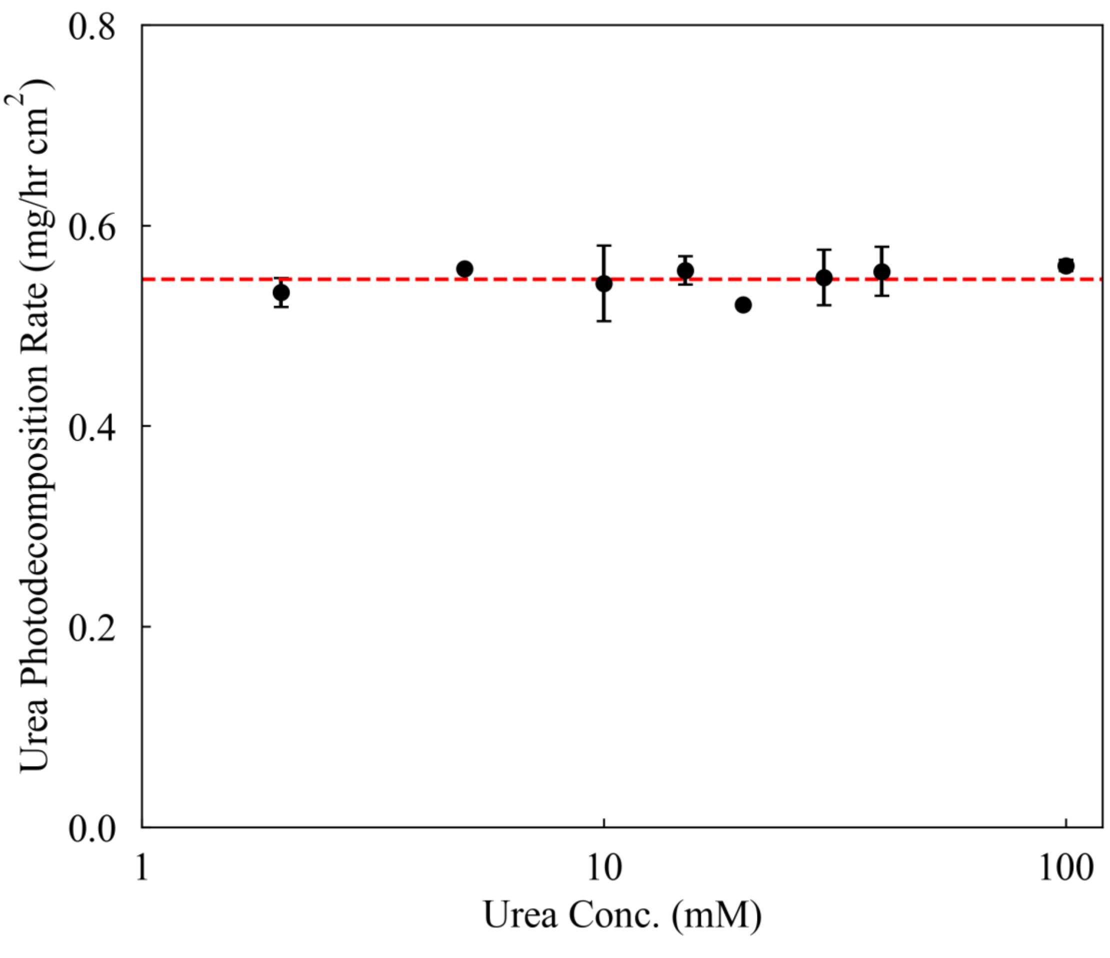

Figure 3.2. Urea photodecomposition rate measured with different urea concentrations in the feeding solution. The POUR operation voltage is 0.5V and the UV light intensity is 48.0mW/cm^2. Standard flow rate for 10mM urea solution is 0.6mL/min, and in order to have

similar urea concentration drop after the photodecomposition reaction at TiO_2 surface, with 5mM urea in the feeding solution, the flow rate would be changed to 1.2mL/min; with 20mM urea in the feeding solution, the flow rate would be changed to 0.3mL/min, and so forth.

Since the reaction is not mass-transport limited nor urea concentration dependent, the relationship between the measured photocurrent and the urea photodecomposition rate was determined. Photocurrent would be a direct measure of holes (h^+) that react at surface since measured e^- current goes through the potentiostat to the cathode. By adding bare FTO glasses (starting from 0 to 4 slides) in front of the POUR panel, the intensity of the UV light irradiated on the photoanode (TiO_2/FTO glass) side was reduced and thus leading to a decreasing photocurrent. The urea photodecomposition rate under each corresponding UV light intensity was also measured. As shown in Figure 3.3, the urea photo-oxidation reaction rate is linear to the measured photocurrent, with the intercept of trendline set to be (0,0) in the plot. Therefore, further study on factors affecting the photocurrent was conducted in order to find out the potential approaches to improve the POUR performance on photo-oxidizing urea into N_2 and CO_2.

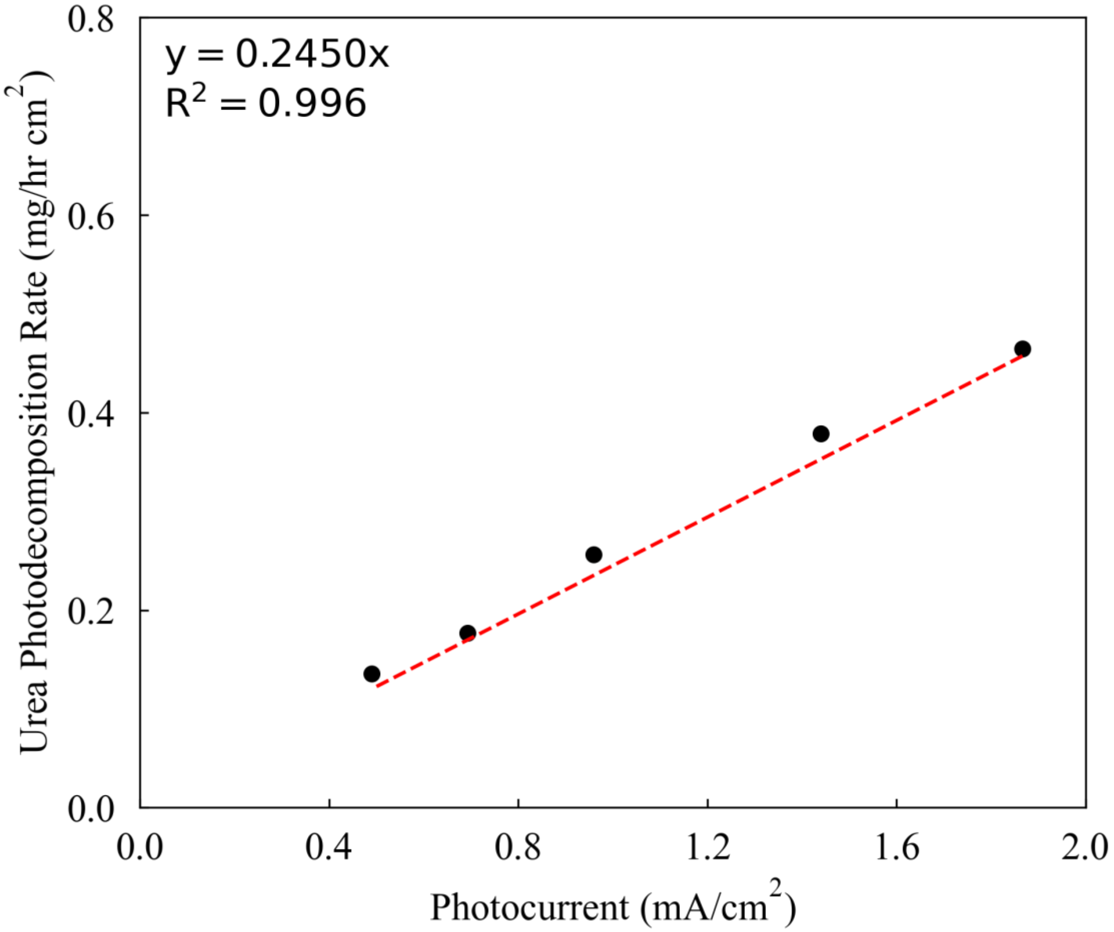

Figure 3.3. Relationship between the measured photocurrent and the urea photodecomposition rate. The distance between the UV LEDs and the POUR panel is 1.5 cm, and the initial UV light intensity is measured to be 48.0mW/cm^2. Bare FTO glasses (starting from 0 to 4 slides) were added in front of the POUR panel to change the intensity of UV irradiation and the photocurrent.

Figure 3.4 a) and b) show the photocurrent measured and quantum efficiency (QE) calculated under different UV light intensities and with different external voltages applied. When no external voltage was applied (0V), the measured photocurrent is extremely low down to the range between 0.01 to 0.15mA/cm^2, and the corresponding QE was calculated to be in the range between 2.9-1.6%. After applying a small 0.3V external voltage across the electrodes, the measured photocurrent and calculated QE show a dramatic increase compared to that with 0V. The external voltage applied helps the charge carrier (e^-/h^+ pairs) separation and thus reduces the recombination process.[10] However, when the UV irradiation goes above 23mW/cm^2, the photocurrent seems to reach a saturation state and stops to be linear to the light intensity. This might be due to the increased built-up internal electric field induced by more photo-excited e-/h+ pairs canceling out the charge carrier separation effect from the applied external voltage. The fast drop of QE from 22% to 8% (with 0.3V applied) shown in Figure 3.4 (b) also confirmed the hypothesis. When 0.5V was applied, the photocurrent is close to linear proportional to the light intensity (under a maximum of 40mW/cm^2 UV irradiation), and the QE is around 25.2-15% which is ~10x higher comparing to the QE measured with 0V applied voltage. Further increase the applied voltage to 1.5V, QE calculated under the same light intensity range increased to 28.7-22.2%, which only shows a slight increase (1.1– 1.5x) comparing to the QE measured with 0.5V external voltage, suggesting an upper-limit of electron/hole reaction efficiency of our TiO_2/FTO glass and Pt/carbonpaper system with applied positive bias to the anode. With voltages at or higher than 1.5V there is significant water splitting and as discussed later, free chlorine species formation, thus in practice a 0.5V has been chosen as the operation voltage to have sufficient QE and minimize byproduct formation for the portable kidney dialysis device application. At 0.5V bias the quantum efficiency appears to drop linearly with light intensity 22% at 8.63 mW/cm^2 to 15% at 39.25mW/cm^2. A linear extrapolation of Figure 3.4 b) to double the light intensity (68 mW/cm^2) would have the QE drop to 8%, thus simply increasing the light intensity beyond 39.25mW/cm^2 will have only a minor increase in urea reaction rate, as shown in Figure 3.4 c)

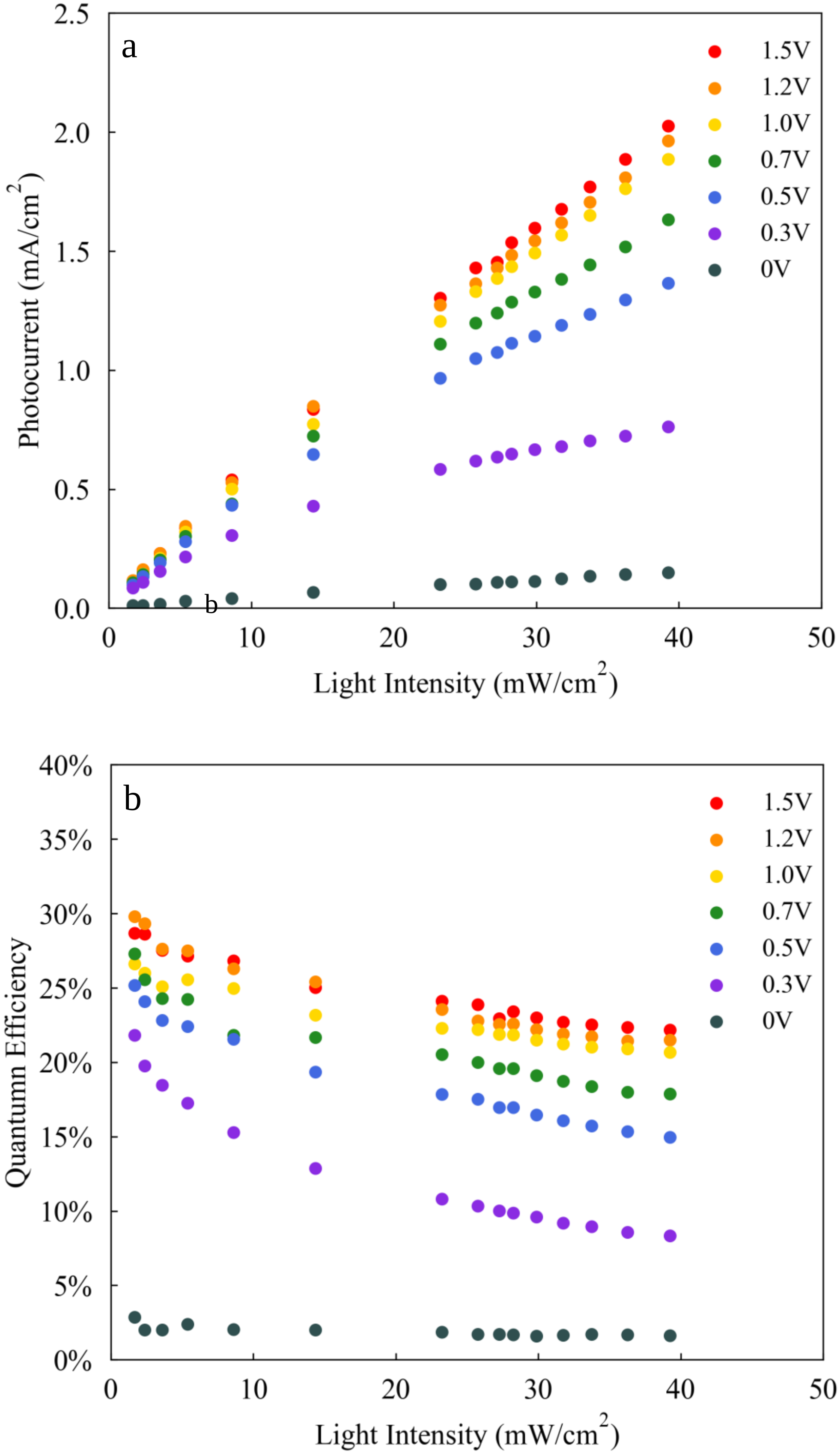
a
b
2.5
2.0
1.5
1.0
0.5
0.0
Photocurrent (mA/cm^2)
0
10
20
30
40
50
Light Intensity (mW/cm^2)
1.5V
1.2V
1.0V
0.7V
0.5V
0.3V
0V
b
40%
35%
30%
25%
20%
15%
10%
5%
0%
Quantumn Efficiency
0
10
20
30
40
50
Light Intensity (mW/cm^2)
1.5V
1.2V
1.0V
0.7V
0.5V
0.3V
0V

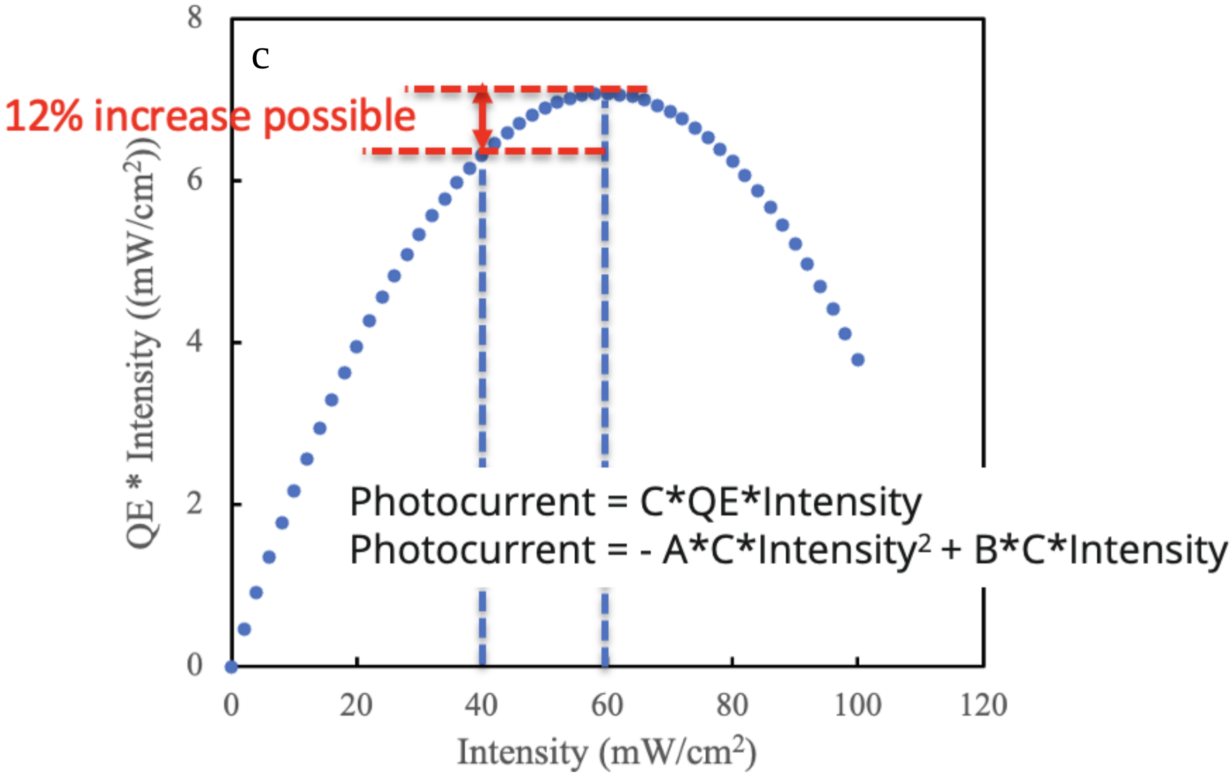

Figure 3.4. (a) Photocurrent measured and (b) quantum efficiency calculated under different light intensities with different external voltages applied. The distance between the UV LEDs (365nm) and the POUR panel is 3cm, and the initial UV light intensity is measured to be 39.25 mW/cm^2. The UV light intensity was changed by adding bare microscope glass substrates (up to 7 slides) and additional FTO/glass (up to 7 slides) in front of the POUR panel.

Cyclic Voltammetry (CV) scans were also conducted under dark and under different light intensities shown in Figure 3.5, suggesting that a higher photocurrent could be generated when irradiating the TiO_2/FTO glass with a higher UV light intensity. Meanwhile, for CV scans measured under a certain UV light intensity, when the applied voltage goes above 0.5V, the photocurrent no longer has a linear increase and could reach a saturation state. This saturation phenomenon observed in CV scans could be explained by the limitation of the maximum amount of e^-/h^+ pairs generated by a fixed photon flux (fixed light intensity), and 0.5V is high enough to separate most of the charge carriers excited by the photons. Additionally, Figure 3.5 also shows that under dark condition, the "photocurrent" is one to two orders of magnitude lower than that under UV light irradiation, which indicates the photon excited e^-/h^+ pairs are the dominant species in the TiO_2 photo-oxidation reaction and the galvanic decomposition of urea by applied voltage is negligible.

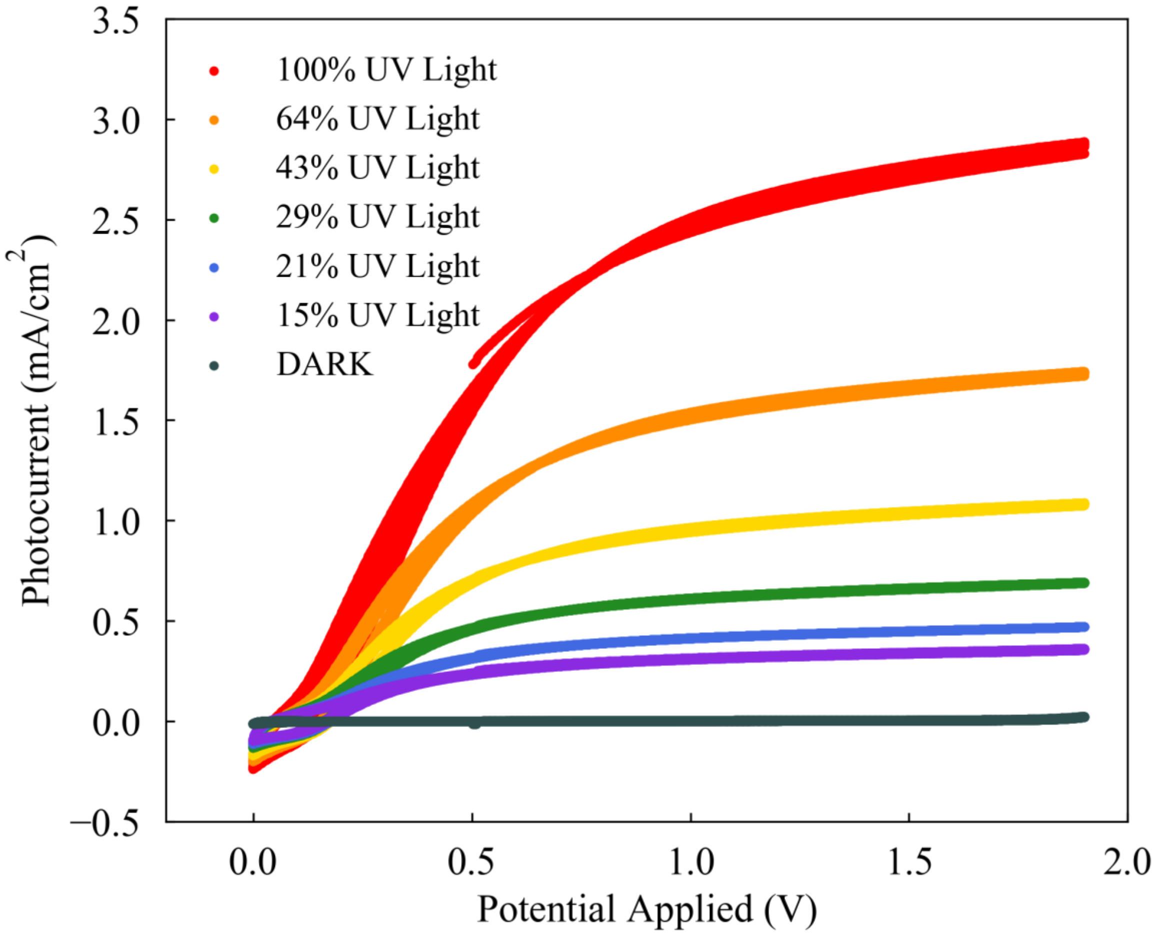

Figure 3.5. The C-V scans measured under different % of UV light intensity.

The distance between the UV LEDs and the POUR panel is 3cm, and the initial UV light intensity (100%) is measured to be 39.25 mW/cm^2. The UV light intensity was changed by adding bare FTO glasses (up to 5 slides) in front of the POUR panel.

Other than the CV scans, EIS spectra were measured with different applied voltages under dark and under UV light irradiation, illustrated in Figure 3.6. Under UV irradiation, TiO_2 is photo-excited by incident photons and e^-/h^+ pairs are generated, with h^+ being driven to the TiO_2 surface and e^- being injected into the circuit to the counter electrode. The semi-circles shown in the Nyquist plots in Figure 3.6 (a) indicates that the resistance at the interface is low and the lifetime of the e^-/h^+ pairs can be then calculated to be around 0.637ms via the following equation, emphasizing the importance of the applied external voltage, which facilitating the e^-/h^+ pair separation and prohibiting the recombination process.[12, 22, 23]

$$\tau_n = \frac{1}{\omega_{min}} = \frac{1}{2\pi f_{min}}$$

The photocatalytic reaction rate at TiO_2 surface under UV irradiation can be obtained from the EIS plot shown in Figure 3.6 (b), which is in the magnitude of 10^2 per sec. Whereas, under dark condition shown in Figure 3.6 (c), TiO_2 is not activated or photo-excited by photon and does not have e^-/h^+ pairs as charge carriers to be considered as conductive, thus the Nyquist plots exhibit large semi-circles indicating a high ohm resistance within the system. Moreover, since there is no e^-/h^+ pair assisted photocatalytic reaction occurring on the electrode surfaces, the reaction rate obtained in Figure 3.6 (d) is in the magnitude of 10^{-1} per sec, which is three orders of magnitude lower than that under UV irradiation.

Taking the average urea photodecomposition rate to be around 0.45mg/hr cm^2 TiO_2/FTO glass, that is $1.25x10^{15}$ urea being reacted per sec per cm^2 TiO_2/FTO glass. The characteristic reaction time obtained from the EIS results is 0.637ms, thus there are $0.80x10^{12}$ urea molecules reacted per cm^2 TiO_2/FTO glass. One the other hand, according to the SEM images, the actual surface area of TiO_2 nanowires is 30x of the planar area on the TiO_2/FTO glass. Since there are approximately $5.19x10^{14}$ unit cells per cm^2 of the TiO_2 surface, the estimated amount of 5-coordinated Ti_{5c} exposed on the TiO_2 surface is ~ $1.56x10^{16}$ per cm^2 TiO_2/FTO glass. Therefore, only 0.005% ($0.8x10^{12}/1.56x10^{16}$) of the surface exposed Ti_{5c}s are involved in the urea photo-oxidation reaction in the characteristic time, indicating there is an excessive amount of Ti_{5c} exposed at the TiO_2 surface but being non-reactive.

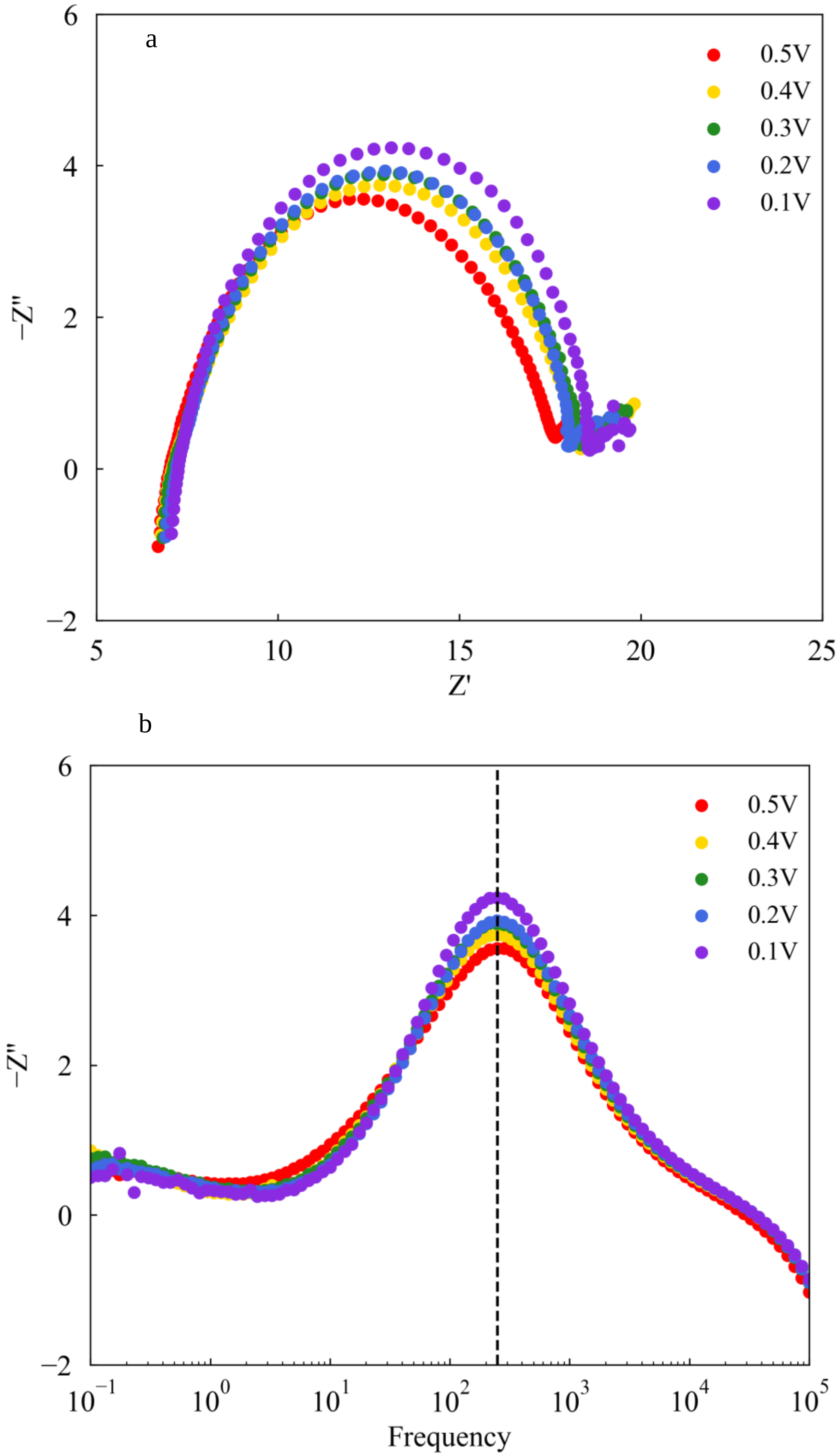
a
● 0.5V
● 0.4V
● 0.3V
● 0.2V
● 0.1V
−Z''
6
4
2
0
−2
5
10
15
20
25
Z'
b
● 0.5V
● 0.4V
● 0.3V
● 0.2V
● 0.1V
−Z''
6
4
2
0
−2
10^{-1}
10^{0}
10^{1}
10^{2}
10^{3}
10^{4}
10^{5}
Frequency

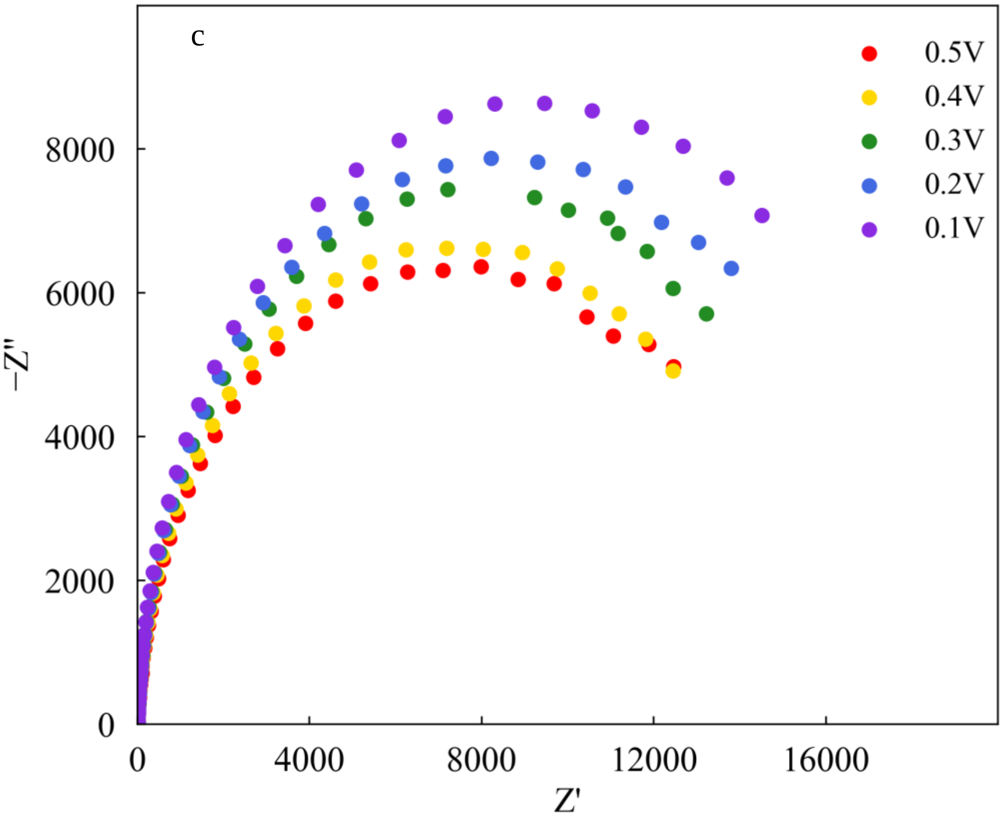
c
0.5V
0.4V
0.3V
0.2V
0.1V
−Z''
0
2000
4000
6000
8000
0
4000
8000
12000
16000
Z'

d

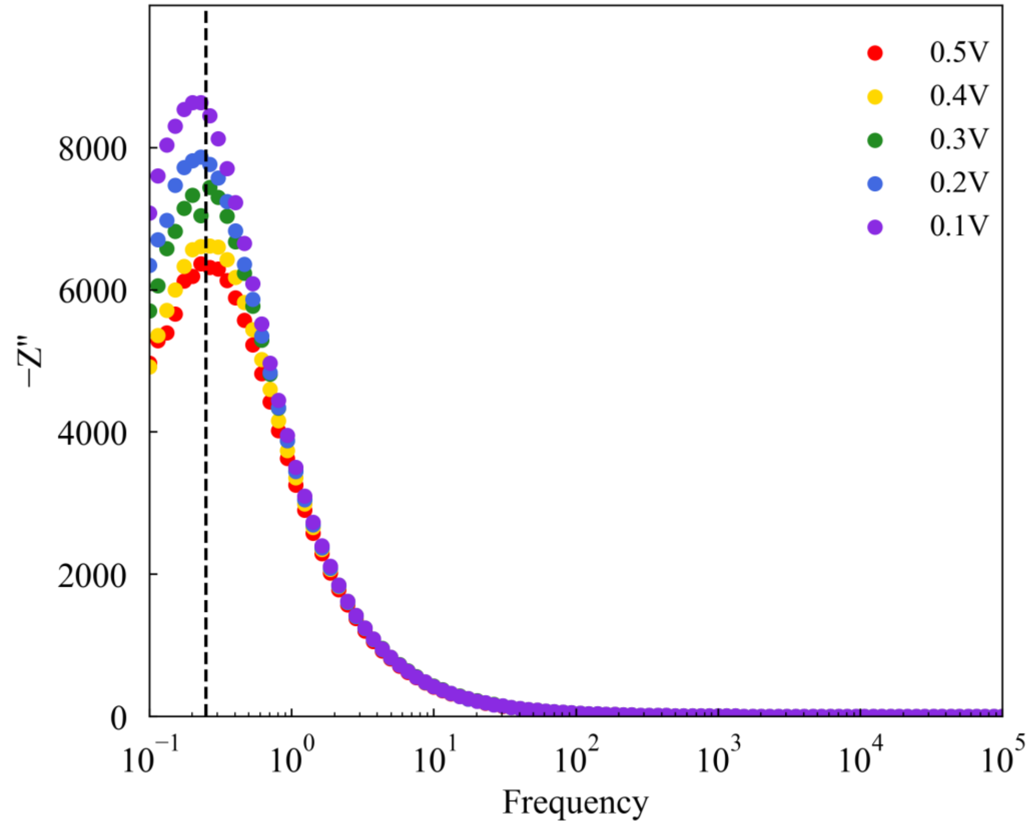
0.5V
0.4V
0.3V
0.2V
0.1V
−Z''
0
2000
4000
6000
8000
10^{-1}
10^{0}
10^{1}
10^{2}
10^{3}
10^{4}
10^{5}
Frequency

Figure 3.6. EIS spectra of the POUR panel measured under (a, b) UV light irradiation; (c, d) dark at different applied bias with frequency ranging from 10^5 to 0.1Hz. The distance between the UV LEDs and the POUR panel is 1.5 cm, and the UV light intensity is 48.0mW/cm^2.

3.3.2 *Mechanistic investigations on urea photo-oxidation reaction at TiO_2 surface*

Though there are limited reports of urea photodecomposition on TiO2, there is significant literature on ammonia photooxidation.[17, 24-29] Urea is similar to ammonia with one hydrogen replaced by a bond to the carbonyl carbon, and is in the non-protonated state. Thus, we would expect non-protonated ammonia (high pH) to have a similar reaction mechanism as urea. The nitrogen electron lone pair potentially can form Ti-N bond with TiO_2 as an important intermediate step indicated by Ichihashi's group's study of ammonia photo-oxidation.[30] Assuming that for each urea ($CO(NH_2)_2$) being photodecomposed, two NH_4Cl/NH_3 could be thus photo-oxidized. Therefore, the 20mM NH_4Cl solution was initially prepared in acidic condition (pH=6.7) and fed into the POUR system for the photodecomposition process. By converting the NH_4Cl photodecomposition rate into mg urea per hour per cm^2, we observed an extremely low photo-oxidation rate which is only about 0.13 mg urea hr^{-1} cm^{-2} (~1/4 of the typical urea decomposition rate in the POUR system) shown in Figure 3.7. Adjusting the pH environment from acidic to alkaline (pH=9.4), NH_4^+ cations were converted into NH_3 which would have their lone pair of electrons exposed to the reaction environment and TiO_2 surface. The equivalent photodecomposition rate in this case is around 0.5 mg urea hr^{-1} cm^{-2}, which is 3.8x higher than under acidic condition and is close to the actual urea decomposition rate in the POUR system (0.45 mg urea hr^{-1} cm^{-2}). Therefore, the photo-oxidation reaction mechanism for NH_3 and urea on TiO_2 surface should be similar and the lone pair of electrons on non-protonated $-NH_2$ is important for decomposition reaction. Additionally, since the photodecomposition rate of NH_3 is close to that of the urea, breaking the C-N bond in urea is not the rate limiting step in its reaction pathways.

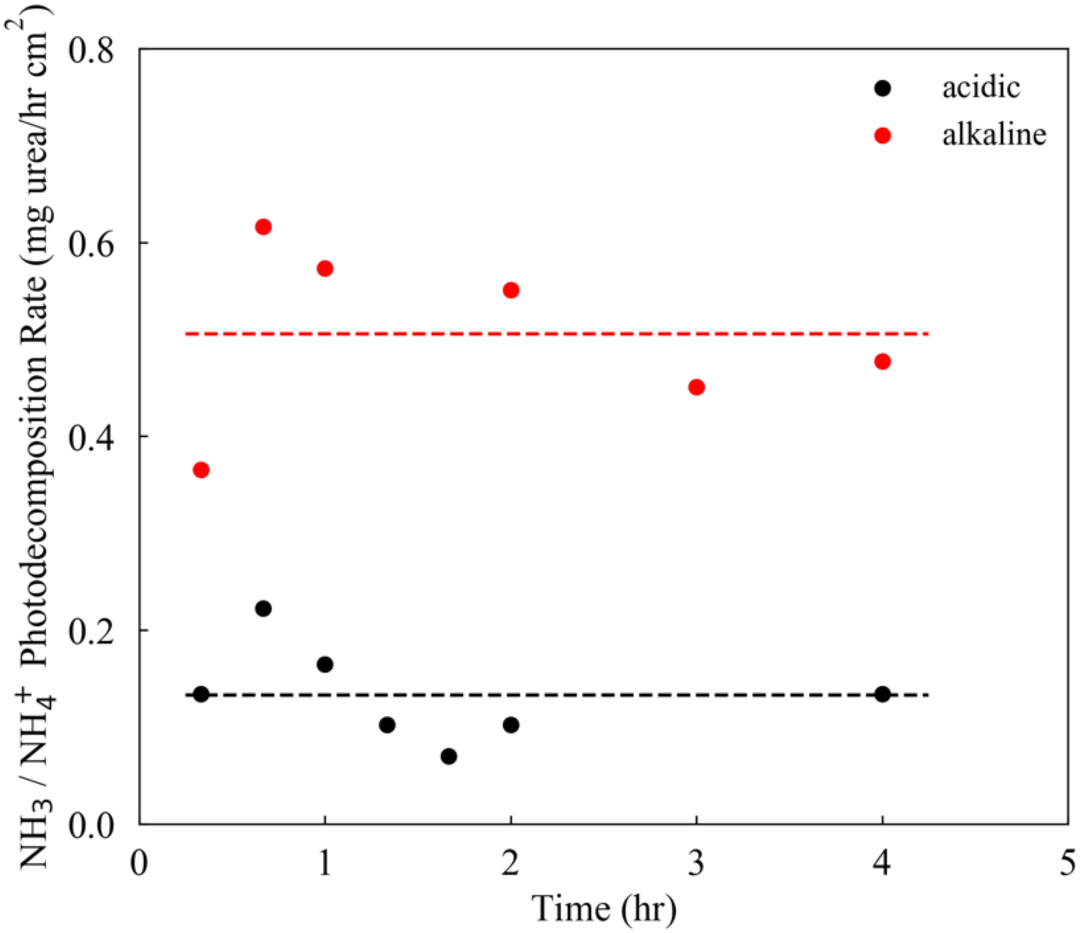

Figure 3.7. NH_3/NH_4^+ photodecomposition rate measured under acidic (pH 6.7) and alkaline (pH 9.4) conditions in the unit of mg urea/hr cm^2. The NH_3/NH_4^+ photodecomposition rate in the unit of mg urea/hr cm^2 is calculated based on the assumption that photodecomposing 2 NH_3/NH_4^+ is equal to 1 urea molecule being decomposed.

The type of anions in the aqueous solution is also considered as a crucial factor that could affect the urea photodecomposition pathway on TiO_2 surface reaction as suggested by Zhou's group in their WO_3 chlorine-assisted ammonia photo-oxidation system. Thus, NaCl (physiological

0.15M) in the standard 10mM urea solution has been substituted with Na_2SO_4 and in order to keep the ionic strength in the solution to be the same, the substitution ratio between NaCl and Na_2SO_4 is 3:1. Also, we further increased the NaCl concentration in the 10mM urea solution from 0.15M to 0.2M and 0.3M to investigate that whether more chlorine or a higher $Cl^-/-NH_2$ ratio in the solution could help to improve the urea photodecomposition performance at the TiO_2 surface. Nitrate, one of the undesired toxic by-products that could be formed from urea photo-oxidation reaction, was also measured for these experiments and the percentage of oxidized urea into nitrate was then calculated, shown in Table 3.1. When there is no chlorine in the solution, the urea photodecomposition rate is around half of the value measured in the standard 0.15M NaCl condition and regarding to the nitrate formation in the urea photo-oxidation reaction, all the urea has been oxidized into nitrate with no N_2 formed as the final product. When further increased the NaCl concentration in 10mM urea solution to 0.015M (10% of the standard 0.15M), urea photodecomposition rate is still low with all the urea being oxidized into nitrate. However, with $Cl^-/-NH_2$ ratio going up to 6:1 (0.12M NaCl in urea solution), the urea photodecomposition rate shows a 65% increase to 0.35 mg hr^{-1} cm^{-2}, which is about 83% of the rate measured in standard 10mM urea 0.15M NaCl solution. Meanwhile, the nitrate formation rate shows a dramatic drop (~90% drop) to 0.041mg hr^{-1} cm^{-2}, which indicates that nitrate is no longer the major product from urea photo-oxidation reaction on the TiO_2 surface. Therefore, SO_4^{2-} does not function as a poisoning species to prohibit urea photo-oxidation reaction but is not as efficient as Cl^- and critically has undesired nitrate as the final product. Shown below is the formal electrochemical equation to form nitrate, using $16e^-$ (vs $6e^-$ for N2 product) making it 2.3x less current efficient. However, it is possible to form $S_2O_4^{2-}$, as a source of O for NO_3^-, reducing the require charge transfers.

Anode: $CO(NH_2)_2 + 7H_2O + 16e^- + 16h^+ \rightarrow CO_2 + 2NO_3^- + 18H^+ + 16e^-_{circuit}$

Cathode: $4O_2 + 8H_2O + 16e^-_{circuit} \rightarrow 16OH^-$

Overall: $CO(NH_2)_2 + 4O_2 \rightarrow CO_2 + 2NO_3^- + H_2O + 2H^+$

As a result of this anion substitution experiment, Cl^- is considered as an important intermediate involved in the photo-oxidation reaction on the TiO_2 surface for urea being decomposed into N_2 and CO_2. However, further increasing the NaCl concentration in the solution from 0.15M to 0.2M and 0.3M, with the $Cl^-/-NH_2$ ratio increased from 7.5:1 to 10:1 and 15:1, the urea photodecomposition rate and nitrate formation rate show little difference as is shown in Table 3.1. Thus, at these concentrations, the surface reaction with holes would be the rate limiting step not concentration of Cl^-.

Other than the study on the urea photodecomposition and nitrate formation rate in these experiments, based on the photocurrent recorded under each experimental condition, the photocurrent efficiency towards urea decomposition reaction could thus be calculated, as listed in Table 3.1. Under all these conditions, 60% to 76% of the measured photocurrent is effectively involved in the urea decomposition reaction, which indicates a strong selectivity for urea photo-oxidation reaction at the TiO_2 surface.

Table 3.5. The urea photodecomposition rate and nitrate formation rate measured in 10mM urea solutions with different $Cl^-/-NH_2$ ratios by substituting SO_4^{2-} for Cl^-. The percentage of oxidized

urea into nitrate and photocurrent efficiency towards urea photodecomposition are calculated for each condition, respectively.

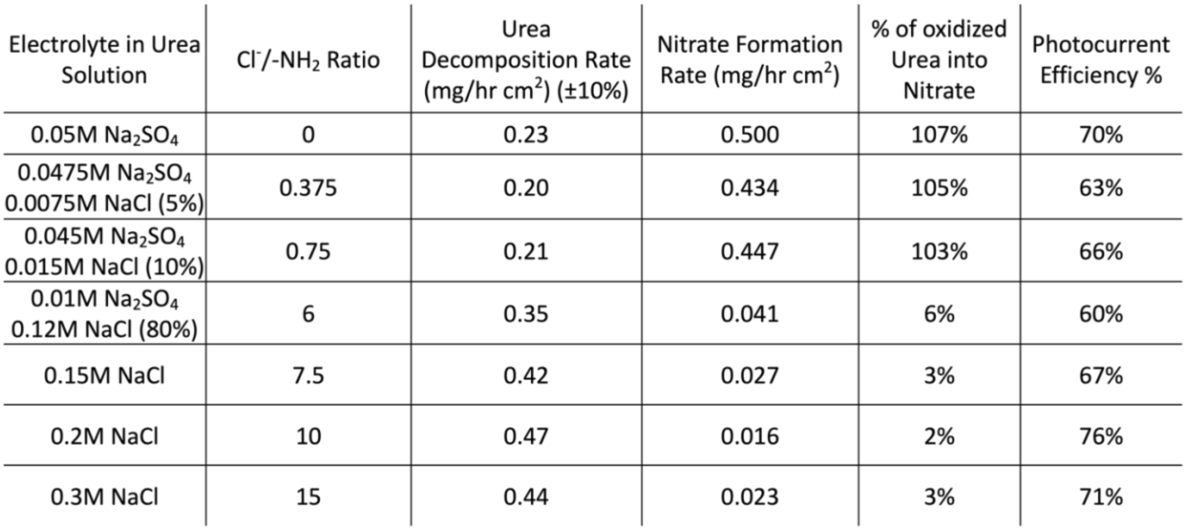

Electrolyte in Urea Solution	$Cl^-/-NH_2$ Ratio	Urea Decomposition Rate (mg/hr cm^2) (±10%)	Nitrate Formation Rate (mg/hr cm^2)	% of oxidized Urea into Nitrate	Photocurrent Efficiency %
0.05M Na_2SO_4	0	0.23	0.500	107%	70%
0.0475M Na_2SO_4 0.0075M NaCl (5%)	0.375	0.20	0.434	105%	63%
0.045M Na_2SO_4 0.015M NaCl (10%)	0.75	0.21	0.447	103%	66%
0.01M Na_2SO_4 0.12M NaCl (80%)	6	0.35	0.041	6%	60%
0.15M NaCl	7.5	0.42	0.027	3%	67%
0.2M NaCl	10	0.47	0.016	2%	76%
0.3M NaCl	15	0.44	0.023	3%	71%

Since gas permeable carbonpaper is used as the counter electrode, O_2 can freely diffuse into the system and react with urea at TiO_2 surface to form nitrate. In order to exclude this possibility, additional experiments were conducted by bubbling different gas species into the 10mM urea 0.15M NaCl solution and measuring the corresponding urea photodecomposition and nitrate formation rate, shown in Table 3.2. By bubbling air, pure N_2, O_2, and Ar during the POUR operation, the urea photodecomposition rate does not show a notable change as well as the nitrate formation rate. The percentage of urea being photo-oxidized into nitrate in all these four bubbling experiments is nearly the same at around 4%, which is consistent with the previous experiment results shown in Table 3.1. Therefore, the gas dissolved in urea solution is not involved in the urea photo-oxidation reaction at TiO_2 surface and the nitrate is not formed due to dissolved O_2 reacting with the TiO_2 surface.

Table 3.6. The urea photodecomposition rate and nitrate formation rate measured in 10mM urea 0.15M NaCl solution when bubbling various kinds of gas species during the POUR operation. The photocurrent was recorded and the percentage of oxidized urea into nitrate are calculated for each condition, respectively.

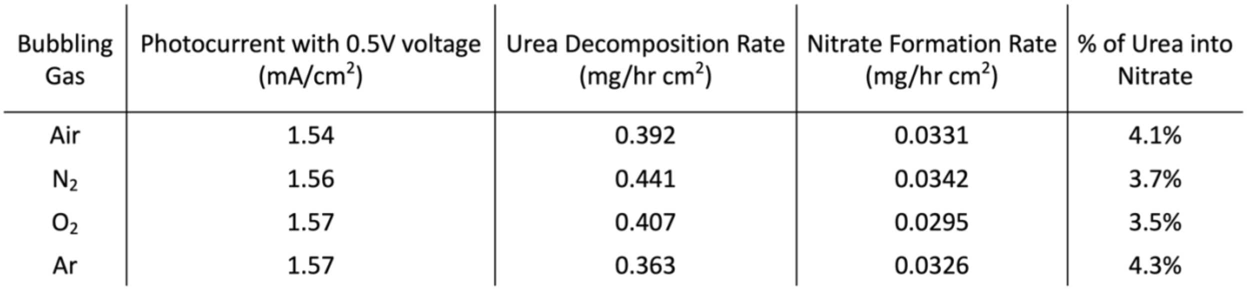

Bubbling Gas	Photocurrent with 0.5V voltage (mA/cm^2)	Urea Decomposition Rate ($mg/hr\ cm^2$)	Nitrate Formation Rate ($mg/hr\ cm^2$)	% of Urea into Nitrate
Air	1.54	0.392	0.0331	4.1%
N_2	1.56	0.441	0.0342	3.7%
O_2	1.57	0.407	0.0295	3.5%
Ar	1.57	0.363	0.0326	4.3%

Besides nitrate and N_2 as the oxidation product from urea, CO_2 is also an important reaction product, which could form HCO_3^-/CO_3^{2-} in aqueous POUR system (~3mM CO_3^{2-}/HCO_3^- was detected from the outlet of the single-pass experiment by titration). Meanwhile, the HCO_3^- concentration in the common blood dialysate buffer is about 37mM. Thus, a series of HCO_3^- anion substitution experiments were conducted and the urea photodecomposition as well as the nitrate formation rates were measured under each condition, listed in Table 3.3. By substituting HCO_3^- for Cl^-, the urea photodecomposition rate is decreased. Even with 0.12M NaCl and 0.06M $NaHCO_3$ in the 10mM urea solution ($Cl^-/-NH_2$ ratio = 6), the urea decomposition reaction rate is still less than 20% of that with 0.15M NaCl in the solution. Unlike the SO_4^{2-} anion substitution, HCO_3^-, appears not to react with the photo-excited h^+ and urea. Water molecules (H_2O) with a very high concentration in aqueous solution (55 mol/L) could compete against the low-concentration Cl^- ions (0.15M) to form hydroxyl radicals ($HO\cdot$), however the results shown in Table 3.3 imply that the effect of $HO\cdot$ formed from H_2O at TiO_2 surface is negligible in urea photo-oxidation reaction.

$$H_2O + h^+ \rightarrow HO\cdot + H^+$$

Even at these low nitrate formation rates, there is no observed HCO_3^- concentrations dependance. In conclusion, HCO_3^- does not contribute to urea photo-oxidation reaction on TiO_2 surface, even to the nitrate, whereas SO_4^{2-} can help to decompose urea and to form nitrate. The photocurrent efficiency toward urea photodecomposition calculated for each condition shown in Table 3.3 also supports the proposed mechanism that Cl^- is the primary intermediate in the urea photo-oxidation reaction at TiO_2 surface into physiologically safe N_2 and CO_2.

Table 3.7. The urea photodecomposition rate and nitrate formation rate measured in 10mM urea solutions with different Cl^-/-NH_2 ratios by substituting HCO_3^- for Cl^-. The pH of the solution was recorded and the percentage of oxidized urea into nitrate and photocurrent efficiency towards urea photodecomposition are calculated for each condition, respectively.

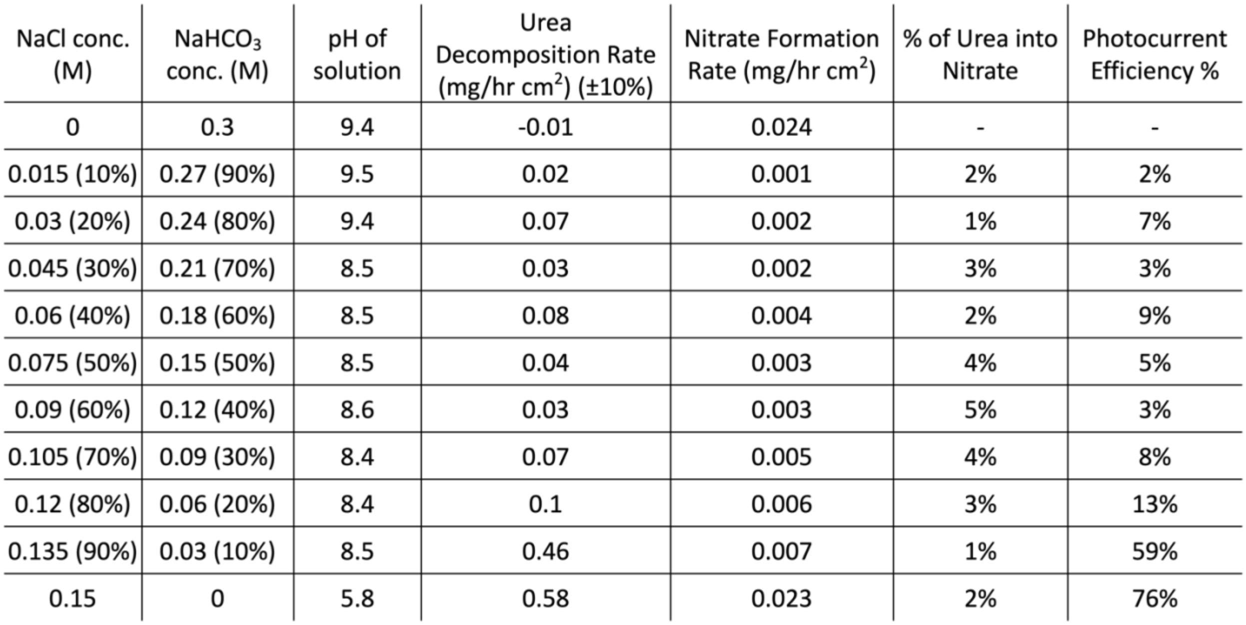

NaCl conc. (M)	$NaHCO_3$ conc. (M)	pH of solution	Urea Decomposition Rate (mg/hr cm^2) (±10%)	Nitrate Formation Rate (mg/hr cm^2)	% of Urea into Nitrate	Photocurrent Efficiency %
0	0.3	9.4	-0.01	0.024	-	-
0.015 (10%)	0.27 (90%)	9.5	0.02	0.001	2%	2%
0.03 (20%)	0.24 (80%)	9.4	0.07	0.002	1%	7%
0.045 (30%)	0.21 (70%)	8.5	0.03	0.002	3%	3%
0.06 (40%)	0.18 (60%)	8.5	0.08	0.004	2%	9%
0.075 (50%)	0.15 (50%)	8.5	0.04	0.003	4%	5%
0.09 (60%)	0.12 (40%)	8.6	0.03	0.003	5%	3%
0.105 (70%)	0.09 (30%)	8.4	0.07	0.005	4%	8%
0.12 (80%)	0.06 (20%)	8.4	0.1	0.006	3%	13%
0.135 (90%)	0.03 (10%)	8.5	0.46	0.007	1%	59%
0.15	0	5.8	0.58	0.023	2%	76%

When the TiO_2 is irradiated with UV light, the photo-excited holes (h^+) are generated at the surface with a strong oxidative capacity, which can oxidize water molecules (H_2O) into hydroxyl radicals (HO·) and Cl^- ions into chlorine radicals (Cl·). Both of these two radicals are strong oxidants but the HO· is found to be negligible in the urea photo-oxidation reaction. We propose two possible photo-oxidation pathways of urea into N_2 and CO_2 with the assistant of Cl^-/Cl· as key intermediate, shown in Figure 3.8. The TiO_2 surface bonded Cl· (Ti-Cl·) is an excited state generated by reacting the Cl^- in solution with the h^+ at TiO_2 surface under UV irradiation.

$$TiO_2 + h^+ + Cl^- \rightarrow \cdot Cl\text{-}TiO_2$$

The Ti-Cl· would then react with urea molecules in the solution to form Ti-N bond and thus capture the urea onto the TiO_2 surface, remove a urea nitrogen and release the HCl back into the solution. Since the complete oxidation of urea is a 6-step process, it is unlikely that radicals released into solution can efficiently react with 5 dilute intermediates to give complete reaction to N_2/CO_2, thus it is more likely to have surface bound urea that can directly receive the sequential h^+ at TiO_2 surface. The formation of Ti-N bonds was observed from the XPS results when exposed the TiO_2 surface to the urea solution with 3min UV irradiation. In order to prove that only the TiO_2 surface bonded Cl· (Ti-Cl·) is the key intermediate involved in the urea photo-oxidation reaction but not the dissolved Cl· or HO· radicals, the scavenger quenching experiments were conducted.

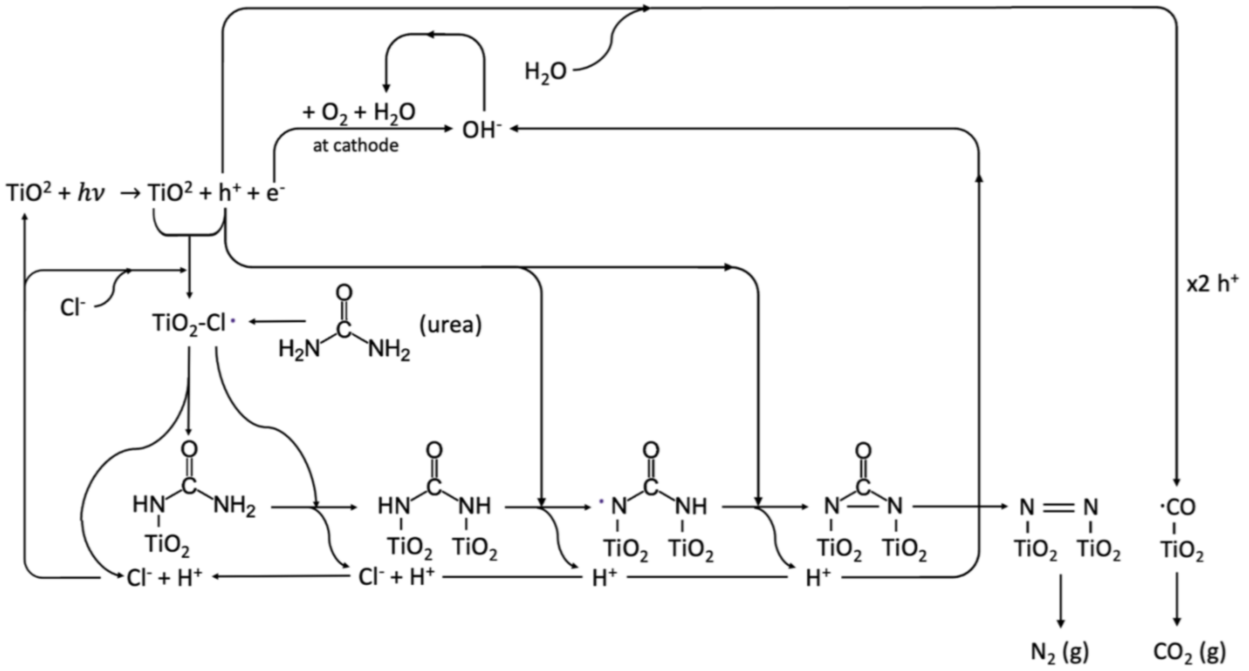

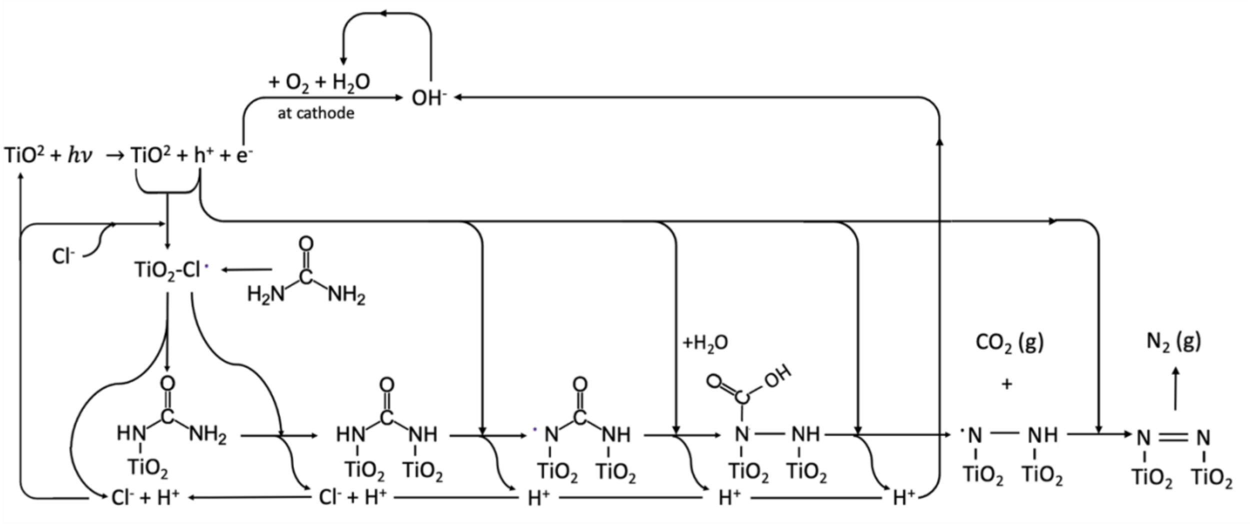

Figure 3.8. Proposed photo-oxidation pathways for urea into N_2 and CO_2, with the assistant of Ti-Cl· as key intermediates.

Tert-butyl alcohol can rapidly react with both Cl· and HO·, but only those dissolved in the solution.[17, 18] Those Cl· and HO· bonded on TiO_2 surface could not be quenched by the tert-butyl alcohol. Whereas another scavenger, allyl alcohol, can quench both surface bonded and dissolved Cl· and HO· easily.[18, 31, 32] Moreover, nitrobenzene was used as the radical scavenger only for quenching the HO· radicals.[17, 18, 33] Figure 3.9 shows the measured urea photodecomposition rates by adding tert-butyl alcohol, allyl alcohol and nitrobenzene as the radical scavenger, respectively with different scavenger concentrations. Table 3.4-3.6 also lists the measured nitrate and ammonia formation rates measured from the radical scavenger experiments.

By adding the tert-butyl alcohol to quench the Cl· and HO· radicals only in the solution, urea photodecomposition rate does not decrease significantly. Additionally, when the tert-butyl alcohol to urea ratio goes up to 21.5:1, the photodecomposition rate only decreases by 26.5%, indicating that the TiO_2 surface has a higher selectivity towards urea oxidation than tert-butyl alcohol. On the contrary, when allyl alcohol was added to quench both surface bonded and dissolved Cl· and HO· radicals, urea photodecomposition rate was effectively quenched. When 21.5mM allyl alcohol was added, the urea photodecomposition rate decreased by 44%, and with a higher allyl alcohol concentration (215mM) the decomposition rate could be decreased by 98%. Therefore, only TiO_2 surface bound Ti-Cl· and possibly Ti-O· radicals are important and involved in the urea photo-oxidation reaction. However, a high (20x) allyl alcohol concentration is needed to compete with the urea, thus the selectivity of urea photo-oxidation on TiO_2 surface very high suggesting urea intermediates that are bonded to the TiO_2 surface as proposed in Figure 3.8. Adding 2.15mM and 15.05mM nitrobenzene to quench only the HO· radicals, urea decomposition rate decreased by 15% and 24%, which is not effective as the allyl alcohol quenching agent, therefore the TiO_2 surface bonded Cl· radicals are the primary mechanism and HO· is minor in urea photo-oxidation reaction into N_2 and CO_2.

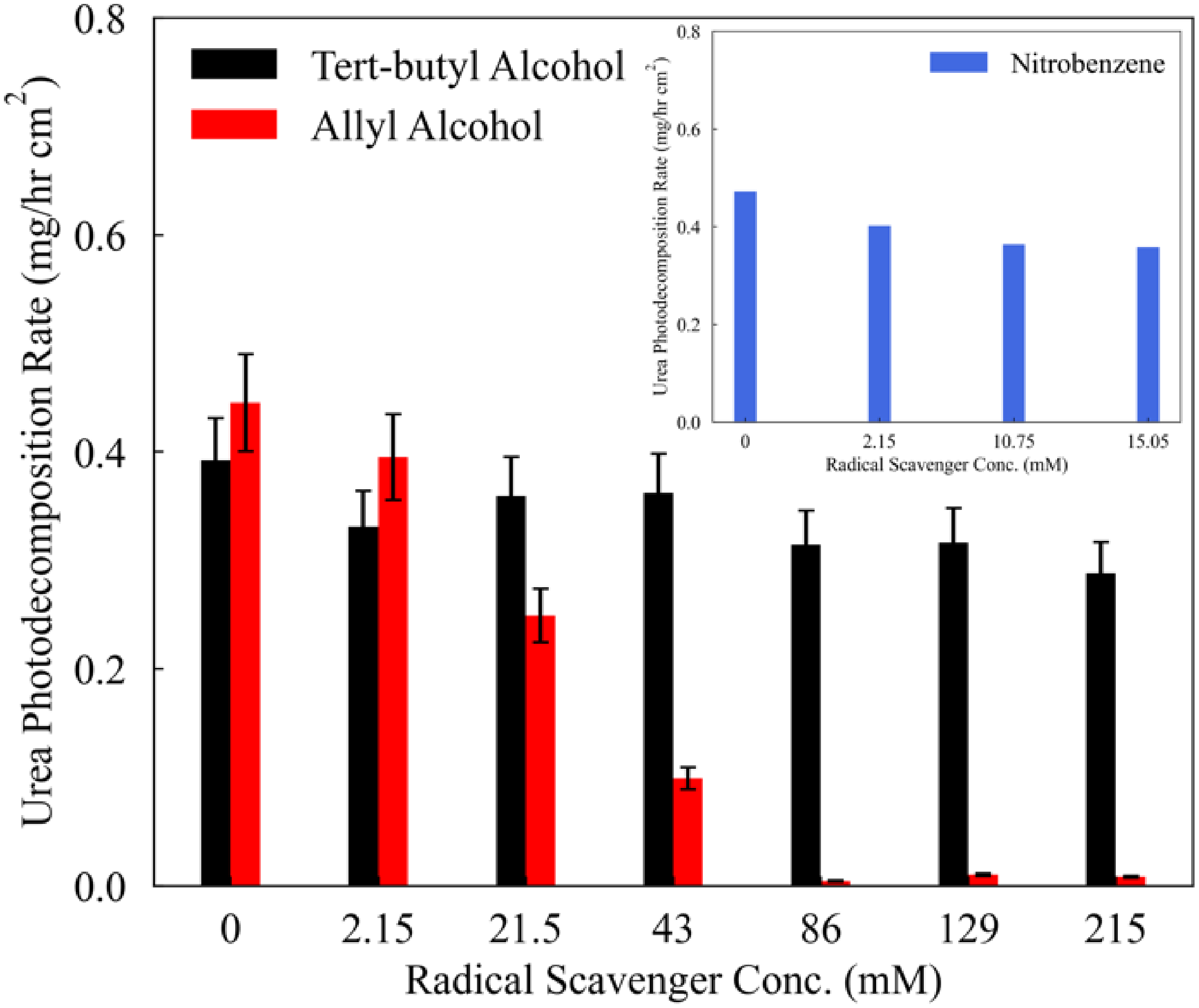

Figure 3.9. The urea decomposition rate measured with 10mM urea solution, by adding different types and amount of scavengers to quench the Cl· and HO· radicals bonded on the TiO_2 surface and/or dissolved in the solution.

Table 3.8. The urea decomposition rate and nitrate/ammonia formation rate measured in 10mM urea 0.15M NaCl solution with different amount of tert-butyl alcohol added as radical scavenger to quench the dissolved Cl· and HO·. The percentages of oxidized urea into nitrate and ammonia are calculated for each condition, respectively.

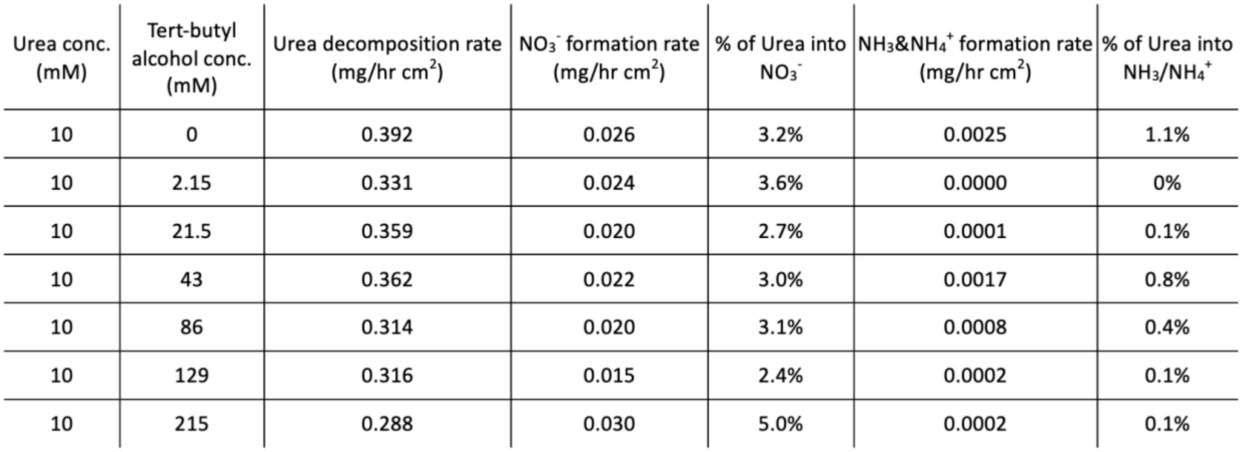

Urea conc. (mM)	Tert-butyl alcohol conc. (mM)	Urea decomposition rate (mg/hr cm^2)	NO_3^- formation rate (mg/hr cm^2)	% of Urea into NO_3^-	NH_3&NH_4^+ formation rate (mg/hr cm^2)	% of Urea into NH_3/NH_4^+
10	0	0.392	0.026	3.2%	0.0025	1.1%
10	2.15	0.331	0.024	3.6%	0.0000	0%
10	21.5	0.359	0.020	2.7%	0.0001	0.1%
10	43	0.362	0.022	3.0%	0.0017	0.8%
10	86	0.314	0.020	3.1%	0.0008	0.4%
10	129	0.316	0.015	2.4%	0.0002	0.1%
10	215	0.288	0.030	5.0%	0.0002	0.1%

Table 3.9. The urea decomposition rate and nitrate/ammonia formation rate measured in 10mM urea 0.15M NaCl solution with different amount of allyl alcohol added as radical scavenger to quench the dissolved Cl· and HO·. The percentages of oxidized urea into nitrate and ammonia are calculated for each condition, respectively.

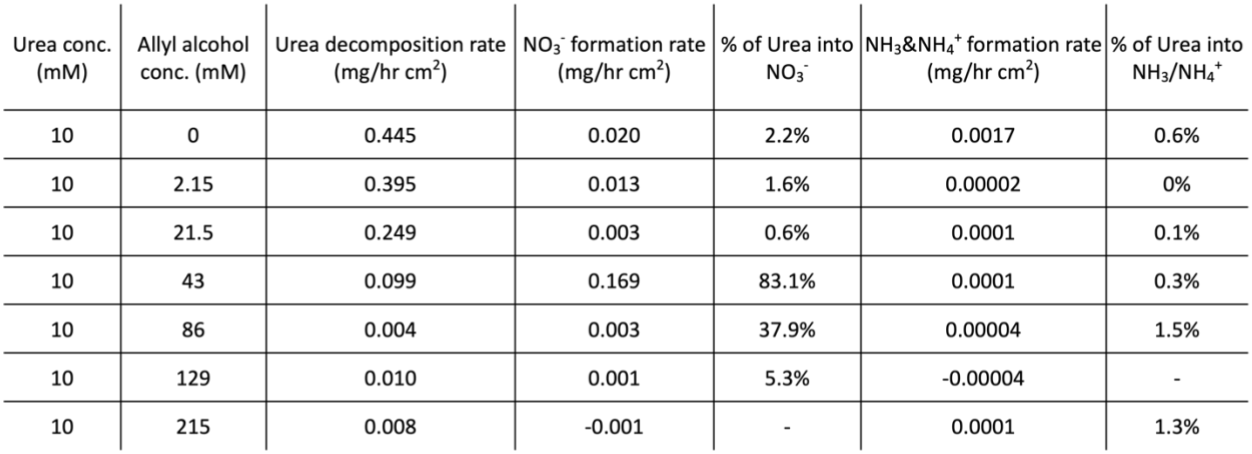

Urea conc. (mM)	Allyl alcohol conc. (mM)	Urea decomposition rate (mg/hr cm^2)	NO_3^- formation rate (mg/hr cm^2)	% of Urea into NO_3^-	NH_3&NH_4^+ formation rate (mg/hr cm^2)	% of Urea into NH_3/NH_4^+
10	0	0.445	0.020	2.2%	0.0017	0.6%
10	2.15	0.395	0.013	1.6%	0.00002	0%
10	21.5	0.249	0.003	0.6%	0.0001	0.1%
10	43	0.099	0.169	83.1%	0.0001	0.3%
10	86	0.004	0.003	37.9%	0.00004	1.5%
10	129	0.010	0.001	5.3%	-0.00004	-
10	215	0.008	-0.001	-	0.0001	1.3%

Table 3.10. The urea decomposition rate and nitrate/ammonia formation rate measured in 10mM urea 0.15M NaCl solution with different amount of nitrobenzene alcohol added as radical scavenger to quench the dissolved Cl· and HO·. The percentages of oxidized urea into nitrate and ammonia are calculated for each condition, respectively.

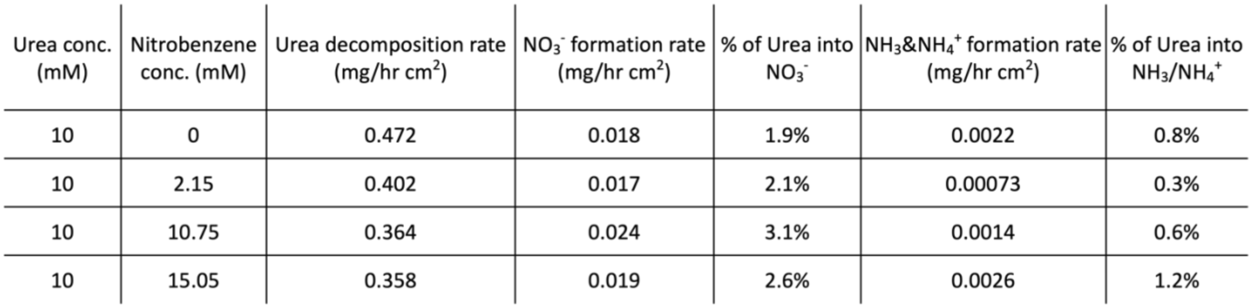

Urea conc. (mM)	Nitrobenzene conc. (mM)	Urea decomposition rate (mg/hr cm^2)	NO_3^- formation rate (mg/hr cm^2)	% of Urea into NO_3^-	NH_3&NH_4^+ formation rate (mg/hr cm^2)	% of Urea into NH_3/NH_4^+
10	0	0.472	0.018	1.9%	0.0022	0.8%
10	2.15	0.402	0.017	2.1%	0.00073	0.3%
10	10.75	0.364	0.024	3.1%	0.0014	0.6%
10	15.05	0.358	0.019	2.6%	0.0026	1.2%

3.4 CONCLUSION AND FUTURE WORK

In conclusion, this study reveals that the urea photo-oxidation reaction at the TiO_2 surface is not mass transport limited but surface reaction limited by the photo-excited h^+ reaction, according to flow-rate and urea-concentration dependency experiments. The application of an external voltage is required to improve the urea photodecomposition rate by drawing e^- into the circuit to reduce the recombination process at the TiO_2 surface. By applying the external voltage across the electrodes from 0V to 1.5V, QE measured under 39.25mW/cm^2 UV irradiation increased from 2% to 22%. However, the applied voltage should be at a maximum of 1.5V in order to avoid side-reactions to form toxic NH_3/NH_4^+ or NO_3^-. QE is seen to drop linearly with light intensity and 48mW/cm^2 is near the maximum urea oxidation rate in this system. Moreover, the crucial role of TiO_2 surface bound chlorine via reaction of chloride anion with TiO_2 hole forming reactive Ti-Cl· has been revealed as the key intermediates in the urea photo-oxidation reaction. The efficient photodecomposition of urea completely into N_2 and CO_2 suggests Ti-N bond formation in the urea photo-oxidation reaction at the TiO_2 surface. All these findings offer valuable insights for designing an efficient and selective photocatalytic system in wearable dialysis devices, providing a promising approach for continuous and effective urea removal to benefit patients with kidney disease.

For the future work, a more detailed and complicated computational modeling will be conducted with DFT simulations for the urea photo-oxidation reaction at the TiO_2 surface with Ti-Cl^- and Ti-Cl· as the key intermediates. Free energy diagram will be generated computationally to help understand the reaction mechanism and charge distribution density maps will be simulated for each reaction steps to confirm the bond formation process (Ti-N, N=N, etc.) during the urea photo-oxidation reaction at the TiO_2 surface.

3.5 REFERENCE

[1] Roberts, M., *The regenerative dialysis (REDY) sorbent system.* Nephrology, 1998. **4**(4): p. 275-278.

[2] Raja, R.M., M.S. Kramer, and J.L. Rosenbaum, *Recirculation peritoneal dialysis with sorbent Redy cartridge.* Nephron, 1976. **16**(2): p. 134-142.

[3] Agar, J.W., *Understanding sorbent dialysis systems.* Nephrology, 2010. **15**(4): p. 406-411.

[4] Urbańczyk, E., M. Sowa, and W. Simka, *Urea removal from aqueous solutions—a review.* Journal of Applied Electrochemistry, 2016. **46**(10): p. 1011-1029.

[5] Simka, W., et al., *Electrochemical treatment of aqueous solutions containing urea.* Journal of applied electrochemistry, 2009. **39**: p. 1137-1143.

[6] Hernández, M.C., et al., *Electrochemical oxidation of urea in aqueous solutions using a boron-doped thin-film diamond electrode.* Diamond and related materials, 2014. **44**: p. 109-116.

[7] Fujishima, A. and K. Honda, *Electrochemical photolysis of water at a semiconductor electrode.* nature, 1972. **238**(5358): p. 37-38.

[8] Lee, S.-Y. and S.-J. Park, *TiO2 photocatalyst for water treatment applications.* Journal of industrial and engineering chemistry, 2013. **19**(6): p. 1761-1769.

[9] Schneider, J., et al., *Understanding TiO2 photocatalysis: mechanisms and materials.* Chemical reviews, 2014. **114**(19): p. 9919-9986.

[10] Yuzawa, H., et al., *Reaction mechanism of ammonia decomposition to nitrogen and hydrogen over metal loaded titanium oxide photocatalyst.* The Journal of Physical Chemistry C, 2012. **116**(6): p. 4126-4136.

[11] Ray, N.J. and E.G. Karpov, *A Voltage Bias Effect on Catalytic Activity of Electrically Continuous Pt/TiO2 Nanocomposites.* Advanced Materials Interfaces, 2018. **5**(13): p. 1800089.

[12] Huang, F., et al., *Impacts of surface or interface chemistry of ZnSe passivation layer on the performance of CdS/CdSe quantum dot sensitized solar cells.* Nano Energy, 2017. **32**: p. 433-440.

[13] Shao, G., et al., *Dialysate Regeneration with Urea Selective Membrane Coupled to Photoelectrochemical Oxidation System.* Advanced Materials Interfaces, 2022. **9**(13): p. 2102308.

[14] Bruce J. Hinds, H.T., Guozheng Shao, *Periodic oxidation to regenerate TiO2 anodes for urea photoelectrochemical oxidation*, in *US Patent App. 63/381,896*. 2022.

[15] Shao, G., et al., *Dialysate regeneration via urea photodecomposition with TiO2 nanowires at therapeutic rates.* Artificial Organs, 2023.

[16] Simka, W., J. Piotrowski, and G. Nawrat, *Influence of anode material on electrochemical decomposition of urea.* Electrochimica acta, 2007. **52**(18): p. 5696-5703.

[17] Ji, Y., et al., *Highly selective transformation of ammonia nitrogen to N2 based on a novel solar-driven photoelectrocatalytic-chlorine radical reactions system.* Water research, 2017. **125**: p. 512-519.

[18] Yang, Y., et al., *Electrochemical oxidation of pharmaceuticals in synthetic fresh human urine: Using selective radical quenchers to reveal the dominant degradation pathways and the scavenging effects of individual urine constituents.* Water Research, 2022. **221**: p. 118722.

[19] Chen, C., et al., *Coupling N2 and CO2 in H2O to synthesize urea under ambient conditions.* Nature chemistry, 2020. **12**(8): p. 717-724.

[20] Liu, X., et al., *Mechanism of CN bonds formation in electrocatalytic urea production revealed by ab initio molecular dynamics simulation.* Nature Communications, 2022. **13**(1): p. 5471.

[21] Song, S., et al., *A selective Au-ZnO/TiO2 hybrid photocatalyst for oxidative coupling of methane to ethane with dioxygen.* Nature Catalysis, 2021. **4**(12): p. 1032-1042.

[22] Kern, R., et al., *Modeling and interpretation of electrical impedance spectra of dye solar cells operated under open-circuit conditions.* Electrochimica acta, 2002. **47**(26): p. 4213-4225.

[23] Huang, F., et al., *Hierarchical ZnO microspheres photoelectrodes assembled with Zn chalcogenide passivation layer for high efficiency quantum dot sensitized solar cells.* Journal of Power Sources, 2018. **401**: p. 255-262.

[24] Kebede, M.A., et al., *Photooxidation of Ammonia on TiO2 as a Source of NO and NO2 under Atmospheric Conditions.* Journal of the American Chemical Society, 2013. **135**(23): p. 8606-8615.

[25] Wang, H., et al., *Photoelectrocatalytic oxidation of aqueous ammonia using TiO2 nanotube arrays.* Applied Surface Science, 2014. **311**: p. 851-857.

[26] Nemoto, J., et al., *Photodecomposition of ammonia to dinitrogen and dihydrogen on platinized TiO2 nanoparticules in an aqueous solution.* Journal of Photochemistry and Photobiology A: Chemistry, 2007. **185**(2-3): p. 295-300.

[27] Vikrant, K., et al., *Photocatalytic platforms for removal of ammonia from gaseous and aqueous matrixes: status and challenges.* ACS Catalysis, 2020. **10**(15): p. 8683-8716.

[28] Mozzanega, H., J.M. Herrmann, and P. Pichat, *Ammonia oxidation over UV-irradiated titanium dioxide at room temperature.* Journal of Physical Chemistry, 1979. **83**(17): p. 2251-2255.

[29] Chang, J.-G., et al., *Adsorption configuration and dissociative reaction of NH3 on anatase (101) surface with and without hydroxyl groups.* The Journal of Physical Chemistry C, 2009. **113**(16): p. 6663-6672.

[30] Utsunomiya, A., et al., *Mechanistic study of reaction mechanism on ammonia photodecomposition over Ni/TiO2 photocatalysts.* Applied Catalysis B: Environmental, 2017. **206**: p. 378-383.

[31] Barazesh, J.M., C. Prasse, and D.L. Sedlak, *Electrochemical transformation of trace organic contaminants in the presence of halide and carbonate ions.* Environmental science & technology, 2016. **50**(18): p. 10143-10152.

[32] Maruthamuthu, P., *Absolute rate constants for the reactions of sulfate, phosphate and hydroxyl radicals with monomers.* 1980.

[33] Watts, M.J. and K.G. Linden, *Chlorine photolysis and subsequent OH radical production during UV treatment of chlorinated water.* Water research, 2007. **41**(13): p. 2871-2878.

Chapter 4. HIGHLY EFFICIENT PLASMONIC MEMBRANE FLOW REACTOR

Adapted with permission from Hao Tang, Guozheng Shao, and Bruce J. Hinds. "Highly Efficient Plasmonic Membrane Flow Reactor." *Advanced Functional Materials* 31.23 (2021): 2100342. DOI: 10.1002/adfm.202100342. Copyright 2021, Wiley.

4.1 BACKGROUND

Gold nanoparticles have shown significant plasmonic photo-catalytic activity under relatively low-intensity illumination since the collective electronic excitation, known as localized surface plasmons (LSP), could generate intense near-field electromagnetic fields and hot carriers within visible wavelength region[1-10]. Near-field electromagnetic field can be boosted up to hundred times and the energetic hot carriers generated by nonradiative decay of localized surface plasmons can be 10^6 times hotter than those from direct excitation. Photo-thermal effect is also considered to be synergistic to the localized surface plasmons[11], which contributes to photo-catalytic activity as well. The LSP-induced electromagnetic field and hot carriers have been demonstrated to facilitate photochemical transformations[12-15], such as NH_3 decomposition[4], CO oxidation[16], CO_2 reduction[17], O_2 dissociation[18, 19], H_2 dissociation[20], N_2O decomposition[21] and H_2O_2-assisted alcohol oxidations[22]. The competing technology of semiconductor photocatalysts have a number of drawbacks, mainly ascribing from the restriction of photon energies higher than the bandgap and poor catalytic activities. The most investigated n-type semiconductor photocatalyst, TiO_2 has a large bandgap (~3.2eV[23, 24]) that could only absorb photons within the low relative intensity UV region of solar spectrum, and is energy inefficient when catalytically forming bonds less than 3.2eV. Narrow bandgap semiconductors, such as α-Fe_2O_3 suffers from a slow charge carrier mobility as well as poor catalytic activities.[25]

Taking advantages of the intense near-field electromagnetic field and energetic hot electrons generated from LSP on gold nanoparticles surface, pioneering works have been reported on controllable chemical reactions. In the presence of H_2O_2, 15nm Au nanoparticles can generate intense near-field surface plasmons under 520nm LED irradiation, and thus photo-catalytically oxidize sec-phenethyl alcohol and benzyl alcohol into acetophenone and benzaldehyde, respectively.[22] However, reuse of gold nanoparticles is difficult and solution-based reactions are not able to limit secondary oxidation of product below statistical probability of reacting with the product at a given extent of reaction. In general, plasmonic field enhancements are seen at high-aspect ratio patterned edges or nanocrystals. The case of a patterned gold nanohole array on solid SiO_2 shows strong plasmonic reactions via Ag deposition at the pattern edges that is consistent with FDTD simulation. [26, 27] A novel design incorporating Au catalysis and precise array geometry to have a controllable plasmon-induced photochemical reactor is to flow reagents through a nanopore array membrane, with residence time precisely controlled by flow rate and thickness of plasmon region at pore exits. This can be achieved by depositing a thin (25nm) gold film onto porous anodized alumina oxide (AAO) membranes. Localized surface plasmon would and only be generated at the pore exits at the same thickness of around 25nm as the coated gold film. A schematic diagram of the Au@AAO structure and corresponding plasmonic oxidation process is shown in Figure 4.1. Via controlling the flow rate of solution passing through this engineered plasmonic membrane flow system, the residence time at the active region could be controlled, which limits the reaction time and thus the degree of the oxidation reaction. Moreover, with this flow membrane system, mass transport during the reaction would not be limited by diffusion but by convective flow resulting in a highly efficient photocatalytic reaction. From the study of the O_2 regeneration in H_2O_2 decomposition reaction, ~300% external quantum efficiency was observed at absorption peak, associated with hot electron generation and remaining in an excited state after H_2O_2 activation for catalytic activity. It was also found that gold oxide forms and has non-photocatalytic activity and must be accounted for in nano-scale gold catalysis. Also demonstrated was a 42% conversion of sec-phenethyl alcohol by plasmonic reactor, without any further optimization.

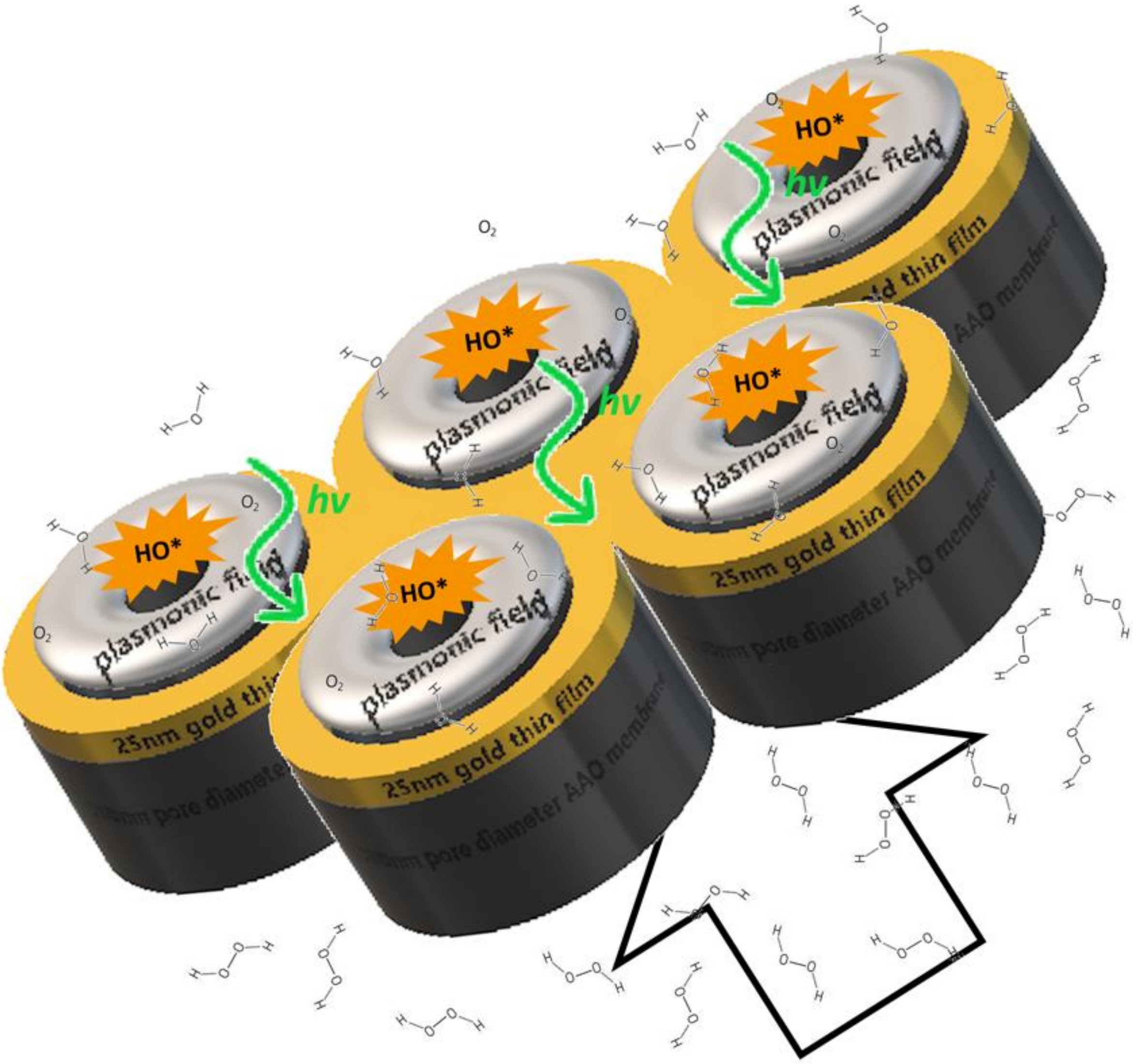

Figure 4.1. Schematic of Au@AAO membrane with generation of HO* radicals via flowing H_2O_2 solution through plasmonic membrane with plasmonic activation at pore exits with 25nm thick layer of gold.

4.2 EXPERIMENTAL METHODS

4.2.1 *Materials*

The AAO membranes with different pore diameters (20, 100, and 200nm) were purchased from Whatman plc., with specified average porosity ranging between 25 to 50%. Au for thermal vapor deposition was purchased from Ted Pella, Inc. as received. 30% H_2O_2 solution and DL-sec-phenethyl alcohol were purchased from Fisher without any further purification. Deuterium water (D_2O) with 99.9% atom % D was purchased from Sigma Aldrich as received. Single-color LEDs with different wavelengths (460, 523, 623nm) were purchased from LED Engin.

4.2.2 *Fabrication of Au@AAO Membranes*

AAOs with different pore diameters (20, 100, and 200nm) were used to fabricate Au@AAO membranes. First, AAOs were treated with O_2 plasma at 30 W for 10 min in order to remove any organic contaminations left on the surface. Then the AAOs were mounted in a thermal evaporator to vertically coat the 25 nm Au nanolayer at a rate of 0.1 nm s^{-1}. Eventually, the Au coated AAOs (Au@AAO) were mounted between two laser-cut polycarbonate frames with a hole diameter of 1.27cm, by medical grade epoxy, giving an active area of 1.27cm^2 for experiments described below.

4.2.3 *Finite-Difference Time-Domain Simulations*

A commercial software package, FDTD Solutions (Lumerical Solutions, Inc. Canada), was used to calculate transmission spectra and the near-field E-field distribution of Au@AAO membranes with the same structural parameters as those from the actual fabricated samples and the surrounding medium within the membrane pores was assumed to be H_2O.

Nanoholes with different pore diameters were used with periodic boundary conditions in two dimensions to simulate an infinite array of periodic nanoholes, which was used to stimulate the top view of the AAO membrane. Spacing of the nanoholes was carefully adjusted in order to match an average porosity to be around 50%. Deposition of the gold was simulated by directly adding a 25 nm thick Au layer on the top surface of the AAO with the same periodic nanohole structure. The auto nonuniform mesh was chosen in the entire simulation domain for higher numerical accuracy and the mesh refinement is conformal variant 2. Monitors of the frequency domain field profile were placed in the stimulated structure to calculate the E-field distribution and the transmission spectra in the continuous-wave normalization state. The magnitude of the incident E-field was taken to be unity and thus the enhancement of the electromagnetic fields could be evaluated. The optical parameters of Au, aluminum oxide, and H_2O were taken directly from the database embedded in the software.

4.2.4 *O_2 Generation from HO* by Au@AAO*

3% H_2O_2 solution was used to study the HO* formation induced by the gold plasmonic photodecomposition. To estimate the rate of HO* formation, O_2 generation rate was measured and converted into the amount of HO* formed during the plasmonic photodecomposition process. Single-color LEDs with different wavelengths (460, 523, and 623nm) were used as light sources for Au@AAO membranes with different pore diameters. The fabricated Au@AAO membrane was sandwiched by two 5mm thick silicon spacers and glass slides. The distance between the light source and the Au@AAO membrane was kept to be 1.5cm. A peristaltic pump was used to feed 3% H_2O_2 solution from the backside chamber through the Au@AAO membrane to the front chamber, with a static flow rate of 0.173mL min^{-1}. Outflow from the front chamber was connected to a gas gathering setup in order to measure the gas generation rate. Live videos were recorded in order to obtain the real-time O_2 generation rate under different experimental conditions. The O_2 generate rate was thus then converted to the amount of HO* formed during the plasmonic photodecomposition process. Applied voltage on LEDs was adjusted to provide different LED illumination intensities, and the current was then recorded in order to calculate the corresponding output power. The radiant power range for each LED was measured directly and ranged from 33 to 90mW (460nm), 21 to 75mW (523nm), 22 to 62mW (623nm) for set LED forward biases. The calculation of photon flux onto Au@AAO sample included viewing angle efficiency calculation at 1.5cm (21% efficiency) from specified Viewing Angle (100°) and Total Illumination Angle (120°) LED parameters.

4.2.5 *Alcohol Oxidation Reaction by Au@AAO*

3mM sec-phenethyl alcohol and 0.6M H_2O_2 in D2O solution were prepared for the plasmonic photocatalytic oxidation reaction with the Au@AAO flow membrane system. 200 nm pore diameter Au@AAO was used within the flow membrane system and 523 nm LED was used as the light source with applied voltage to be 2.83V. The same setup was used as the O_2 generation experiments, while the flow rate was controlled to be 0.1mL min^{-1}. The outflow from the front chamber was collected and diluted 60-fold using D_2O for 1H-NMR measurement.

4.2.6 *Characterizations*

Scanning Electrode Microscope. The scanning electron microscopy (SEM) images were taken with an FEI XL830 Dual Beam FIB/SEM with a primary electron energy of 5kV.

UV-vis Spectroscopy. The UV–vis spectra for Au@AAO samples with different pore diameters were taken by the Varian Cary 5000 UV–vis-NIR spectrophotometer.

X-ray photoelectron spectroscope. XPS spectra were taken by the Electron Spectroscopy for Chemical Analysis (ESCA) system with the Surface Sciences Instruments (SSI) M-Probe. 1H NMR spectra of sec-phenethyl alcohol and acetophenone were measured by AV-301 with the Bruker PABBI-ATMA 1H {X-BB} probe.

4.3 RESULTS AND DISCUSSION

Localized surface plasmons could generate intense near-field electromagnetic fields and hot carriers within visible wavelength region, and this local field intensity is dependent on the geometry of nanostructure as well as the surrounding environment. Finite-difference time-domain simulations[26, 27] were conducted to calculate the adsorption spectra and the distributions of the normalized E-field $|E|/|E_0|$ of the Au@AAO membranes, shown in Figure 4.2 and Figure 4.3. In the cross-sectional view of the FDTD color maps, within the red dash lines is the 25nm thick gold nanolayer, and in the top view of the FDTD color maps, the yellow arrow indicates the polarization direction of incident light. The FDTD calculated adsorption spectra for 20nm, 100nm and 200nm pore-diameter AAOs with 25nm thick gold film were in good agreement with literature simulations of similar geometries[26, 27], regarding to the absorption and transmission peaks. E-Field enhancements were calculated under four specific wavelengths (460nm, 523nm, 590nm and 623nm) of LED's that are readily available commercially. Figure 4.2a shows the absorption spectrum of 25nm Au solid SiO_2 flat surface as well as the top and cross-sectional view of the color maps for normalized E-field enhancement under 523nm incident light calculated by FDTD, revealing that without the porous structure of AAO membrane there would be no plasmonic E-field enhancement even though an absorption peak was seen around 510nm. Figure 4.2b-d show the FDTD calculated absorption spectra and color maps of the normalized E-field enhancement for 25nm thick gold film on AAOs with different pore diameters under 523nm incident light, showing that the E-field is enhanced only within the 25nm thick gold film and in a ring shape around the pore edges. Under different LED wavelengths, cross-sectional view of the FDTD calculated color maps for the normalized E-field enhancement were shown in Figure 4.3 and the factors of E-field enhancement were listed in Table 4.1 for 20nm, 100nm and 200nm pore-diameter

AAOs with 25nm thick gold film under 460nm, 523nm, 590nm and 623nm incident light. With regard to the pore-diameter dependency on plasmonic E-field enhancement, 200nm pore-diameter Au@AAO shows the highest plasmonic response compared to the 20nm and 100nm ones using the 4 available LEDS wavelengths. Moreover, via changing the wavelength of the incident light, the factor of E-field enhancement is expected to be largest around the transmission peak for each of the three Au@AAO membranes. The expectation is that a photon absorbed at the absorption peak would generate the most hot electrons while at the transmission peak plasmonic resonance will generate significant E-field enhancement around the pore edges.

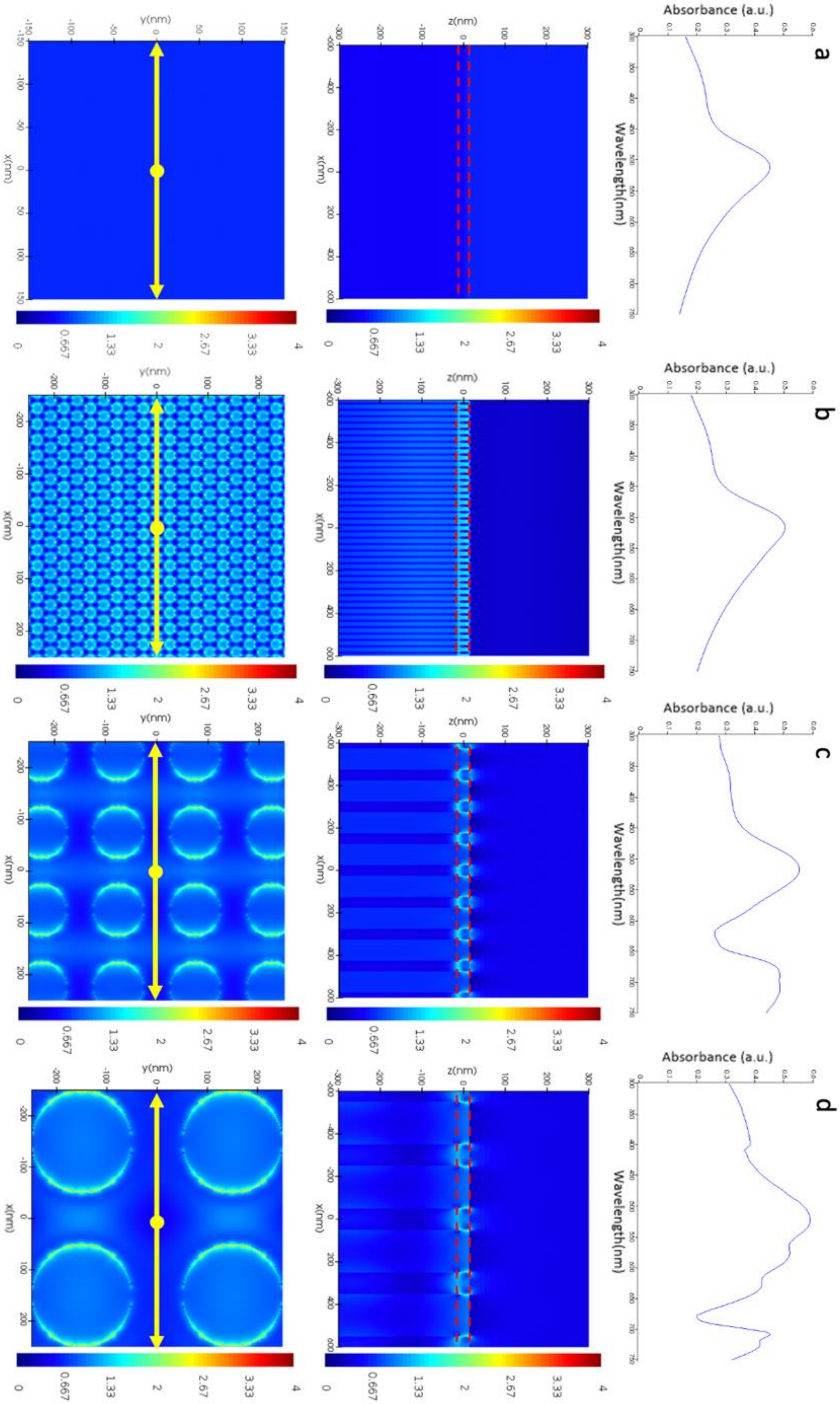
a
b
c
d
Absorbance (a.u.)
Wavelength(nm)
z(nm)
x(nm)
y(nm)
0
0.667
1.33
2
2.67
3.33
4

Figure 4.2. FDTD simulation of absorption spectra and normalized E-field $|E|/|E_0|$ enhancement under 523nm incident light for 25nm thick gold film on porous AAO: a) solid SiO_2 surface; b) 20nm; c) 100nm; d) 200nm pore diameter.

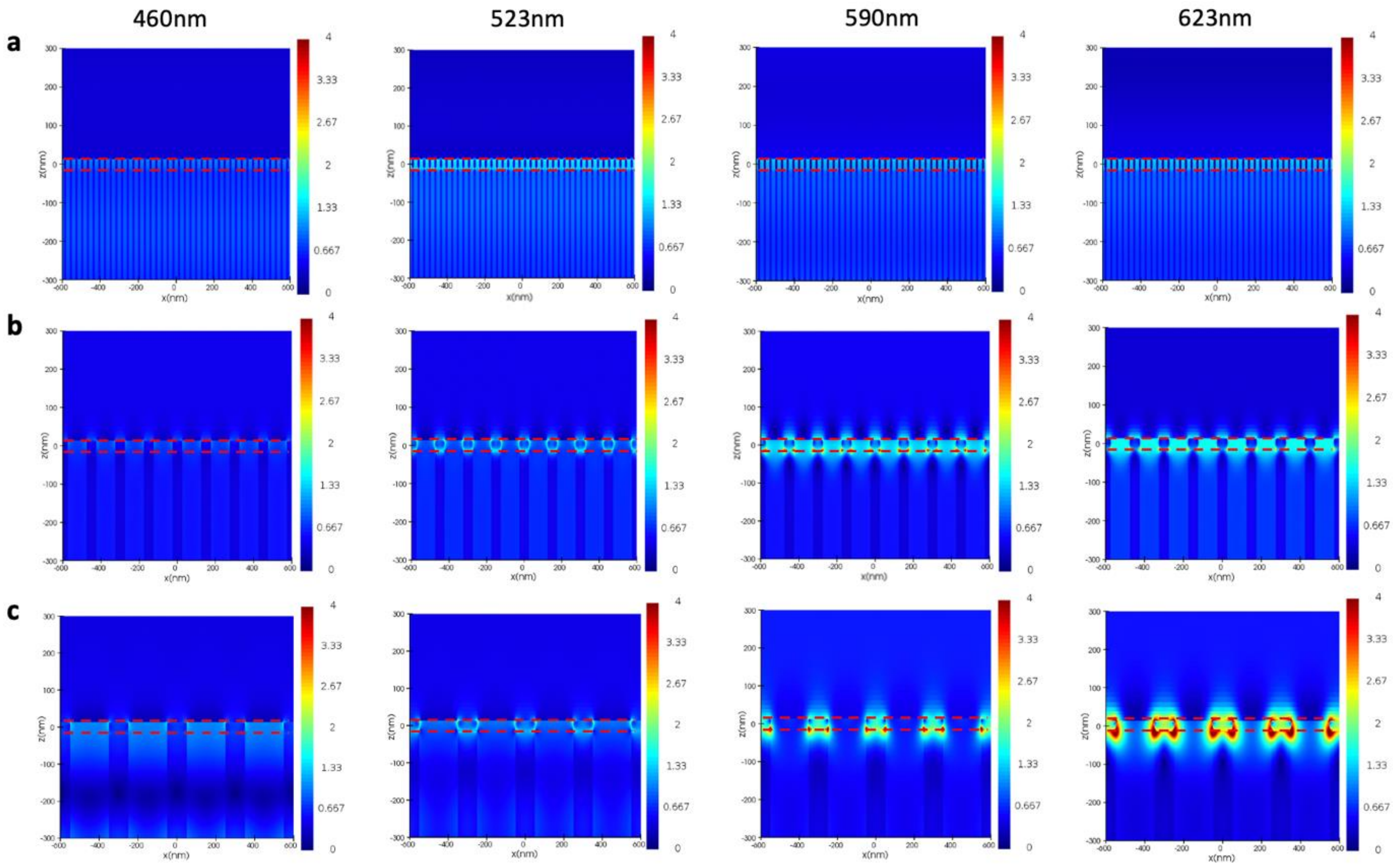
460nm
523nm
590nm
623nm
a
b
c
z(nm)
x(nm)
300
200
100
0
-100
-200
-300
-600
-400
-200
0
200
400
600
4
3.33
2.67
2
1.33
0.667
0

Figure 4.3. Cross-sectional view of the color maps for FDTD calculated normalized E-field $|E|/|E_0|$ enhancement at different wavelengths for 25nm thick gold film on porous AAO: a) 20nm; b) 100nm; c) 200nm pore diameter.

Table 4.11. Factors of the E-field enhancement under different wavelengths for 20nm; 100nm; and 200nm pore-diameter AAO membranes with 25nm thick gold film.

Wavelength Pore diameter	460nm	523nm	590nm	623nm
20nm	1.13	1.55	3.21	3.55
100nm	1.14	2.50	3.68	2.95
200nm	1.60	2.69	5.06	9.37

To investigate the plasmonic response of the Au@AAO active membrane, the cross-sectional view of the FDTD calculated color maps of the normalized E-field enhancement at absorption and transmission peaks for 100nm and 200nm pore-diameter AAOs with 25nm thick gold film were shown in Figure 4.4. The absorption and transmission peaks are at 517nm and 577nm for 100nm pore-diameter AAOs with 25nm thick gold film; 523nm and 618nm for 100nm pore-diameter Au@AAOs. The cross-sectional view of the FDTD calculated color maps of the normalized E-field enhancement for these two Au@AAO membranes show that the E-field enhancement around the pore edges is much stronger at the transmission peak rather than the absorption peak, suggesting that hot electron generation may dominate near adsorption peak. However, it is still difficult to decouple the effect of E-field enhancement and hot electron generation during the surface plasmon resonance (SPR) process at the absorption and transmission peaks.

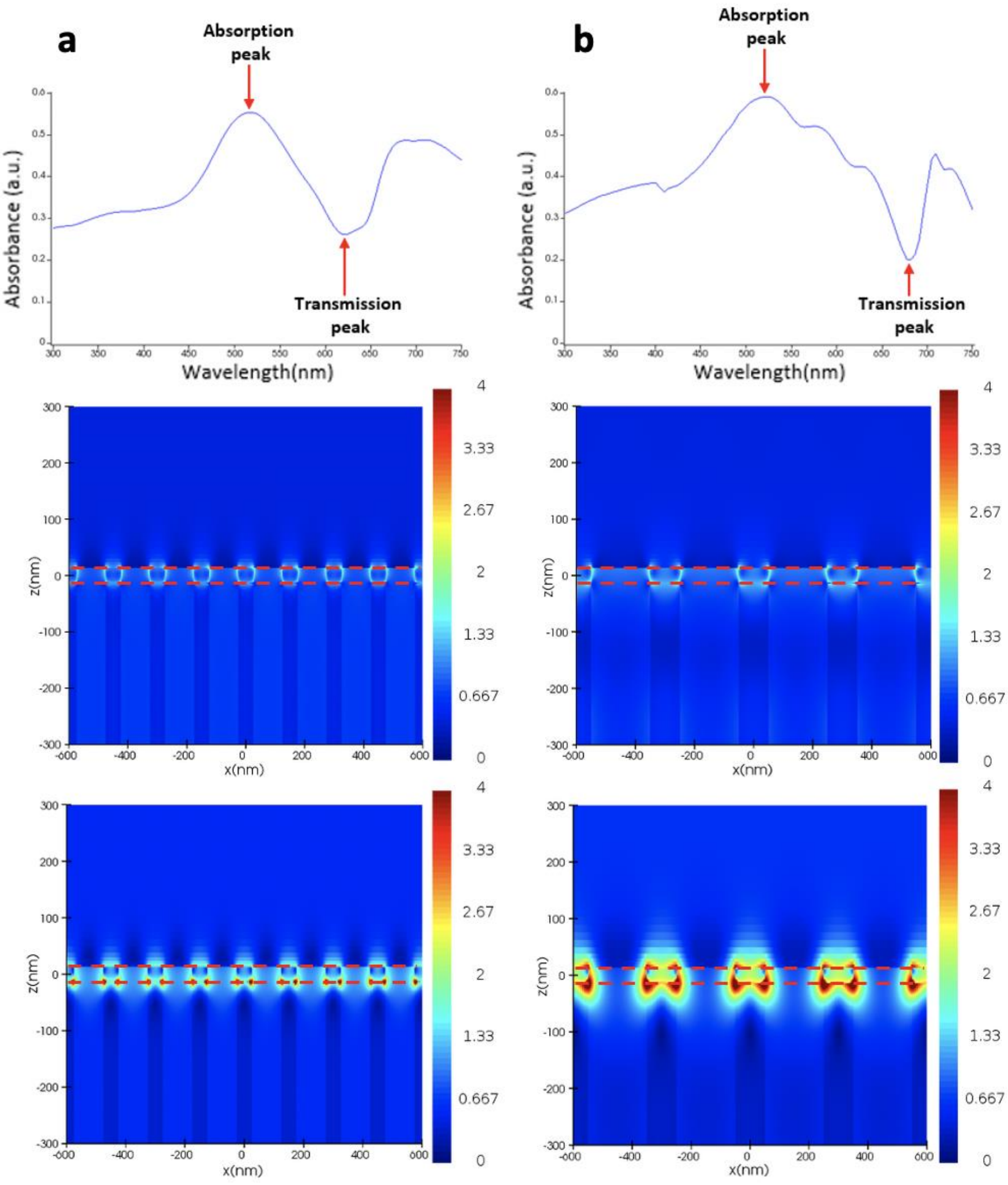

Figure 4.4. FDTD simulation of absorption spectra and electromagnetic field enhancement at absorption and transmission peak for 25nm thick gold film on porous AAO: a) 100nm; b) 200nm pore diameter.

Figure 4.5 shows the SEM images of the top and cross-sectional views of the 100nm and 200nm pore-diameter AAOs with 25nm thick gold film. The morphology of the 25nm thick gold film coating is uniform through the entire top surface of the porous AAO and does not block the pore entrances. Observing from the cross-sectional SEM images for both Au@AAO membranes, a small portion of the pores were having Au deposited further inside into the pore channels, arising from the thermal vaporization process for gold coating. The experimentally measured UV-vis absorption spectra for 100nm and 200nm pore-diameter Au@AAO are shown in Figure 4.6, which are in good agreement with the FDTD calculated spectra with peaks between 500 and 600nm.

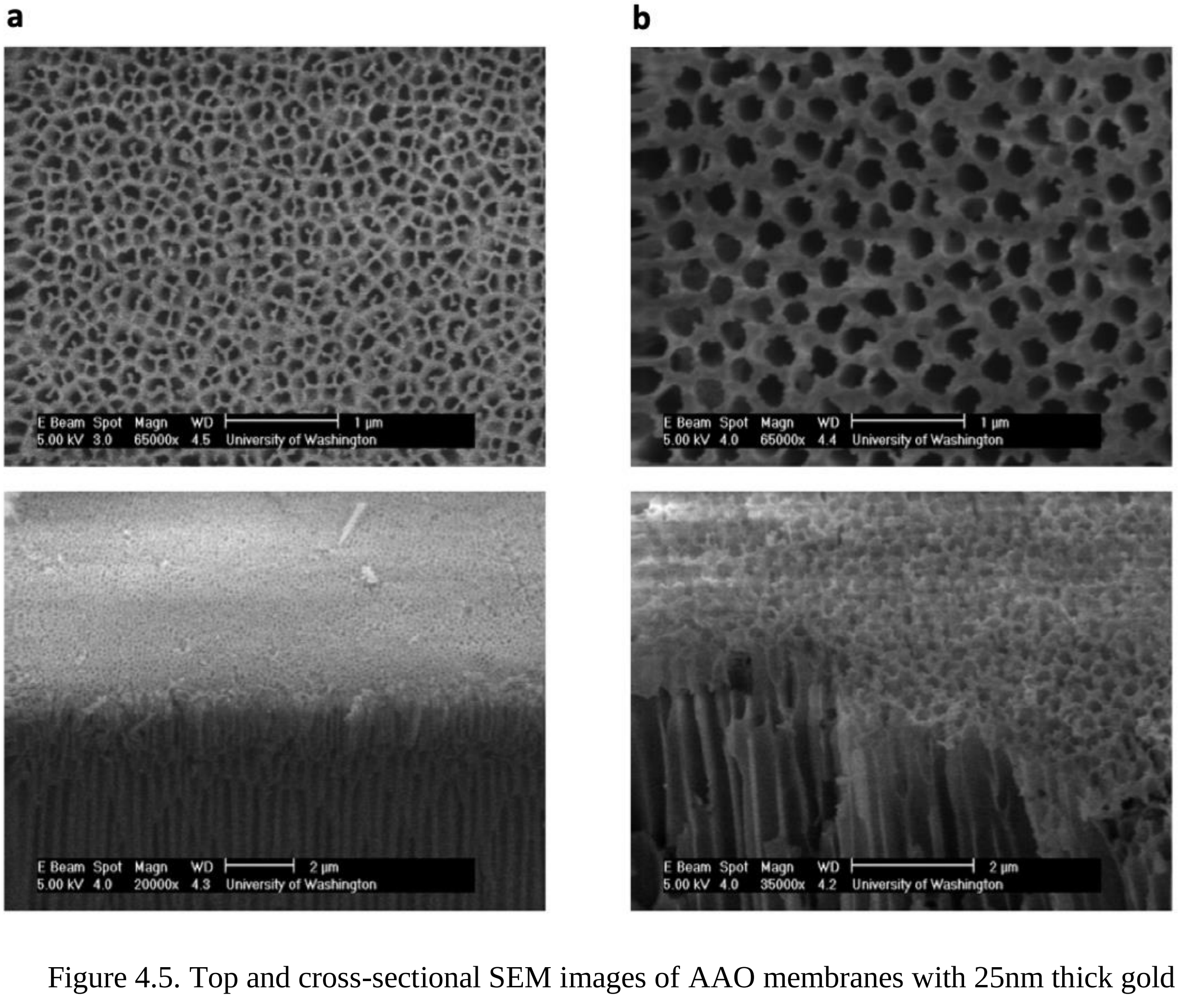

Figure 4.5. Top and cross-sectional SEM images of AAO membranes with 25nm thick gold film: a) 100nm pore-diameter Au@AAO; b) 200nm pore-diameter Au@AAO.

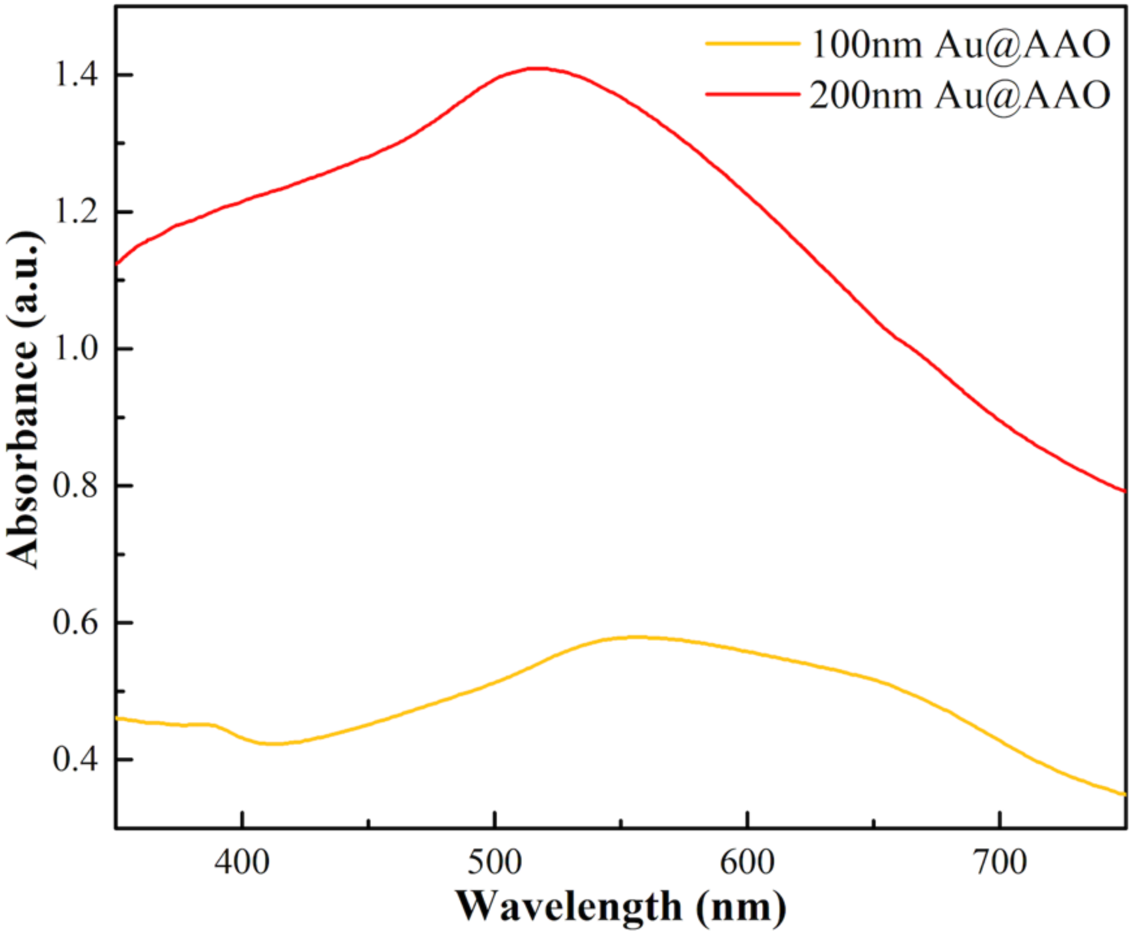

Figure 4.6. UV-vis absorption spectra and transmission spectra of 100nm and 200nm pore-diameter AAO membranes with 25nm thick gold film.

The gold plasmonic activation of peroxide was initially studied as a function of 523nm LED intensity on flat SiO_2 surface and 20nm, 100nm 200nm pore-diameter AAO membranes with 25nm thick gold film for O_2 generation experiments, as shown in Figure 4.7. It is important to note that all samples showed significant amounts of ’dark’ catalytic activity. The O_2 generation rate for the control experiment of 25nm thick gold film coated on flat SiO_2 surface did not increase with light intensity thus not showing plasmon enhanced photo-catalytic activity as expected. However increased O_2 generation rate was observed with increasing photon flux on the Au@AAO surface for 20nm, 100nm and 200nm pore-diameter Au@AAO membranes consistent with photo-catalytic activity. The 200nm pore size Au@AAO had the highest photo activity. Under dark condition where there was no light irradiation on the Au@AAO membranes, an increasing degree of O_2 generation rates were observed for 20nm, 100nm and 200nm pore-diameter Au@AAO, spontaneous H_2O_2 decomposition catalyzed by gold nanoparticles. [28-30] Thus, the calculation of photon quantum efficiency (QE) for this plasmonic membrane system must subtract the dark rate as illustrated in Figure 4.7. For each O_2 molecule generated through this gold plasmonic membrane system, 2 e^- were involved and thus the QE dependency with respect to incident photon flux for flat SiO_2 surface and 20nm, 100nm 200nm pore-diameter AAOs with 25nm thick gold film could be obtained and shown in Figure 4.8.

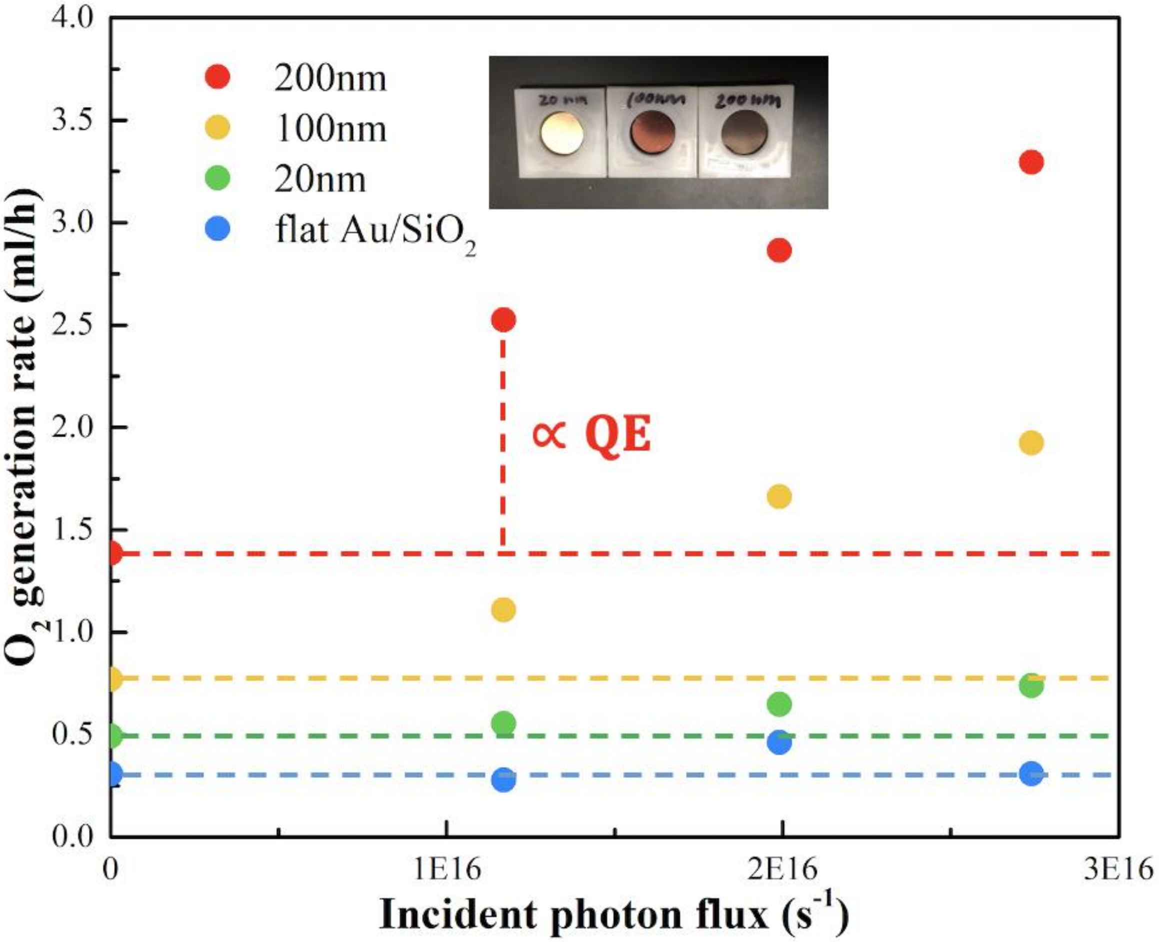

Figure 4.7. O_2 generation rate as function of incident photon flux under 523nm LED irradiation for Au@AAOs with different pore diameters.

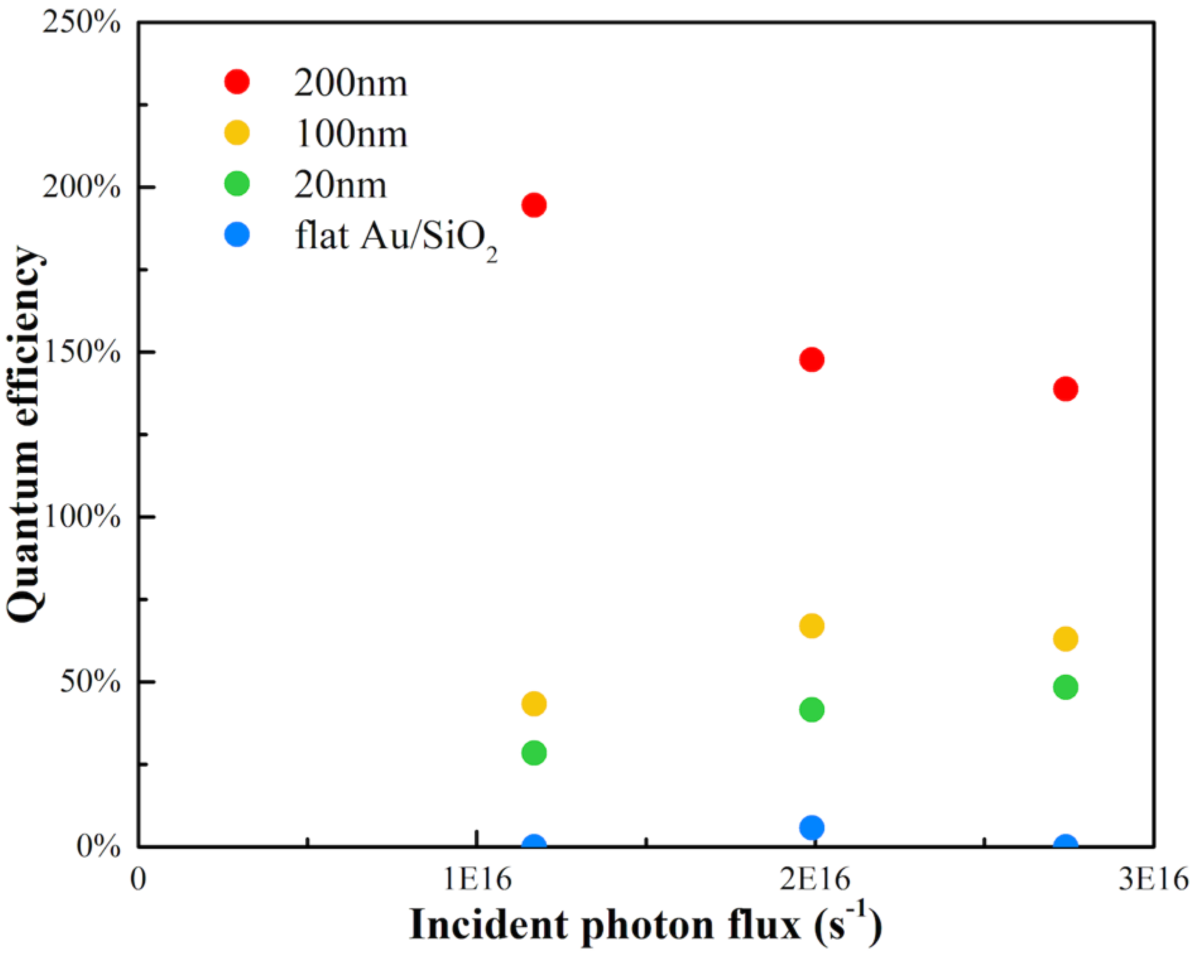

Figure 4.8. Quantum efficiency as function of AAO pore diameter and 523nm LED light intensity.

The calculated QE for 200nm pore-diameter AAO with 25nm thick gold film shows a surprisingly high value between 200-150%, which is beyond the one photon to one electron limit of quantized photoexcitation. However, for Au@AAOs with 20nm and 100nm pore diameters, the QEs were much lower and fell below the 100% limit. Nearly 0% QE was observed for the control sample of 25nm thick gold film coated on flat SiO_2 surface indicating that gold plasmonic activities could only occur with porous structures, in agreement with the FDTD simulations. For thinner 10nm thick Au films on all three AAO pore diameters, low and difficult to measure reaction rates were observed, presumably due to a non-continuous gold film from the thermal evaporation process.

The wavelength dependence on the gold plasmonic catalytic reaction for Au@AAO with 200nm pore diameter was studied with commercially available LEDs (460, 523, 623nm), with the 523nm source showing near 200% QE as shown in Figure 4.9. Among the three LEDs used, 523nm LED is closest to the optical adsorption peak of Au@AAO with 200nm pore diameter, according to both simulated and experimentally measured spectra. This indicates that gold plasmonic reaction for H_2O_2 decomposition is more favorable at the absorption peak, where hot electrons would be efficiently generated at the plasmonic region around the pore entrances. Observing over 100% QE would indicate that hot electrons remain as hot electrons after peroxide activation, hence giving catalytic activity. However, contributions of the plasmon near-field enhancement and photothermal effects cannot be quantified separately. Importantly there is very low photo-activation (QE) at the transmission peak (~620nm) where near-field enhancement would be greatest, strongly suggesting that the hot electron mechanism is dominate.

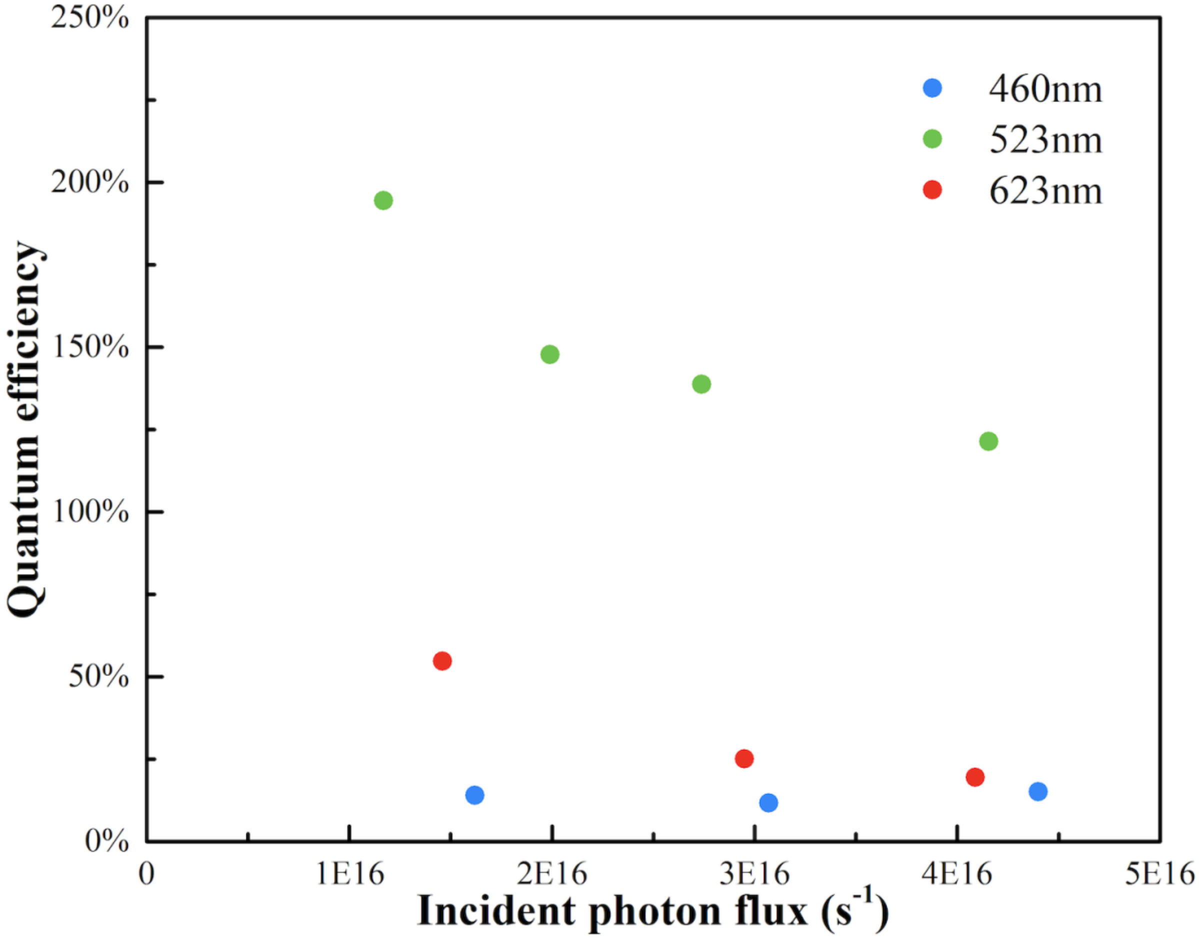

Figure 4.9. Quantum efficiency as function of incident photon flux for Au@AAO with 200nm pore diameter, under different wavelengths LED irradiation.

The plasmonic photocatalytic reaction rate is reported to exhibit a linear dependence on the light intensity at low intensity, and a super-linear power law dependence on the light intensity under a significantly high intensity irradiation. [19] Our observation was that QE decreased with increasing incident photon flux. Interestingly, a significant color change was observed on the Au@AAOs with 200nm pore diameter after H_2O_2 experiments, as shown in the inset of Figure 9. UV-vis spectra of the fresh-prepared and used 200nm pore-diameter Au@AAO samples were measured experimentally and shown in Figure 4.10, which further confirmed that there was an absorption peak shift from 517nm to 490nm after operation in H_2O_2 experiments for a cumulative 12 hours. The change in absorbance does not account for the large drop in QE. This suggests that the surface activity of (Au^0) has changed.

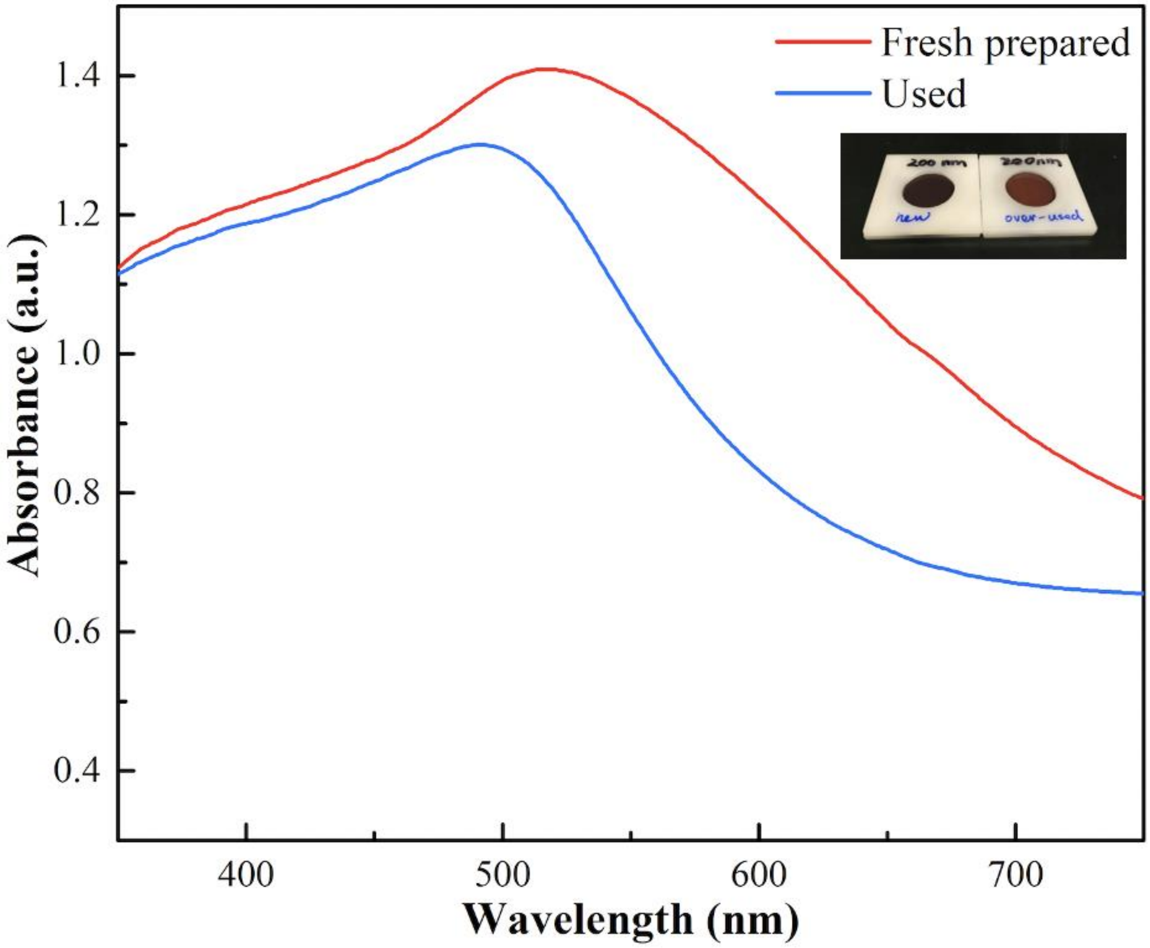

Figure 4.10. Experimentally measured UV-vis absorption spectra of 200nm pore-diameter AAO with 25nm thick gold film when fresh-prepared and used for 12hrs.

Surface state analysis of the gold thin film on AAO was conducted with XPS measurements, and the spectra for the fresh-prepared and used samples are shown in Figure 4.11. For fresh-prepared samples, a small amount of Au^{3+} does exist due to oxidation during the thermal vaporization process for preparing the Au@AAO samples. The fresh-prepared Au@AAO sample did have an Au^{3+}/Au^0 ratio of 0.23, however after running H_2O_2 experiments for 12 hours the Au^{3+}/Au^0 ratio dramatically increased to 0.59 presumably forming surface Au_2O_3 on the gold thin film.

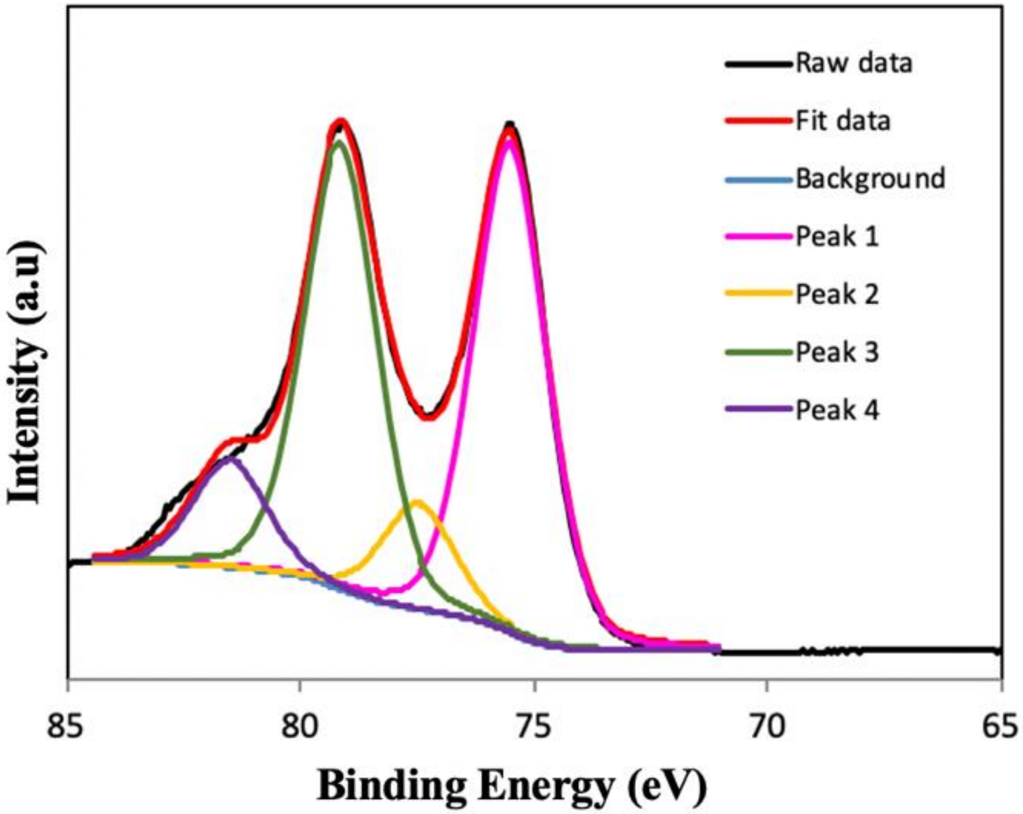
Raw data
Fit data
Background
Peak 1
Peak 2
Peak 3
Peak 4
Intensity (a.u)
85
80
75
70
65
Binding Energy (eV)

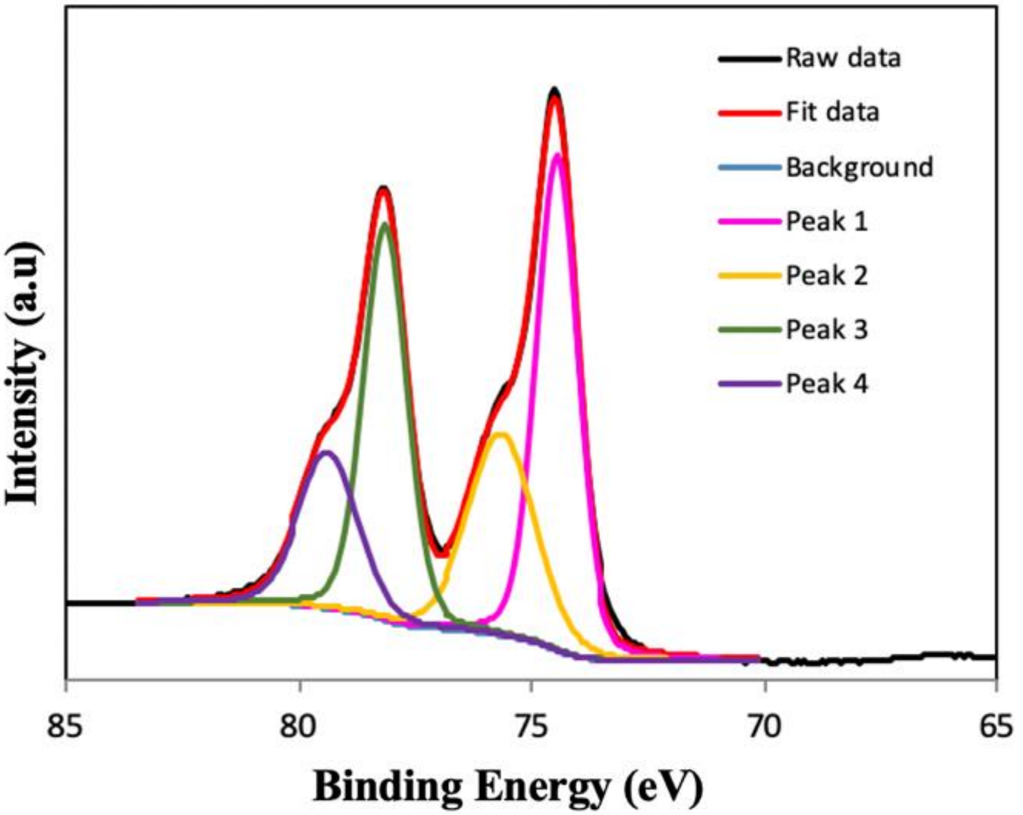
Raw data
Fit data
Background
Peak 1
Peak 2
Peak 3
Peak 4
Intensity (a.u)
85
80
75
70
65
Binding Energy (eV)

Figure 4.11. X-ray photoelectron spectra of Au 4f peaks from fresh-prepared and used 200nm pore-diameter AAOs with 25nm thick gold film.

Table 4.12.. The chemical composition of Au thin film on fresh-prepared and used 200nm pore-diameter AAOs, and the ratio of Au^{3+}/Au^0 before and after H_2O_2 experiments for 12 hours.

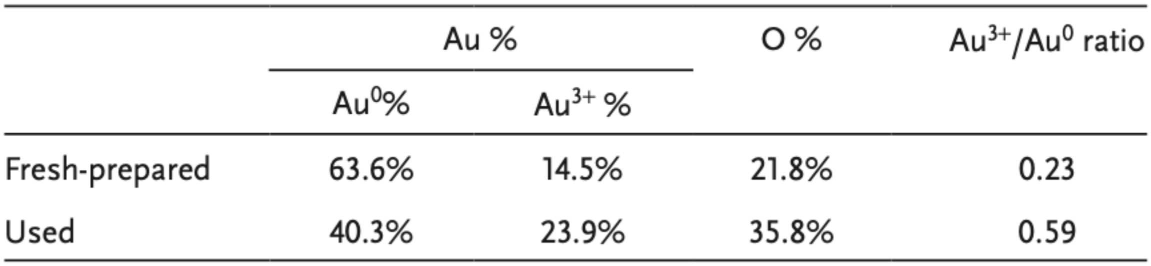

	Au %		O %	Au^{3+}/Au^0 ratio
	Au^0%	Au^{3+} %		
Fresh-prepared	63.6%	14.5%	21.8%	0.23
Used	40.3%	23.9%	35.8%	0.59

In order to prove the hypothesis, O_2 generation rates over time under dark condition and under 523nm light irradiation were video recorded for 12hrs with two samples prepared in the same batch, shown in Figure 4.12. The QE of O_2 generation over reaction time for 200nm pore-diameter Au@AAO was calculated by subtracting the ‘dark’ reaction rate at each time point, shown in Figure 4.13. Under dark conditions, the O_2 generation rate kept increasing during the first 6 hours and then stayed stable at around 5ml/h, which suggests that the gold oxide thin film could is catalytically active for the decomposition reaction of H_2O_2. This catalytic activity of gold thin film increased over time, and we mainly ascribed to the formation of more Au_2O_3 during the H_2O_2 flow reaction. The QE of O_2 generation over reaction time for 200nm pore-diameter Au@AAO exhibited an increasing trend at the first 3 hours from 130% to 250%, and then kept around 250% for another 3 hours. However, due to the oxidation of plasmonic active Au^0 within the gold thin film, the QE started to drop after 6hr operation under the H_2O_2 flow reaction and reached a low level around 120%. This long-term dynamic study of the gold-plasmon photodecomposition of H_2O_2 provides strong evidence that Au_2O_3 is catalytically active and must be accounted for in plasmonic catalysis studies. However, it is important to note that remarkably high QE was continuously observed for about 6hrs in this Au@AAO membrane system and efforts to extend stability are ongoing. By taking the advantages of the flow membrane system, with well-controlled residence time of the solution flowing through the catalytic active region, a single oxidation event can still be achieved even if the peroxide activation reaction is dominated by the Au_2O_3 catalyzed reaction.

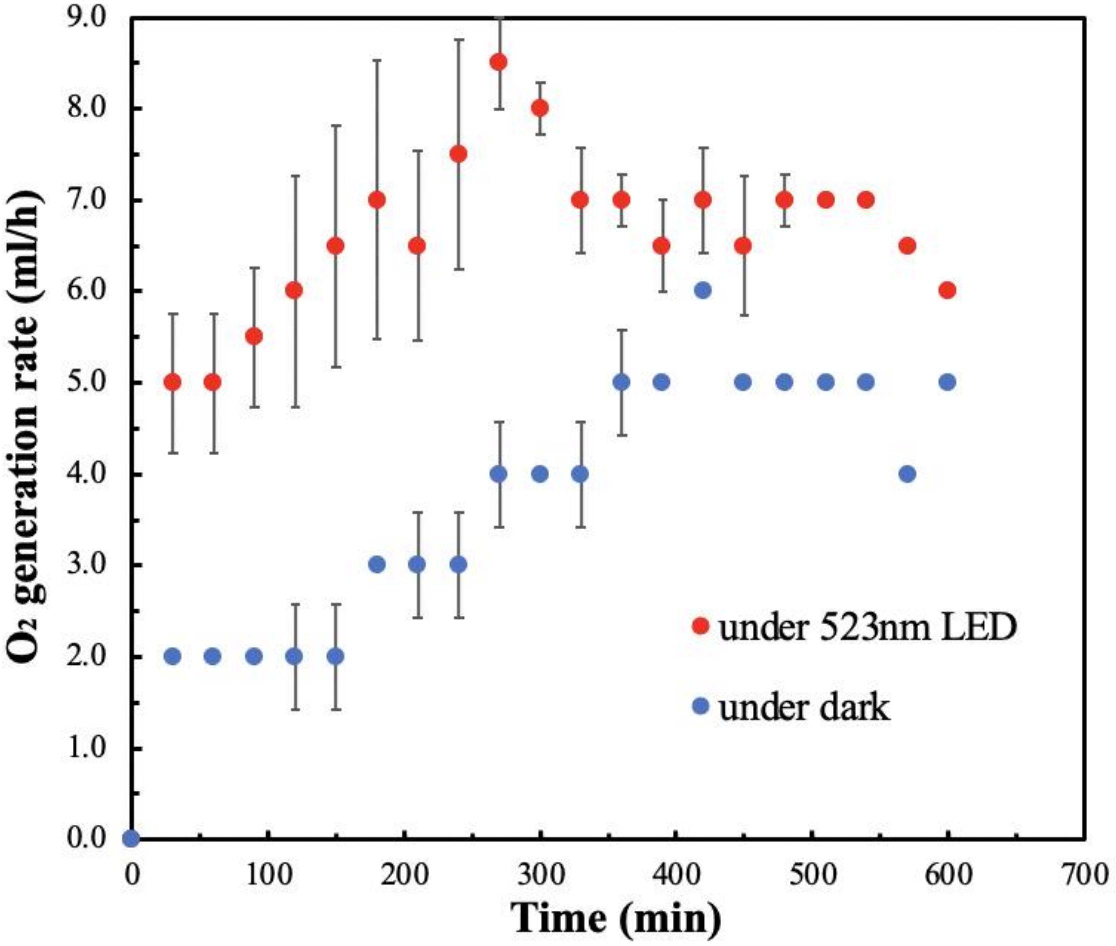

Figure 4.12. O_2 generation rate over time under dark condition and under 523nm light irradiation, video recorded for 12hrs.

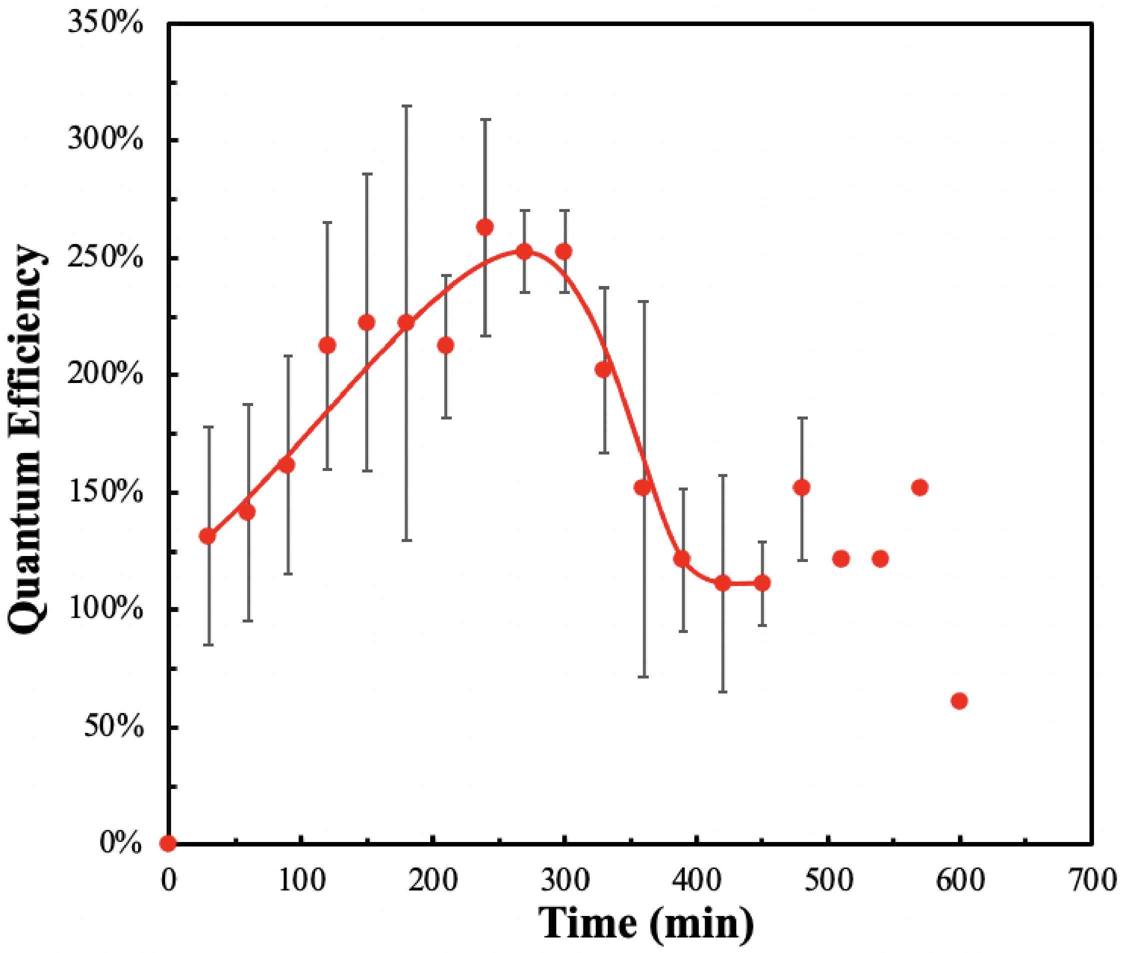

Figure 4.13. Quantum efficiency of O_2 generation over reaction time for Au@AAO with 200nm pore diameter.

To demonstrate the utility of the plasmonic flow reactor as a method to both activate the oxidation reaction and limit it to a single oxidation event by controlling residence time, a model phenolic compound was studied. An aqueous 3mM sec-phenethyl alcohol flowed through this 200nm pore-diameter Au plasmonic flow membrane system, in the presence of 0.6M H_2O_2, with Au surface under 523nm LED illumination with output power of 0.153W. The solution flow rate of 0.1 ml/min, corresponds to an approximate residence time of 2ms in the 25nm thick plasmonic region and matches molar photon flux to substrate molar flux. 42% of the alcohol was selectively converted into acetophenone as measured by NMR in the permeate while remainder was unreacted reagent. The remainder of peroxide radical formed O_2, reducing overall alcohol oxidation efficiency. These initial tests show that an idealized photochemical flow system can be realized with a gold plasmonic flow membrane system.

4.4 CONCLUSION

The plasmonic flow reactor concept has been demonstrated with over 200% QE for peroxide activation and the ability to limit the reaction to a single oxidation reaction by controlling residence time with flow rate and pore geometry. Periodic pore arrays of 25 nm thick Au were modeled by FDTD simulations predicting the largest e-field enhancements for larger 200 nm pore diameters. Shifts in both optical adsorption and transmission peaks as a function of pore diameter were simulated and experimentally confirmed. Peroxide activation, as measured by O_2 generation was most efficient with 200 nm pore diameter system under 523 nm LED illumination. The optimal wavelength falls near the absorption peak of Au@AAO with 200 nm pore diameter, which is consistent for both FDTD calculation and experimental measured UV–vis spectrum. This suggests that hot electron generated from the gold plasmonic response is the primary mechanism for the activation of H_2O_2. However, the E-field enhancement and photothermal effects from LSP resonance could not be completely excluded by these initial experiments, though E-field enhancement is modeled to be a factor of only 2.7 and thus unlikely a significant factor. The QE for the gold plasmonic flow system calculated from the O_2 generation experiments was as high as 250%, which indicates a mechanism of a hot-electron activation of peroxide that leaves a still energetic hot electron to catalytically activate multiple reactions. A confounding factor in this system is the formation of Au surface oxides that are catalytically active in dark conditions and must be accounted for in Au plasmonic photochemical studies. By flowing sec-phenethyl alcohol and peroxide through an optimized Au@AAO system with 523 nm LED illumination, the controlled single oxidation product of acetophenone was observed demonstrating the promise of plasmonic flow membrane reactors.

4.5 REFERENCE

[1] Liu, J.G., et al., *Relaxation of Plasmon-Induced Hot Carriers.* Acs Photonics, 2018. **5**(7): p. 2584-2595.

[2] Zhou, L., et al., *Quantifying hot carrier and thermal contributions in plasmonic photocatalysis.* Science, 2018. **362**(6410): p. 69-+.

[3] Zhang, X., et al., *Transient localized surface plasmon induced by femtosecond interband excitation in gold nanoparticles.* Scientific Reports, 2018. **8**.

[4] Zheng, B.Y., et al., *Distinguishing between plasmon-induced and photoexcited carriers in a device geometry.* Nature Communications, 2015. **6**.

[5] Christopher, P. and M. Moskovits, *Hot Charge Carrier Transmission from Plasmonic Nanostructures.* Annual Review of Physical Chemistry, Vol 68, 2017. **68**: p. 379-398.

[6] Linic, S., et al., *Photochemical transformations on plasmonic metal nanoparticles.* Nature Materials, 2015. **14**(6): p. 567-576.

[7] Linic, S., P. Christopher, and D.B. Ingram, *Plasmonic-metal nanostructures for efficient conversion of solar to chemical energy.* Nature Materials, 2011. **10**(12): p. 911-921.

[8] Mubeen, S., et al., *An autonomous photosynthetic device in which all charge carriers derive from surface plasmons.* Nature Nanotechnology, 2013. **8**(4): p. 247-251.

[9] Ding, S.-Y., et al., *Electromagnetic theories of surface-enhanced Raman spectroscopy.* Chemical Society Reviews, 2017. **46**(13): p. 4042-4076.

[10] Tian, Z.Q., B. Ren, and D.Y. Wu, *Surface-enhanced Raman scattering: From noble to transition metals and from rough surfaces to ordered nanostructures.* Journal of Physical Chemistry B, 2002. **106**(37): p. 9463-9483.

[11] Cao, L., et al., *Plasmon-assisted local temperature control to pattern individual semiconductor nanowires and carbon nanotubes.* Nano Letters, 2007. **7**(11): p. 3523-3527.

[12] Aslam, U., et al., *Catalytic conversion of solar to chemical energy on plasmonic metal nanostructures.* Nature Catalysis, 2018. **1**(9): p. 656-665.

[13] Zhan, C., et al., *From plasmon-enhanced molecular spectroscopy to plasmon-mediated chemical reactions.* Nature Reviews Chemistry, 2018. **2**(9): p. 216-230.

[14] Choi, C.H., et al., *Plasmon-Mediated Electrocatalysis for Sustainable Energy: From Electrochemical Conversion of Different Feedstocks to Fuel Cell Reactions.* Acs Energy Letters, 2018. **3**(6): p. 1415-1433.

[15] Baffou, G. and R. Quidant, *Nanoplasmonics for chemistry.* Chemical Society Reviews, 2014. **43**(11): p. 3898-3907.

[16] Aslam, U., S. Chavez, and S. Linic, *Controlling energy flow in multimetallic nanostructures for plasmonic catalysis.* Nature Nanotechnology, 2017. **12**(10): p. 1000-1005.

[17] Robatjazi, H., et al., *Plasmon-induced selective carbon dioxide conversion on earth-abundant aluminum-cuprous oxide antenna-reactor nanoparticles.* Nature Communications, 2017. **8**.

[18] Seemala, B., et al., *Plasmon-Mediated Catalytic O-2 Dissociation on Ag Nanostructures: Hot Electrons or Near Fields?* Acs Energy Letters, 2019. **4**(8): p. 1803-1809.

[19] Christopher, P., et al., *Singular characteristics and unique chemical bond activation mechanisms of photocatalytic reactions on plasmonic nanostructures.* Nature Materials, 2012. **11**(12): p. 1044-1050.

[20] Mukherjee, S., et al., *Hot Electrons Do the Impossible: Plasmon-Induced Dissociation of H-2 on Au.* Nano Letters, 2013. **13**(1): p. 240-247.

[21] Swearer, D.F., et al., *Plasmonic Photocatalysis of Nitrous Oxide into N-2 and O-2 Using Aluminum-Iridium Antenna-Reactor Nanoparticles.* Acs Nano, 2019. **13**(7): p. 8076-8086.

[22] Hallett-Tapley, G.L., et al., *Plasmon-Mediated Catalytic Oxidation of sec-Phenethyl and Benzyl Alcohols.* Journal of Physical Chemistry C, 2011. **115**(21): p. 10784-10790.

[23] Dette, C., et al., *TiO2 Anatase with a Bandgap in the Visible Region.* Nano Letters, 2014. **14**(11): p. 6533-6538.

[24] Bian, L., et al., *Band gap calculation and photo catalytic activity of rare earths doped rutile TiO2.* Journal of Rare Earths, 2009. **27**(3): p. 461-468.

[25] Mishra, M. and D.-M. Chun, *alpha-Fe2O3 as a photocatalytic material: A review.* Applied Catalysis a-General, 2015. **498**: p. 126-141.

[26] Ai, B., et al., *Plasmonic Nanochemistry Based on Nanohole Array.* Acs Nano, 2017. **11**(12): p. 12094-12102.

[27] Schwind, M., B. Kasemo, and I. Zoric, *Localized and Propagating Plasmons in Metal Films with Nanoholes.* Nano Letters, 2013. **13**(4): p. 1743-1750.

[28] Ghosh-Mazumdar, A.S. and E.J. Hart, *Advances in Chemistry Series No. 81*. Radiation Chemistry I. 1968, Washington, DC: American Chemical Society, Ed. R. F. Gould. 193.

[29] He, W., et al., *Intrinsic catalytic activity of Au nanoparticles with respect to hydrogen peroxide decomposition and superoxide scavenging.* Biomaterials, 2013. **34**(3): p. 765-773.

[30] Ballarin, B., et al., *Supported Gold Nanoparticles for Alcohols Oxidation in Continuous Flow Heterogeneous Systems.* Acs Sustainable Chemistry & Engineering, 2017. **5**(6): p. 4746-4756.

Chapter 5. CONCLUSIONS AND FUTURE DIRECTIONS

5.1 CONCLUSIONS

In conclusion, two distinct types of photocatalytic materials have been studied in the field of wearable dialysis devices and quantized chemical oxidation reactions for precise pharmaceutical synthesis. The first photocatalytic material studied is TiO2, and a novel urea photodecomposition system (POUR) was developed for the efficient and selective photodecomposition of urea into N_2 and CO_2, enabling dialysate regeneration for portable kidney dialysis. The early study focused on the long-term stability of the TiO_2 photocatalyst, as it is crucial for continuous and efficient urea removal. Through XPS surface chemistry analysis, the formation of Ti-C bonds concurrent with photocatalytic activity decrease was observed. To maintain the urea photodecomposition performance, TiO_2 regeneration treatments utilizing an oxidative environment were explored, including periodic air purging and high voltage bias pulses during the device operation. With optimized parameters, the equivalent urea removal rate reached the target level for a wearable dialysis device over a 52-hour test. Also, it has been proven that an external voltage could facilitate charge carrier separation within single crystalline nanowires and reduce the recombination process, and thus the photocurrent could be increased by ~100-fold comparing to that measured with no bias applied. After that, a more systematic and deeper study was conducted to focus on the role of chlorine ions (Cl^-) and chlorine radicals ($Cl\cdot$) as key intermediates in the photo-oxidation reaction of urea on the TiO_2 surface. The investigations of flow-rate and urea-concentration dependencies revealed that the urea photo-oxidation reaction is not mass transport limited but surface reaction limited, and the applied voltage was again proven to improve the urea photodecomposition rate by facilitating charge carrier separation and minimizing recombination.

The presence of chlorine ions (Cl^-) has been identified as essential for promoting efficient photodecomposition, and the chlorine radicals ($Cl\cdot$) were shown to be vital intermediate species involved in the photo-oxidation reaction on the TiO_2 surface.

In another material system, gold nanoparticles exhibit promising photocatalytic activities via the localized surface plasmonic resonance (LSPR) phenomenon, which could be used in precise pharmaceutical synthesis. A plasmonic flow reactor utilizing thin Au film at the exits of monolithic anodized aluminum oxide (AAO) membranes was demonstrated. The system exhibited over 200% quantum efficiency for peroxide activation, with the ability to control single oxidation reactions through residence time manipulation using flow rate and pore geometry. The optimization of pore diameter and LED illumination wavelength resulted in the most efficient peroxide activation, suggesting that hot electron generation from gold plasmonic response is the primary mechanism for H_2O_2 activation. The calculated high quantum efficiency (250%) for the gold plasmonic flow system indicates a hot-electron activation of peroxide, leaving an energetic hot electron to catalytically activate multiple reactions. By flowing sec-phenethyl alcohol and peroxide through the optimized Au@AAO system, controlled single oxidation product of acetophenone was observed, demonstrating the potential of the plasmonic flow membrane reactor design for quantized chemical oxidation reactions in pharmaceutical applications.

Overall, the entire PhD project encompasses two parts focusing on photocatalytic materials for distinct applications. Firstly, we investigated the utilization of TiO_2 in a novel urea photodecomposition system (POUR) for dialysate regeneration in portable kidney dialysis, with a specific emphasis on long-term stability and regeneration treatments. After that, we systematically examine the role of chlorine ions (Cl^-) and chlorine radicals ($Cl\cdot$) as key intermediates in the photo-oxidation reaction of urea on the TiO_2 surface to gain insights into the photocatalytic mechanism.

Secondly, we explored the promising photocatalytic activities of gold nanoparticles through localized surface plasmonic resonance (LSPR) in a plasmonic flow reactor, demonstrating efficient peroxide activation and single oxidation reactions, particularly applicable in precise pharmaceutical synthesis.

5.2 FUTURE DIRECTIONS

For the future work on the TiO_2 mechanism study for urea photo-oxidation reaction, a more detailed and complicated computational modeling will be conducted with DFT simulations for the urea photo-oxidation at the TiO_2 surface via $Cl^-/Cl\cdot$ as the key intermediate in reaction pathways. No research group has been reported to study the mechanism for urea photo-oxidation with TiO_2, but for the synthesis of urea from N_2 and CO_2. Figure 5.1 shows the free energy diagram of urea production from a theoretical DFT calculation and Figure 5.2 illustrates the proposed reaction mechanism of urea production, which can be considered as the reversed reaction for the urea photo-oxidation in the TiO_2 system. With DFT simulations done on the urea photo-oxidation process, we will be able to further confirm our proposed reaction pathway shown in Figure 3.8, as well as the role of chlorine ions (Cl^-) and chlorine radicals ($Cl\cdot$) as the key intermediates in urea photo-oxidation reaction.

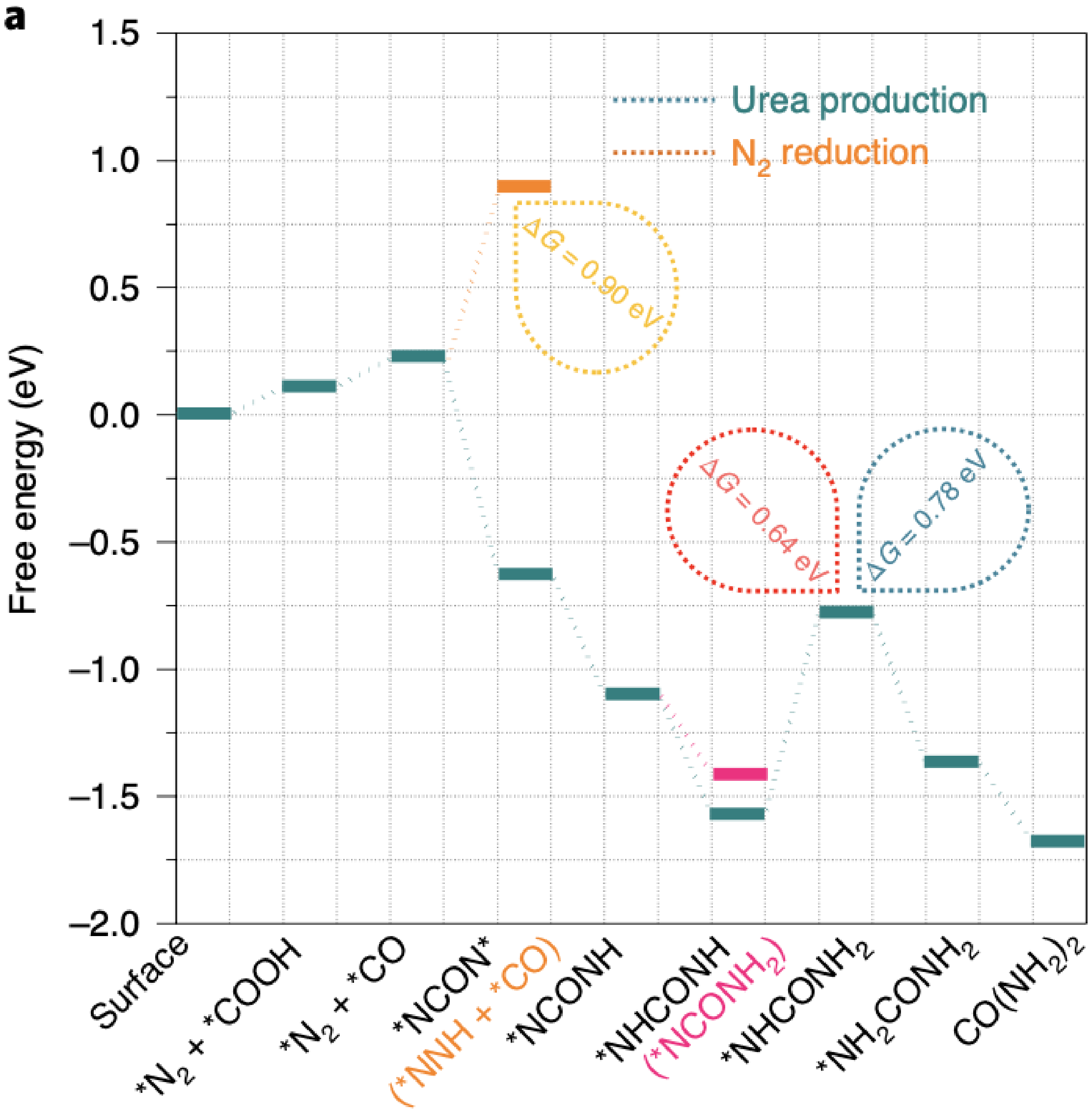

Figure 5.1. Theoretical calculated free energy diagram of urea production with DFT simulations; reproduced with permission from ref [1]. Copyright 2020, Springer Nature.

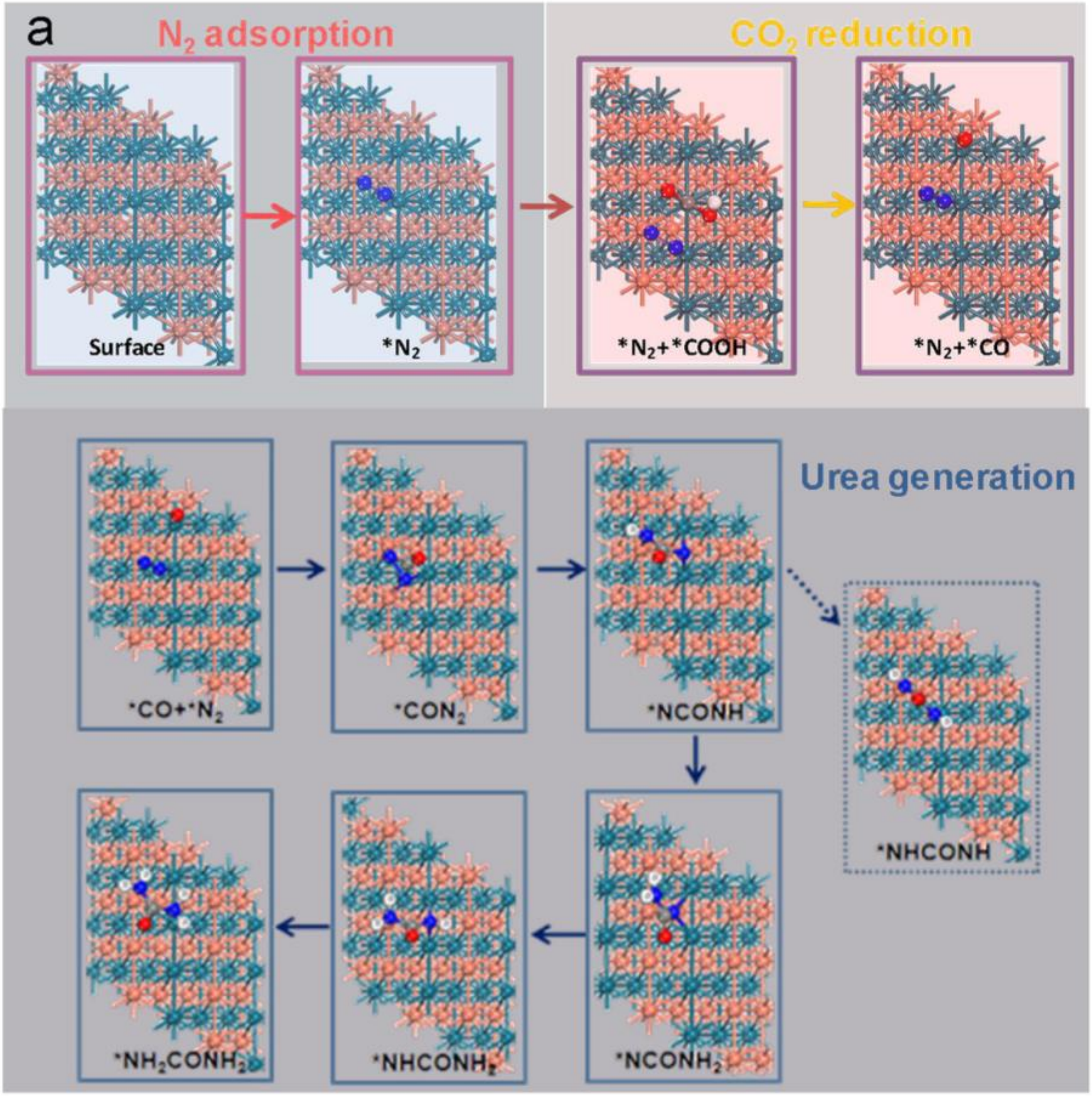

Figure 5.2. A possible reaction mechanism of urea production; reproduced with permission from ref [1]. Copyright 2020, Springer Nature.

5.3 REFERENCE

[1] Chen, Chen, et al. "Coupling N2 and CO2 in H2O to synthesize urea under ambient conditions." Nature chemistry 12.8 (2020): 717-724.

VITA

Education Background:

Molecular Engineering: Data Science, Ph.D.	University of Washington	2017/09 – 2023/08
Molecular Engineering, Master	University of Washington	2017/09 – 2020/06
Materials Science & Engineering, Master	University of Washington	2015/09 – 2016/12
Materials Science & Engineering: Biomaterials, Bachelor	Georgia Institute of Technology	2013/08 – 2015/05
Materials Science & Engineering	University of Idaho	2011/01 – 2013/05
Energy and Power Engineering	Central South University	2009/09 – 2010/07

Publications:

- **Hao Tang**, Guozheng Shao, and Bruce J. Hinds. " Regeneration of TiO_2 Photocatalytic Activity for Urea Oxidation to Enable Continuous Portable Kidney Dialysis." Submitted.
- Shao, Guozheng, **Hao Tang**, Shen Ren, Sharon A. Creason, Syed Faisal, Anna Galperin, Alberto Aliseda, Dayong Gao, Buddy Ratner, and Bruce J. Hinds. "Dialysate Regeneration via Urea Photodecomposition with TiO_2 Nanowires at Therapeutic Rates." Artificial Organs (2023).
- Bruce Hinds III, **Hao Tang**, Guozheng Shao. "Periodic oxidation to regenerate TiO_2 anodes for urea photoelectrochemical oxidation" US Patent App. 63/381,896.
- Shao, Guozheng, **Hao Tang**, Shen Ren, Sharon A. Creason, Dayong Gao, Buddy D. Ratner, and Bruce J. Hinds. "Dialysate Regeneration with Urea Selective Membrane Coupled to Photoelectrochemical Oxidation System." Advanced Materials Interfaces 9.13 (2022): 2102308.
- **Hao Tang**, Guozheng Shao, and Bruce J. Hinds. "Highly Efficient Plasmonic Membrane Flow Reactor." Advanced Functional Materials (2021): 2100342.
- Ren, Shuxia, Weichao Dong, **Hao Tang**, Lingzhi Tang, Zhenhua Li, Qiang Sun, Huifang Yang, Zhigang Yang, and Jinjin Zhao. "High-efficiency magnetic modulation in Ti/ZnO/Pt resistive random-access memory devices using amorphous zinc oxide film." Applied Surface Science 488 (2019): 92-97.
- **Hao Tang**, Huang, Fei, Yuan Wang, Juan Hou, Zhaoyu Liu, Robert C. Massé, Jianjun Tian, and Guozhong Cao. "Hierarchical ZnO microspheres photoelectrodes assembled with Zn chalcogenide passivation layer for high efficiency quantum dot sensitized solar cells." Journal of Power Sources 401 (2018): 255-262.

- Zhao, Jinjin, Zhenghao Liu, **Hao Tang**, Chunmei Jia, Xingyu Zhao, Feng Xue, Liyu Wei, Guoli Kong, Chen Wang, and Liu Jinxi. "Enhanced performance of solar cells via anchoring $CuGaS_2$ quantum dots." Science China Materials 60, no. 9 (2017): 829-838.
- Huang, Fei, Juan Hou, Hongen Wang, **Hao Tang**, Zhaoyu Liu, Lisha Zhang, Qifeng Zhang, Shanglong Peng, Jianshe Liu, and Guozhong Cao. "Impacts of surface or interface chemistry of ZnSe passivation layer on the performance of CdS/CdSe quantum dot sensitized solar cells." Nano Energy 32 (2017): 433-440.